Title
1D, 2D, and 3D Periodic Structures: Electromagnetic Characterization, Design, and Measurement

Author
Brockett, Timothy John

Publication Date
2013

Peer reviewed|Thesis/dissertation

University of California

Los Angeles

1D, 2D, and 3D Periodic Structures:

Electromagnetic Characterization, Design, and Measurement

A dissertation submitted in partial satisfaction

of the requirements for the degree

Doctor of Philosophy in Electrical Engineering

by

Timothy John Brockett

2013

Abstract of the Dissertation

1D, 2D, and 3D Periodic Structures: Electromagnetic Characterization, Design, and Measurement

by

Timothy John Brockett

Doctor of Philosophy in Electrical Engineering

University of California, Los Angeles, 2013

Professor Yahya Rahmat-Samii, Chair

Periodic structures have many useful applications in electromagnetics including phased arrays, frequency selective surfaces, and absorbing interfaces. Their unique properties can be used to provide increased performance in antenna gain, electromagnetic propagation, and electromagnetic absorption. In antenna arrays, repeating elements create a larger effective aperture, increasing the gain of the antenna and the ability to scan the direction of the main beam. Three-dimensional periodic structures, such as an array of shaped pillars such as columns, cones, or prisms have the potential of improving electromagnetic absorption, improving performance in applications such as solar cell efficiency and absorbing interfaces. Furthermore, research into periodic structures is a continuing endeavor where novel approaches and analysis in appropriate applications can be sought.

This presentation will address the analysis, diagnostics, and enhancement of 1D, 2D, and 3D periodic structures for antenna array applications and solar cell technology. In particular, a unique approach to array design will be introduced to prevent the appearance of undesirable grating lobes in large antenna arrays that employ subarrays. This approach, named the distortion diagnostic procedure,

can apply directly to 1D and 2D periodic structures in the form of planar antenna arrays. Interesting corollaries included here are developments in millimeter-wave antenna measurements including spiral planar scanning, phaseless measurements, and addressing antennas that feature an internal source. Finally, analysis and enhancement of 3D periodic structures in nanostructure photovoltaic arrays and absorbing interfaces will be examined for their behavior and basic operation in regards to improved absorption of electromagnetic waves.

The dissertation of Timothy John Brockett is approved.

Christoph Niemann

Diana Huffaker

Tatsuo Itoh

Yahya Rahmat-Samii, Committee Chair

University of California, Los Angeles

2013

To all that fostered my interest in engineering . . .

Table of Contents

List of Figures

Acknowledgments

I would like to primarily acknowledge my advisor Professor Yahya Rahmat-Samii for providing guidance and support over the duration of my graduate career. I would like to thank Dr. Harish Rajagopalan, Dr. Farhad Razavi, Dr. Shengheng Xu, and Dr. Keyvan Bahadori, Dr. Ilkyu Kim, Jordan Budhu, Shebendu Bradawaj, and Joshua Kovitz for their collaboration, discussions, and friendship. I would also like to thank Minji Zhu, manager of the Center for High Frequency Electronics, for his cooperation and support in maintaining UCLA's antenna chambers. Finally, I would like to thank Giacomo Mariani, Dr. Ramesh B. Laghumavarapu, and Professor Diana Huffaker for their assistance in my nanostructure research.

Vita

1982	Born, Oakland, California, USA.
2003-2007	Laboratory Manager, Center for High Frequency Electronics, Electrical Engineering Department, University of California, Los Angeles.
2004	B.S. (Electrical Engineering), University of California, Los Angeles.
2008	M.S. (Electrical Engineering), University of California, Los Angeles.
2008-Present	Graduate Student Researcher and Teaching Assistant, Electrical Engineering Department, UCLA.

Publications

Journal Papers

T. J. Brockett, H. Rajagopalan, R. B. Laghumavarapu, D. Huffaker, Y. Rahmat-Samii, "Electromagnetic Characterization of High Absorption Sub-Wavelength Optical Nanostructure Photovoltaics for Solar Energy Harvesting," IEEE Transactions on Antennas and Propagation, vol.61, no.4, pp.1518-1527, April 2013.

T. J. Brockett, Y. Rahmat-Samii, "Subarray Design Diagnostics for the Suppression of Undesirable Grating Lobes,"IEEE Transactions on Antennas and Prop-

agation, vol. 60, no.3, March 2012.

S. F. Razavi, S. Xu, T. Brockett, and Y. Rahmat-Samii, "The spillover effect on the directivity calculation of reflector antennas in planar near-field measurements," IEEE Antennas and Propagation Magazine, vol. 51, no. 6, pp. 124-134, Dec. 2009.

T. J. Brockett and Y. Rahmat-Samii, "A Novel Portable Bipolar Near-field Measurement System for Millimeter-wave Antennas: Construction, Development, and Verification," IEEE Antennas Propagat. Mag., vol. 50, no. 5, pp. 121-130, Oct. 2008 (cover page article).

Conference Papers

T. J. Brockett, Y. Rahmat-Samii, "Measuring the Radiation Pattern of Integrated Antennas with Internal Sources: A Phaseless Near-field Technique," 2013 IEEE Antennas and Propagation Society International Symposium (APSURSI), Orlando, Fl, July 2013.

T. J. Brockett, H. Rajagopalan, Y. Rahmat-Samii, "On understanding the enhancement of optical absorption in nanostructure photovoltaic solar cells," 2012 IEEE Antennas and Propagation Society International Symposium (APSURSI), Chicago, IL, 8-14 July 2012.

H. Rajagopalan, T. J. Brockett, Y. Rahmat-Samii, "Superquadric nanostructures for enhanced absorption in solar cells," 2012 IEEE Antennas and Propagation Society International Symposium (APSURSI), Chicago, IL, 8-14 July 2012.

T. J. Brockett, H. Rajagopalan, Y. Rahmat-Samii, "A New Paradigm in Solar Energy Harvesting: Characterization of High Absorption Nanopilar Array Photovoltaics" presented at the 2012 USNC-URSI Radio Science Meeting, Boulder, CO, January 2012.

T. J. Brockett and Y. Rahmat-Samii, "Sub-array Design Diagnostics for the Development of Large Uniform Arrays," 2011 IEEE Antennas and Propagation Society International Symposium (APSURSI), Spokane, Washington, 3-8 July 2011.

H. Rajagopalan, T. Brockett, and Y. Rahmat-Samii, "Investigation of Semiconductor Nanostructured Photovoltaic for Next Generation Solar Cells," 2011 IEEE Antennas and Propagation Society International Symposium (APSURSI), Spokane, Washington, 3-8 July 2011

T. J. Brockett, Y. Rahmat-Samii, "Diagnosis of Undesirable Grating Lobes in Large Array Antennas Comprised of Sub-array Elements," presented at the URSI Conference 2011, Boulder, Colorado, 2011.

T. J. Brockett, H. Rajagopalan, Y. Rahmat-Samii, "Semiconductor Nanopillar Characterization for Improved Solar Energy Collection using Full-wave Electromagnetic Analysis," presented at the URSI Conference 2011, Boulder, Colorado, 2011.

T. J. Brockett, Y. Rahmat-Samii, "On the importance of sub-array design in the suppression of undesirable grating lobes," 2010 IEEE International Symposium on Phased Array Systems and Technology (ARRAY), pp.745-750, Waltham, Massachusetts, 12-15 Oct. 2010.

T. J. Brockett, H. Rajagopalan, Y. Rahmat-Samii, "GaAs nano-pillars for solar power absorption: Electromagnetic characterization," 2010 IEEE Antennas and Propagation Society International Symposium (APSURSI), pp.1-4, Toronto, Ontario, 11-17 July 2010.

T. J. Brockett, Y. Rahmat-Samii, "Spiral scanning for bipolar planar near-field antenna measurements: A comparative study," 2010 IEEE Antennas and Propagation Society International Symposium (APSURSI),pp.1-4, Toronto, Ontario, 11-17 July 2010.

T. J. Brockett and Y. Rahmat-Samii, "Advantages of Rapid Bipolar Planar Near-field Scanner for Millimetre-wave Antenna Measurement," EuCAP 2010, Barcelona, Spain.

T. J. Brockett, Y. Rahmat-Samii, "Continuous Bipolar Spiral Scanning for Bipolar Planar Near-field Antenna Measurements," presented at the URSI Conference 2010, Boulder, Colorado, 2010.

T. J. Brockett, Y. Rahmat-Samii, "Rapid Continuous Linear Spiral Measurements for Millimeter-waves," Antenna Measurements & Techniques Association Conference, Salt Lake City, UT, 2009.

T. J. Brockett and Y. Rahmat-Samii, "Millimeter-Wave Bi-polar Planar Phaseless Measurements and Diagnostics: Characterization of a Ka-Band Patch Array," accepted to 2009 IEEE International Symposium on Antennas and Propagation, Charleston, SC.

T. J. Brockett and Y. Rahmat-Samii, "A Portable Bi-Polar Millimetre-Wave

Antenna Near-Field Measurement System," AMTA EuCAP 2008, Berlin, Germany.

T. J. Brockett and Y. Rahmat-Samii, "UCLA's Portable Millimeter-Wave Bipolar Planar Near-field Antenna Measurement System," 2008 IEEE International Symposium on Antennas and Propagation, San Diego, CA, Jul. 2008, pp. 1-4.

T. J. Brockett and Y. Rahmat-Samii, "UCLA's Millimeter-Wave Bi-polar Planar Antenna Measurement System: A Novel Portable Design," AMTA Symposium 2007, St. Louis, MO.

CHAPTER 1

Introduction

Periodic structures have many useful applications in electromagnetics including phased arrays, electromagnetic bandgap (EBG) structures, frequency selective surfaces (FSS), and reflectarrays [1–3]. They exhibit unique properties that can be used to provide increased performance in antenna gain, electromagnetic propagation, and electromagnetic absorption. In antenna arrays, repeating elements create a larger effective aperture, increasing directivity of the antenna and, if an appropriate phase distribution is applied, scan the direction of the main beam. Beyond the planar elemental structures, a periodic array of three-dimensional (3D) shaped pillars such as columns, cones, or prisms have the potential of improving electromagnetic absorption, enhancing performance in applications such as solar cell efficiency and microwave absorber [4]. Furthermore, research into periodic structures is a continuing endeavor where novel approaches and analysis to appropriate applications can be sought.

This dissertation will address the analysis, diagnostics, and enhancement of 1D, 2D, and 3D periodic structures for antenna array applications and solar cell technology. The 1D structures that will be covered here will include linear antenna arrays. In particular, a unique approach to array design will be introduced to prevent the appearance of undesirable grating lobes in large antenna arrays that use subarrays. This approach differs from most approaches by focusing on the subarray design, as the subarray can be a source of distortion that can cause the appearance of grating lobes. This technique, named the distor-

tion diagnostic procedure, will apply directly to 2D periodic structures in the form of millimeter-wave planar arrays. The design, diagnostics, fabrication, and measurement of these millimeter-wave planar arrays will be address. Interesting corollaries included here are developments in millimeter-wave antenna measurements including spiral planar scanning, phaseless measurements, and addressing antennas that feature an internal source. Finally, analysis and enhancement of periodic structures with three-dimensional elements in nanostructure photovoltaic arrays and microwave absorber will be examined for their behavior and basic operation in regards to improved absorption of electromagnetic waves. Throughout this dissertation, 3D refers to the three-dimensional nature of the elements, not three-dimensional periodicity. Two-dimensional periodicity is used for these 3D elements. Future research in these areas include development of analytical models to facilitate periodic structure design and optimization.

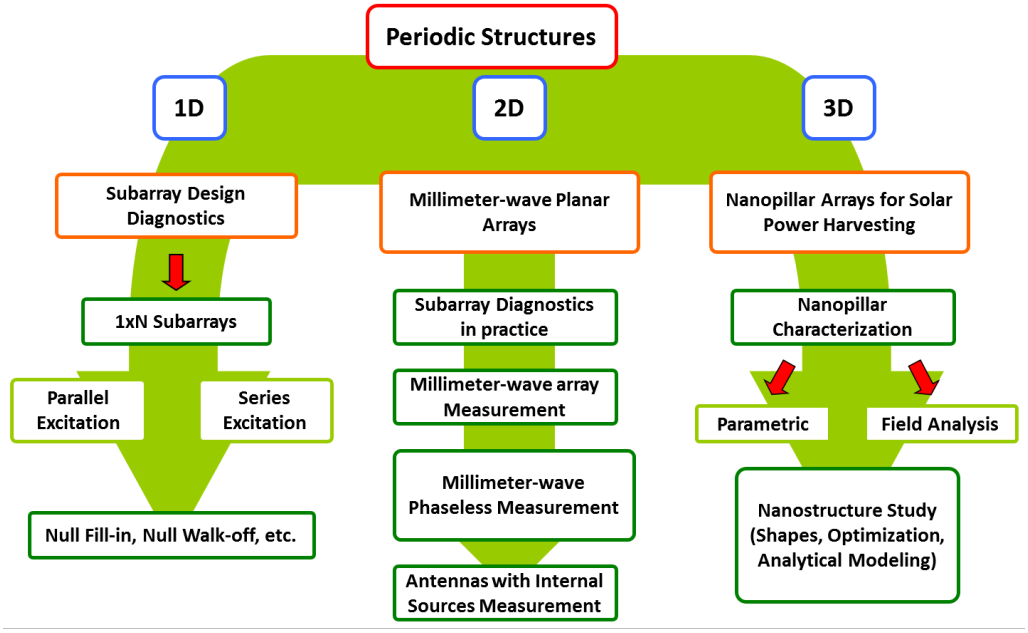

Figure 1.1: Dissertation Outline

Fig. 1.1 presents a diagram of the dissertation outline. After a brief introduction to the relevant background in periodic structure theory and analysis, the

dissertation will be divided into three main parts: Namely, 1D, 2D, and 3D structures. Each section will be bridged as each of the topics discussed here have been motivated by previous research. Overall, the dissertation is aimed demonstrating the application and utility of periodic element theory and analysis to a diverse body of electromagnetic structures and components. The chapters are divided as follows: Chapter 2 will cover fundamental periodic structure theory including antenna array theory, the infinite array model, and floquet modes. Chapter 3 will introduce subarray design diagnostics for linear arrays, a novel technique to approach to design large antennas arrays. Chapter 4 will describe the application of the design diagnostics to 2D planar millimeter-wave antenna arrays. Chapter 5 will introduced developments in millimeter-wave antenna array measurements. Chapter 6 will detail periodic structures in solar power harvesting applications. This includes both characterization and analysis of nanostructure photovoltaic arrays.

CHAPTER 2

Periodic Structures in Electromagnetics

Electromagnetic theory of periodic structures forms the basis for the investigations introduced here. For antenna arrays, basic antenna array theory is used to devise novel approaches to antenna array design using subarrays and provide diagnostic tools to analyze subarray designs. Further theory, related to near-field antenna and phaseless measurements, are used in Chapter 5 for verification of antenna array performance. For the analysis of nanostructure periodic arrays for solar energy applications, the infinite array model and floquet modes are used in the full-wave analysis tool to calculate performance and provide field illustrations that can aid understanding of these structures. This chapter will review the basic theory that was utilized in the investigations introduced here.

2.1 Antenna Array Theory

The performance of an antenna array is a function of its geometrical configuration, the distance between adjacent elements, the excitation amplitude, the excitation phase, and the pattern of its individual elements [5]. The final antenna array pattern of an antenna array with N elements is the superposition of the fields of each element:

$$\vec{E_t} = \vec{E_1} + \vec{E_2} + \ldots + \vec{E_N} \tag{2.1}$$

If one assumes that all elements are identical, it allows the equation to be

written:

$$\tilde{E}_t = \tilde{E}_{element}(1 + e^{j(kd\cos\theta+\beta)} + e^{j2(kd\cos\theta+\beta)} + \ldots + e^{j(N-1)(kd\cos\theta+\beta)}) \tag{2.2}$$

where d is the distance between adjacent elements, β is the excitation phase, and k is the wave number. The term $(1+e^{j(kd\cos\theta+\beta)}+e^{j2(kd\cos\theta+\beta)}+\ldots+e^{j(N-1)(kd\cos\theta+\beta)})$ is usually is separately called the 'array factor' (AF) and can be used to determine the overall array pattern. For a NxM array, the array factor can be reduced to:

$$AF(\theta,\phi) = \{\frac{1}{M}\frac{\sin(\frac{M}{2}\psi_x)}{\sin(\frac{\psi_x}{2})}\}\{\frac{1}{N}\frac{\sin(\frac{N}{2}\psi_y)}{\sin(\frac{\psi_y}{2})}\} \tag{2.3}$$

where $\psi_x = d_x\sin(\theta)\cos(\phi)+\beta_x$ and $\psi_y = d_y\sin(\theta)\cos(\phi)+\beta_y$. Thus, for an array comprised of identical antenna elements, the overall radiation pattern is simply the product of the elemental pattern and the array factor [5].

A useful property of antenna arrays is that the main beam of the radiation pattern can be controlled by manipulating the excitation phase of the individual elements. Scanning the beam requires a progressive phase shift along adjacent elements. The angle of scanned beam involves the excitation phase β in each direction:

$$\beta_x = -kd_x\sin(\theta_0)\cos(\phi_0) \tag{2.4}$$

$$\beta_y = -kd_y\sin(\theta_0)\sin(\phi_0) \tag{2.5}$$

where θ_0 and ϕ_0 is the desired scan angle.

Complication in antenna array design and beam scanning occurs when practical limitations (cost or physical limitations) prevent individual control of the array elements. For example, when elements are arranged in subarrays, a myriad of issues such as grating or quantization lobes can arise [6]. Quantization lobes occurs

when quantized (stepped) phase is applied to the inputs of individual subarrays. Many techniques have been introduced to compensate for this issue including subarray amplitude tapers, irregular spacing of elements, and other techniques [7–11]. Other issues that may arise include design errors in the subarray cause the appearance of grating lobes [12]. Addressing this issue is the subject of Chapter 3 and 4.

2.2 Near-field Measurements and Phase Retrieval

The development of the indoor bi-polar planar measurement technique occurred in the early 1990s at University of California, Los Angeles by Professor Yahya Rahmat-Samii, Dr. Lawrence Williams, and Robert Yaccarino. The technique was a modification on the previous plane-polar measurement technique [13], which itself was a modification on the traditional plane-rectangular measurement technique. The main feature of the bi-polar technique that separates it from plane-polar or plane-rectangular is its elimination of linear motion over the plane of measurement. Instead, it uses two rotations, one to rotate the antenna under test (AUT), and the other to position the measuring probe in sweeping arcs over the AUT. These two rotations is where the "bi" prefix comes from. A brief overview of the specifics of the bi-polar scanning technique will follow. A more detailed explanation of the bi-polar planar technique can be found in [14].

2.2.1 The Bipolar Scanner

The bi-polar planar scan was devised as a modification on the plane-polar technique to eliminate linear motion in the measurement. As a result, mechanical implementation of the scanner became simpler and less costly while preserving the inherent advantages of plane-polar scanners over the traditional plane-rectangular scanner [15].

Fig. 2.1 shows a standard implementation of the bipolar planar scanner [15]. The AUT, on the right of the figure, sits upon a rotary stage mount and is able to rotate 360 degrees. On the left, a second rotary stage mounts an arm upon a pillar structure that reaches over the AUT. The two sides are connected by a common base, designed to fix the distance between the ARM and the AUT axes. On one end of the arm, a rotation axis and translation axis allows the measuring probe to position itself in relation to the AUT. The probe rotation axis allows the probe to set the polarization and also allows co-rotation between the AUT and probe, preserving the polarization throughout the measurement. The probe translation axis, the only linear motion in the measurement, allows the measuring probe to change the distance between the AUT and probe. This is especially important for phase-less measurements, which entails taking amplitude data from two separate planes above the AUT. The other end of the arm holds counterweights. These help stabilize the arm system and transfers the weight of the arm to the center of the ARM rotary stage.

The movement of the AUT and ARM axes results in a planar grid shown in Fig. 2.2 [15]. The location of the ARM and AUT axes on the measurement plane are described by its own unique bi-polar coordinate system denoted by two independent coordinates α and β. α describes the rotation position of the AUT axis while β describes the rotation position of the ARM axis. These coordinates can be related to the traditional polar coordinates and Cartesian coordinates by the following equations:

Polar Coordinates:

$$\rho = 2L\sin(\frac{\beta}{2}) \tag{2.6}$$

$$\phi = \alpha - \frac{\beta}{2} \tag{2.7}$$

Cartesian Coordinates:

$$x = L * \sin(\beta - \alpha) + \sin(\alpha) \tag{2.8}$$

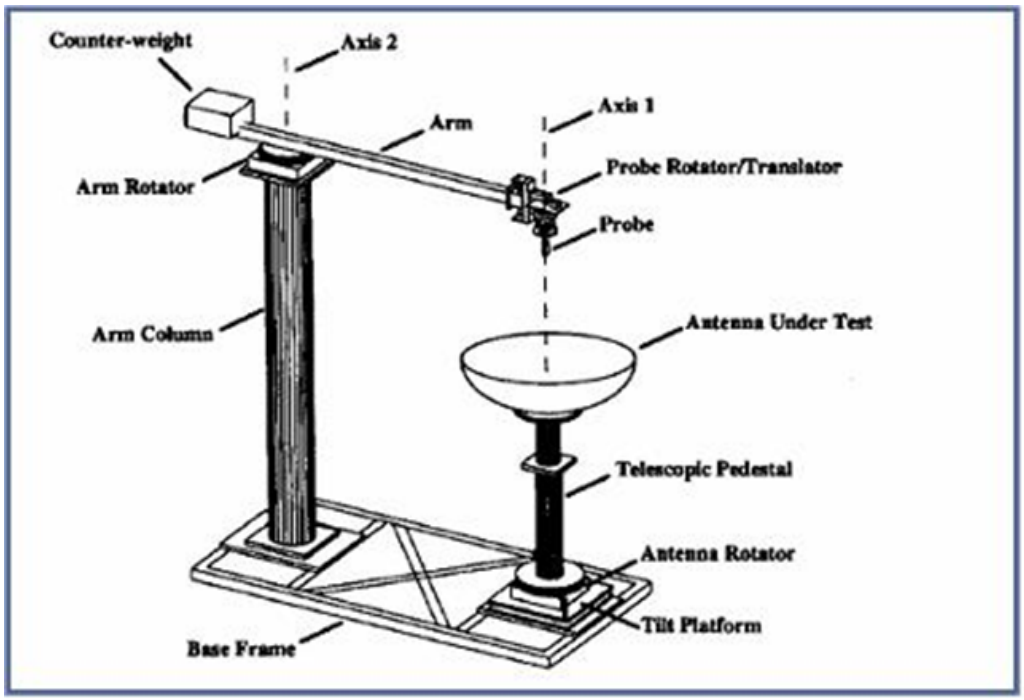

Figure 2.1: Standard implementation of the bipolar near-field scanner

$$y = L * \cos(\beta - \alpha) - \cos(\alpha) \tag{2.9}$$

'L' in these equations represent the length of the arm from the center of rotation of the AUT axis and the center of rotation of the ARM axis.

The standard measurement to obtain the data grid in Fig. 2.2 is usually conducted in the following manner: First, after the axes are initialized to zero degrees (meaning the probe is directly above the center of the AUT), a measurement is taken. Next, the arm moves out a pre-calculated distance $\Delta\beta$. The AUT axis then rotates around 360°, taking measurements at prescribed angles $\Delta\alpha$. After this ring is measured, the arm axis moves out to the next ring and that ring is measured. This continues until the extent of the desired scan plane is obtained.

The calculated angular distances used in the measurement is determined by sampling requirements for the NF-FF transformation, the AUT properties, and the measurement setup. The bi-polar sampling requirements are actually derived from the plane-polar sampling requirements [13]. The following equations are used

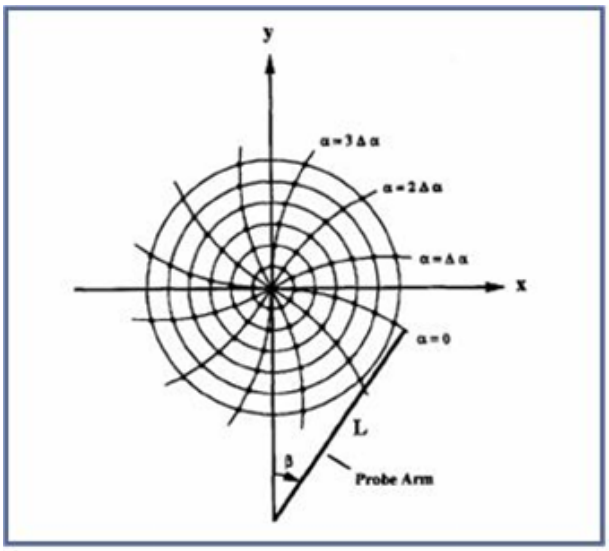

Figure 2.2: Scan grid for the bipolar scanner.

to determine the sampling spaces.

Plane-Polar Equations

$$\Delta\rho = \frac{\lambda d}{2a\chi_1\chi_2} \tag{2.10}$$

$$\Delta\phi = \frac{\lambda}{2a\chi_1^*\chi_2 \sin(\theta)} \tag{2.11}$$

where

$$\chi_1^*(\theta) = 1 + (\chi_1 - 1)(\sin(\theta))^2 \tag{2.12}$$

$$\theta = \tan^{-1}(\frac{\rho}{d}) \tag{2.13}$$

Bi-polar Equations

$$\Delta\alpha = \Delta\phi \tag{2.14}$$

$$\Delta\beta = 2\sin^{-1}(\frac{\rho + \Delta\rho}{2L}) - 2\sin^{-1}(\frac{\rho}{2L}) \tag{2.15}$$

Parameters:

λ : Free-space Wavelength.

ρ : Radial distance from origin.

ϕ : Angular variable.

d : Distance from AUT to Probe.

a : Minimum sphere enclosing the AUT aperture.

χ_1 : Excess Bandwidth Factor.

χ_2 : Oversampling Factor.

2.2.2 Post-Processing

After the measurement, data is organized by α and β points with amplitude and phase data on a plane above the AUT. Two polarizations of data are usually taken. If the measurement is conducted without phase, two planes and two polarizations of twice-oversampled amplitude data above the AUT is gathered. For processing the near-field data into the far-field, a number of techniques are available including the Fast Fourier Transform (FFT), Jacobi-Bessel, and the Fourier-Bessel techniques [14]. The first one, however, has emerged to be the most popular of the three. In fact, the original Bi-polar measurement system uses the FFT as its primary near-field to far-field transformation [15]. Unfortunately, since the data is in the bi-polar coordinate system, a direct FFT application is not available. An intermediate step is needed to transform the data from the bi-polar coordinate system to a regular rectangular grid, of which the FFT requires. To do this, an interpolation technique called Optimal Sampling Interpolation (OSI) is used.

Optimal Sampling Interpolation is a technique that converts the bi-polar data grid into the standard rectangular data grid. In general, the technique involves using several bi-polar grid data points (that surround the desired rectangular data point) to interpolate the desire rectangular data point. It uses a number of interpolating functions, such as the Dirichlet function, approximate prolate spheroidal function, and the Tschebyscheff polynomial, to accurately represent

the data on the rectangular grid. These functions have all been rigorously studied and proven to be quite accurate in [16]. More information on the OSI process can be found there.

With the measured near-field data represented on a rectangular plane, the data can then propagate to the far-field. This is done by employing a Fourier transform to convert the near-field data to the spatial frequency domain represented by the k_x and k_y space. We assume an $e^{j\omega t}$ convention for the electric field.

$$\vec{A}(k_x, k_y) = \frac{1}{2\pi} \int_{-\infty}^{+\infty} \int_{-\infty}^{+\infty} \vec{E}(x, y, 0) e^{j(k_x x + k_y y)} \, dx \, dy. \tag{2.16}$$

The result $\vec{A}$ is what is called the plane-wave spectrum (PWS), representing the linear superposition of plane-waves that construct the near-field data. In the case of discrete data (of which is taken in a measurement) a FFT function is used in place of the continuous Fourier transform. The far-field pattern has a direct relationship with the PWS that can be found by the simple asymptotic relationship [17]:

$$\vec{E}(r, \theta, \phi) = \frac{j e^{-jkr}}{r} k_{z0} \vec{A}(k_{x0}, k_{y0}) \tag{2.17}$$

where r is the radial distance to the far-field point, k is the free-space wave number, and:

$$k_{x0} = k \sin\theta \cos\phi \tag{2.18}$$

$$k_{y0} = k \sin\theta \sin\phi \tag{2.19}$$

$$k_{z0} = k \cos\theta \tag{2.20}$$

Furthermore, to convert the vector quantity $\vec{E}(r, \theta, \phi)$ into spherical coordinate components the following relationships can be used:

$$E_\theta(r, \theta, \phi) = j \frac{k e^{-jkr}}{2\pi r} (A_x cos\phi + A_y sin\phi) \tag{2.21}$$

$$E_\phi(r,\theta,\phi) = jk_{x0}\frac{e^{-jkr}}{2\pi r}(-A_x sin\phi + A_y cos\phi) \tag{2.22}$$

In addition to propagating to the far-field, the Fourier transform (and FFT) can represent the near-field on different planes above the AUT other than the measured plane as shown in Equation 2.18. These so called holographic projections are a vital diagnostic tool when characterizing antennas. Such images can help identify phase errors and cold-spots on the antenna and help understand how the aperture of the AUT is radiating. This property also is essential for the phase-retrieval algorithm used for phase-less measurements. This algorithm requires multiple fast iterations between two near-field planes above the AUT. The FFT is especially well-suited for this task.

$$\vec{E}(x,y,z) = \frac{1}{2\pi}\int_{-\infty}^{+\infty}\int_{-\infty}^{+\infty}\{\vec{A}(k_x,k_y)e^{-jk_z z}\}e^{-j(k_x x + k_y y)}\,dk_x\,dk_y \tag{2.23}$$

The final step of the conversion from near-field to far-field is to compensate for the probe. Since the probe is in the near-field of the AUT, the measured near-field is disturbed.

Thus, the final far-field pattern must be modified to eliminate this effect. This is done by compensating for the far-field probe pattern on the $\phi = 0$ and $\phi = 90$ cuts. When measuring, the probe is aligned to measure on these cuts. With knowledge of the pattern on these cuts, the effects of the probe can be accounted for and then eliminated from the AUT far-field pattern. Data on the probe pattern is usually based on a pattern model as in [18], or actual measured probe patterns. In our case, simulation data (presented in Appendix A) is used to obtain the probe pattern.

2.2.3 Phaseless Post-Processing and the Phase Retrieval Algorithm

One of the goals of this project was to implement the feature of phaseless measurements. The phaseless measurement, where only amplitude measurements are taken, was devised for the Bi-polar scanner by Yaccarino and Rahmat-Samii in [19]. It shows that with two planes of amplitude data above the antenna aperture if was possible to retrieve the unknown phase by an iterative Fourier algorithm starting from a standard initial guess. Furthermore, it is shown in [20], that the technique can be improved by using an evolutionary algorithm to determine a more appropriate initial guess.

Fig. 2.3 shows a diagram of the phase-retrieval algorithm [20]. The algorithm starts with two planes of amplitude data. The planes of data should be at least 2λ apart, however, in certain cases (as with the measurement of the standard gain horn in Chapter 5) it is possible to have planes only 1λ apart. The sampling requirements on each plane is determined by the requirements outlined in [19] and typically requires the oversampling factor to be twice the nominal value for full (amplitude and phase) measurements. This is due to the fact that the squared amplitude data, which is used for the OSI interpolation, is bandlimited to a band twice that of a full measurement.

The two planes of data are interpolated using Squared Amplitude OSI to obtain two rectangular grids of amplitude data. An initial guess for the phase is then applied to an aperture constraint that forces the amplitude of the field to be zero outside the given aperture and one inside the aperture. This initial field is placed on the AUT aperture plane (z=0). The field is then propagated to the second measured plane. The calculated amplitude of the field is then discarded and then replaced by the real measured amplitude data. The field is then propagated back to the first plane where the amplitude is stored separately and then replaced by the measured amplitude data. At this plane, the error metric is calculated by the

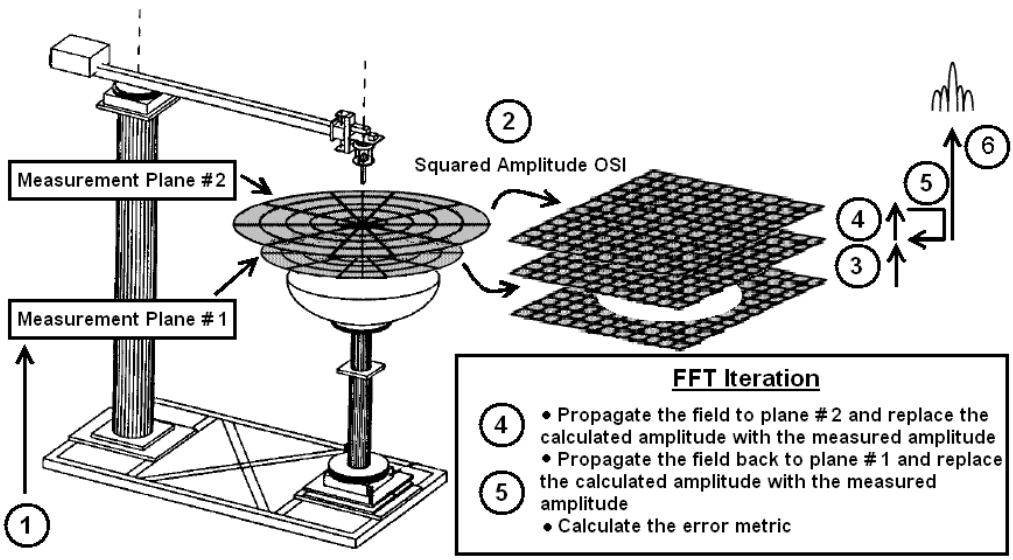

Figure 2.3: Standard procedure for the phase retrieval algorithm

following equation [20]:

$$e = 10log(\frac{\Sigma_{i,j}(|F_{i,j}| - M_{i,j})^2}{\Sigma_{i,j} M_{i,j}^2}) \tag{2.24}$$

where $F_{i,j}$ is the calculated field amplitude at point (i,j) and $M_{i,j}$ is the measured field amplitude at point (i,j) on the first plane. If the desired error level has not been reached, the field is then propagated back to the second plane where the process repeats until the desired error level is reached.

The phase retrieval algorithm describe here is based on the hybrid solution presented in [20]. More information on the Differential Evolutionary Algorithm (DEA) that governs the initial guess and the phase retrieval algorithm is found there.

2.2.3.1 Advantages

A couple of distinct advantages over full measurements emerge when using the phase-retrieval technique. The first is the mitigation of positional errors. Small

positional errors due to positioner over-shoot, rounding errors, etc., can effect the phase measurement significantly at millimeter-wave frequencies while the amplitude is not as sensitive. With phaseless measurements, the phase errors are not incorporated in the data and can help avoid these types of measurement error. The second advantage is the elimination of vector RF test equipment. The vector network analyzer used for the full measurements, which has the ability to measure amplitude and phase up to 67GHz, is the most expensive piece of the measurement system. In fact, it is about 5 times the total cost of the rest of the system. Such an expense is forbidden for most laboratories. Phaseless measurements, in contrast, only requires a signal and power (amplitude) measurements. A simple oscillator or frequency synthesizer and a power meter and sensor can be used, reducing the costs for appropriate equipment considerably.

2.2.3.2 Disadvantages

A couple of disadvantages emerge from this technique. First, the algorithm takes some time to process as it requires numerous iterations between the two planes before it can converge. This time can be anywhere from a minute to several depending on the data given. Second, the algorithm is not well-suited for some types of antennas such as broad-beamed antennas and steered beamed antennas. For the latter antenna type, the algorithm can be facilitated by a well-chosen initial guess, obtained by applying the DEA as presented in [20].

2.3 Infinite Array Analysis

A final topic of this prospectus involves the analysis of very large regular arrays of nanostructures. The number of elements in this array is on the order of ¿250,000. To analyze the behavior of such a large array, the infinite array model was employed. To analyze these infinite arrays, Floquet Analysis is used. It is

based off of Floquet's Theory, which allows for a solutions to the wave equation for structures that are infinitely periodic [21]. Consider a 1D periodic structure that has a spatial separation of distance d. This geometric periodicity forces the electromagnetic field, denoted by $f(x)$ to be periodic:

$$f(x+d) = Cf(x) \tag{2.25}$$

$$f(x+2d) = Cf(x+d) \tag{2.26}$$

$$f(x+3d) = Cf(x+2d) \tag{2.27}$$

$$\vdots \tag{2.28}$$

where C is a complex constant. Then in general: $f(x+nd) = C^2 f(x)$ and for a bounded C, $C = e^{-jkd}$. We can then define a periodic function $P(x)$, where:

$$P(x) = e^{-jkx} f(x) \tag{2.29}$$

Consequently,

$$P(x+nd) = P(x) \tag{2.30}$$

Thus, $P(x)$ is a periodic function in x with a period d (the same periodicity as the geometry). Since $P(x)$ is periodic in x, we can express it via a Fourier Series expansion:

$$P(x) = \sum_{n=-\infty}^{\infty} p_n e^{j\frac{2\pi n}{d}x} \tag{2.31}$$

Substituting for $P(x)$:

$$f(x) = \sum_{n=-\infty}^{\infty} p_n e^{jk_{x_n}x} \tag{2.32}$$

where $k_{x_n} = k + \frac{2\pi n}{d}$.

This results in an harmonic expansion of the field $f(x)$ that represents a spatial Floquet harmonic. It is both an infinite series and all terms propagate along the periodic axis. It is only presented in the 1D case here, however, it can be expanded to three dimensions with complex periodicity.

CHAPTER 3

1D Periodic Structures: Linear Antenna Arrays and Subarray Design Diagnostics

Large antenna arrays have many applications in space-borne antennas, radar, weather sensing, and communications. Often the design of these large antennas are difficult due to complications in array layout and feeding network design. One popular strategy to simplify design is to use subarrays as elements in the larger array. This allows the designer to concentrate on the smaller subarray design and use it as a repeating element throughout a large array. Depending on the size of the subarray, the feeding network complexity can be significantly reduced.

For two uniformly excited antenna array designs developed in [22, 23], subarrays were used as a building block to simplify the development and design of the beam-forming network. In both these cases, the final array pattern produced anomalous grating lobes that deteriorated the overall performance of the arrays. Since these arrays were designed for uniform excitation, grating lobes should have not appeared in the final pattern. To diagnose the source of these anomalies, an evaluation of the array configuration, the subarray design, and beam-forming network was conducted by the authors.

Array theory dictates that the pattern of an array using individual elements is the multiplication of the elemental pattern and the array factor (AF) determined by the spacing, amplitude, and phasing between the individual elements [5]. When using a subarray design, the pattern of the array is the multiplication of the elemental pattern, the subarray AF, and the AF determined by the spac-

ing, amplitude, and phasing between individual subarrays. In general, if identical excitation is supplied to each element of the array or subarray, the differences between the two situations should be minimal. However, if due to the design of the subarray the excitation is not identical between the two situations, distortions such as grating lobes can appear. Fig. 3.1 shows the different levels of AF synthesis. Each level acts independently of each other until they are combined together to create the final array pattern that is shown in Fig. 3.2. Any change in the pattern or AFs at each individual level can affect the outcome of the final array pattern. Such changes can manifest itself into asymmetries, changes in sidelobe levels, or the appearance of grating lobes; the last being the focus of this paper. The appearance of grating lobes usually originates in two specific level of array synthesis: The 'full array' level or the 'subarray' level.

Beam-scanning with arrays that use subarrays have specific issues that can create undesirable grating lobes in the antenna pattern. A well-known and understood issue, quantization, comes into play when feeding each of the individual subarray with progressive phase [6]. In this case, undesirable grating lobes appear due to the quantized nature of the phase along the inputs of each individual subarray (the full array level of Fig. 3.1) causing the antenna array gain and pattern to degrade. The error usually assumes that the subarray is an ideal uniform element of the array and does not contribute to the degradation of the final antenna pattern [9–11, 24]. In other cases, the subarray has strategic amplitude tapering or irregularities that can help improve the overall final array pattern [7, 8]. In any case, the subarray itself does not cause the appearance of grating lobes.

Since none of the situations above applied to the arrays in [22,23], our attention was then drawn to the configuration (excitation and location) of the individual antenna elements of the subarray (the subarray level of Fig. 3.1). In both subarray designs, the location of each element was clearly defined. In contrast, the excitation parameters of each element was potentially sensitive due to a myriad of

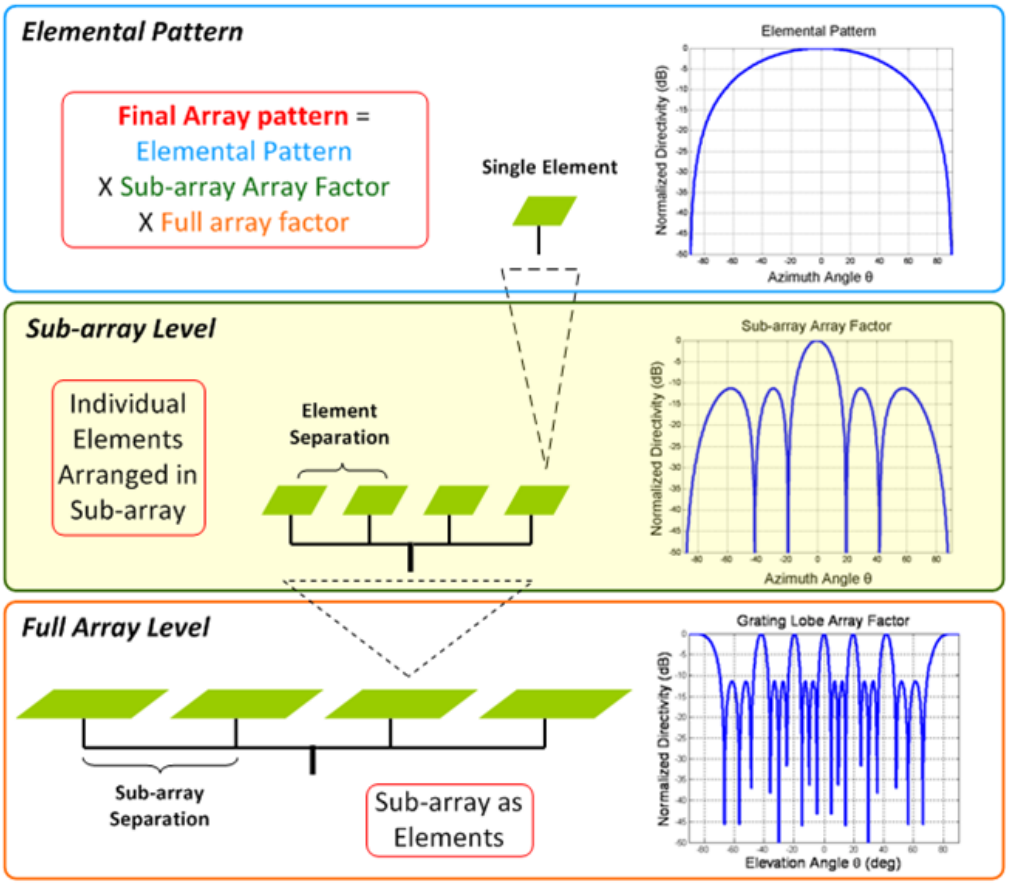

Figure 3.1: The three levels of array synthesis when using subarrays in an array antenna design.

possible issues such as feeding network errors, mutual coupling between adjacent elements or feed lines, fabrication tolerances, etc. These discrepancies in the excitation parameters were systematic: Errors that appeared in the subarray design was replicated throughout the full array. Thus, it was possible to evaluate and understand the systematic scenarios that caused errors in the subarray that ultimately manifested as grating lobes in the final array pattern. These evaluations lead directly to a diagnostic tool that was used to improve array and subarray design.

When applying uniform amplitude and phase to a linear array with elements less than a wavelength apart, there is no difference in the overall antenna pattern

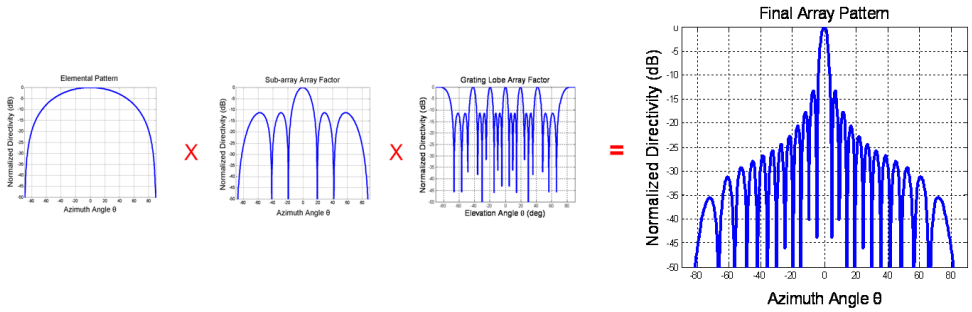

Figure 3.2: The multiplication of each pattern of the three levels produces the final array pattern.

if the array elements are excited as individual elements or as subarrays. In this ideal case each level of array synthesis aligns in a way that either avoids the appearance of grating lobes altogether (such as that with individual elements) or cancels the presence of the grating lobes (such as arrays that use subarrays). In arrays that use subarrays, the cancellation of these grating lobes is critical in providing an undistorted antenna pattern. Fig. 3.3 demonstrates how the grating lobes that appear in the AF on the full array level are cancelled. The dotted line, which represents the AF on the full array level, features grating lobes periodically throughout the pattern. The dashed line, which represents the AF of the subarray level, has nulls at the exact angles that the grating lobes appear at the full array level. Thus, when the two AFs are multiplied, the grating lobes are completely cancelled and form the AF shown as the solid line. This matching of the null of the subarray AF with the grating lobes of the full array level is what makes the final pattern identical to the case of individual elements [1].

Clearly, if this critical matching of the AFs at either the full array or subarray level were to be disturbed, then it is likely that complete cancellation of the grating lobes would not be possible and begin to manifest in the overall array pattern. Distortions of the AFs that could cause this can happen at both the full array and subarray level. Quantization lobes happen at the full array level, where

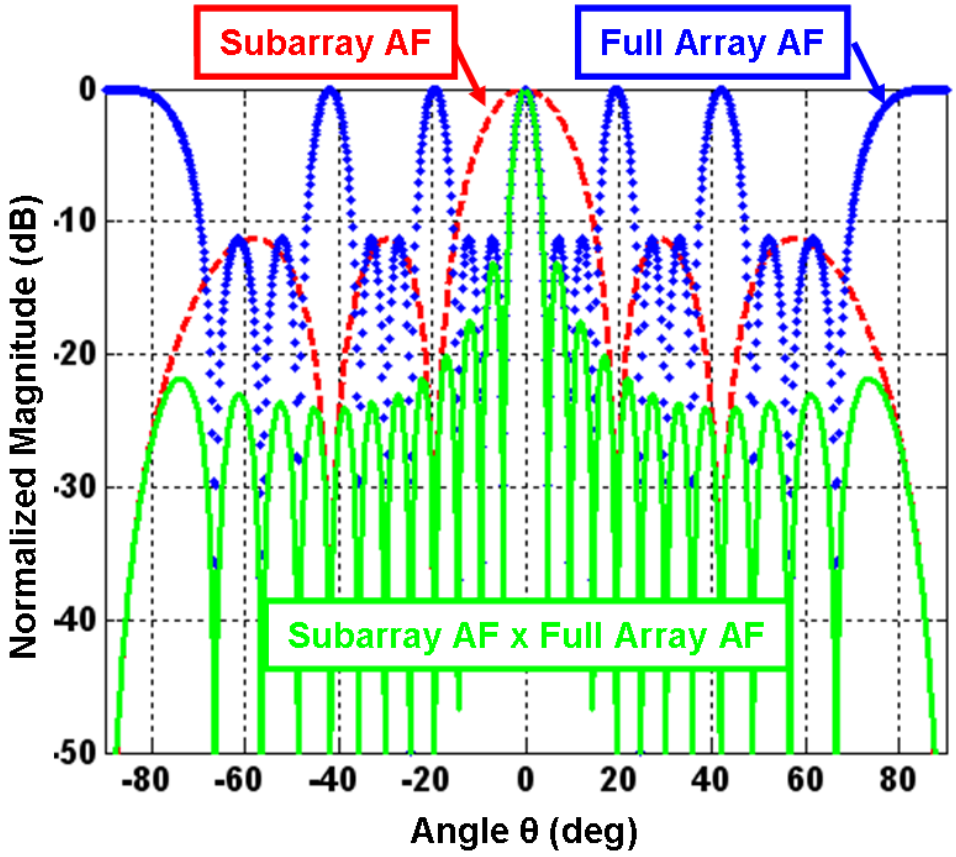

Figure 3.3: The matching of the subarray level AF (dashed line) nulls with the grating lobes of the full-array level AF (dotted line) to produce an unblemished array factor (solid line).

progressive phase at the input of the subarray elements would scan the grating lobe AF while the AF at the subarray level would remain stationary. Thus, the grating lobes would no longer match with the nulls of the subarray AF and would appear in the final array pattern. As described in [9–11, 24], many techniques have been devised to mitigate the appearance of these grating lobes. In these cases, the subarray itself exhibits uniform illumination or is designed with specific illumination so its AF prevents the appearance of grating lobes.

Distortions that can occur at the subarray level have received very little at-

tention in comparison. In this case, it is convenient to assume that the feeding at the full array level is uniform and its AF does not distort. Changes in the AF at the subarray level would then disturb the level or location of the nulls that are vital in cancelling the grating lobes. Since these are not random errors, precise evaluations of subarray distortions can be conducted to understand the possible grating lobe manifestations in the final array pattern; hence, providing a useful diagnostic tool.

Understanding the possible manifestations of distortions in the subarray and final array pattern can be a valuable tool in the diagnostics of the subarray design. The possible distortions have many sources that will ultimately manifest themselves in the amplitude and/or phase excitation at each element of the subarray. Thus, any possible distortions will be revealed in the subarray AF. Recognition of the distortions in the subarray AF is a valuable instrument to troubleshoot and compensate for errors. To the best knowledge of the authors, particular distortions that arise in the subarray AF has not been explicitly categorized, making it difficult to know which elements or what excitation component (amplitude or phase) is causing the distortions. For the antenna designer actively designing a subarray, this knowledge can lead to an immediate redesign, saving time and effort in the design cycle.

Another important outcome of this diagnostic tool is that the underlying cause of the excitation errors does not need to explicitly known. For example, if a subarray design exhibits a phase shift in the element excitation, it does not matter if it is cause by mutual coupling, inaccurate feedline lengths, or some other mechanism: The designer knows that the desired phase is not being achieved because it is evident in the subarray AF. The phase error can then be corrected by any technique to shift phase such as lengthening or shortening feed lines or shifting element positions. In essence, distortion design diagnostics allows for a valuable first-order check for a subarray design before it is incorporated in the larger array.

3.1 Subarray Design and Distortions

The AF of a 1xN subarray with variable amplitude and phase on each element can be expressed as the following equation [5]:

$$AF_{subarray} = \sum_{n=1}^{N} a_n \exp\{j[(n - [\frac{N+1}{2}])kd\sin\theta + \beta]\} \tag{3.1}$$

where N is the number of elements in the subarray, a_n is the amplitude of the individual elements, k is the free space wave number, d is the separation distance between individual elements, and n is the phase of the individual elements. Here we assume the coordinate system origin is at the center of the subarray.

This equation can plot any AF with infinite possible combinations of element separation, amplitude tapers, and phase distributions. To help guide the evaluations of subarray distortions, it is important to identify and characterize the most likely configurations and design of 1xN subarrays. Firstly, for our purposes here, we assume elements are uniformly spaced with no errors in position, since most modern design and fabrication can carefully control this and avoid any possible irregularity. Secondly, since the source of distortions is in the excitation of each element, the distortions will be classified by the type of beam-forming network that is exciting the subarray elements. They will be classified into two types: Parallel excitation and series excitation. As will be shown, each network has distinctive distortions that are indicative of excitation errors that lead to the appearance of anomalous grating lobes. Examples here will use 1x4 subarrays, however, the analysis is not limited to this number of elements and can be applied to 1xN subarrays.

3.1.1 Parallel Excitation

Fig. 3.4 shows an example of a 1x4 subarray that is excited in parallel. In other words, the inside two patches 2 and 3 and two outside patches 1 and 4 are excited separately from lines that originate from a single node point. Furthermore, the inside elements have identical but mirrored excitation configurations and the outside elements are excited with different (but identical and mirrored) excitation configurations. Thus, the inside elements and outside elements have the potential of having different amplitude and phase relative to one another. Although a microstrip subarray design is shown here, any subarray design where such an excitation scheme is used can be considered in this analysis.

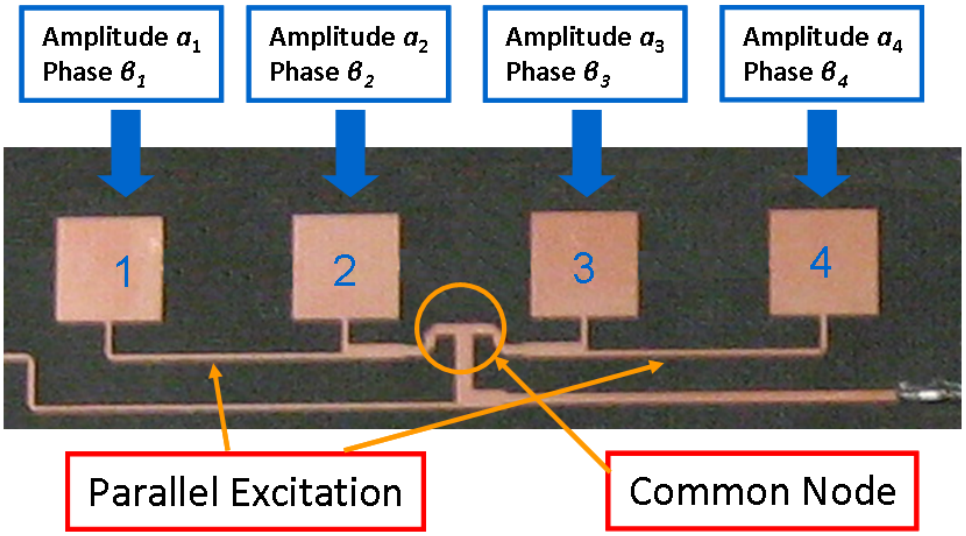

Figure 3.4: Example of 1x4 subarray with a parallel excitation configuration.

We can infer that for parallel excitation the following conditions would hold:

Amplitude:

$$a_1 = a_N, a_2 = a_{N-1}, a_3 = a_{N-2}, ... \tag{3.2}$$

Phase:

$$\beta_1 = \beta_N, \beta_2 = \beta_{N-1}, \beta_3 = \beta_{N-2}, ... \tag{3.3}$$

These conditions can allow us to evaluate and distinguish possible distortions for differences in amplitude and phase. The evaluations are done separately for clarity; it is certainly possible to have combinations of both amplitude and phase distortions simultaneously.

Fig. 3.5(a) shows the possible distortions the AF of a 1x4 subarray design excited in parallel with amplitude errors. A 1x4 subarray was chosen because they were used in [23], however, similar distortions are observed for 1x3, 1x5, and 1x6 subarrays. Fig. 3.5(a) presents four different AFs with different weights between the inside and outside elements. The ratio between the elements are labeled on each curve with '1' being no difference between the inside elements and outside elements (ideal uniform pattern) and '0.25' meaning that the outside elements 1 and 4 are one quarter the amplitude of the inside elements 2 and 3. (i.e. a1/a2 = 0.25.) The tapering of the amplitude brings down the side lobe levels as one would expect, but more interestingly, the first null actually begins to deviate or 'walk-off' from its original location. This null no longer cancels the corresponding grating lobe from the full array AF and causes those grating lobes to appear in the final array pattern. Fig. 3.5(a) also shows the combination of the AF at the subarray level and the full array level for the same taper values between the inside and outside elements. Indeed, grating lobes appear in the combination AF and would manifest in the final array pattern.

Fig. 3.5(b) presents the possible distortions the AF of a 1x4 subarray design excited in parallel with phase errors. It presents shifts in phase between the inside and outside elements of 0° (ideal uniform pattern) to 60° (i.e. $\beta_1 = \beta_2 + 60°$). In this case, the first nulls remain at the same angle, but instead begin to 'fill in'. Thus, when combined with the AF of the full array level, the nulls no longer completely cancel the grating lobes, but allow their signature to remain. This is portrayed in Fig. 3.5(b), where the combination of the subarray and full array AFs are shown. Clearly, the grating lobes appear where the subarray AF nulls

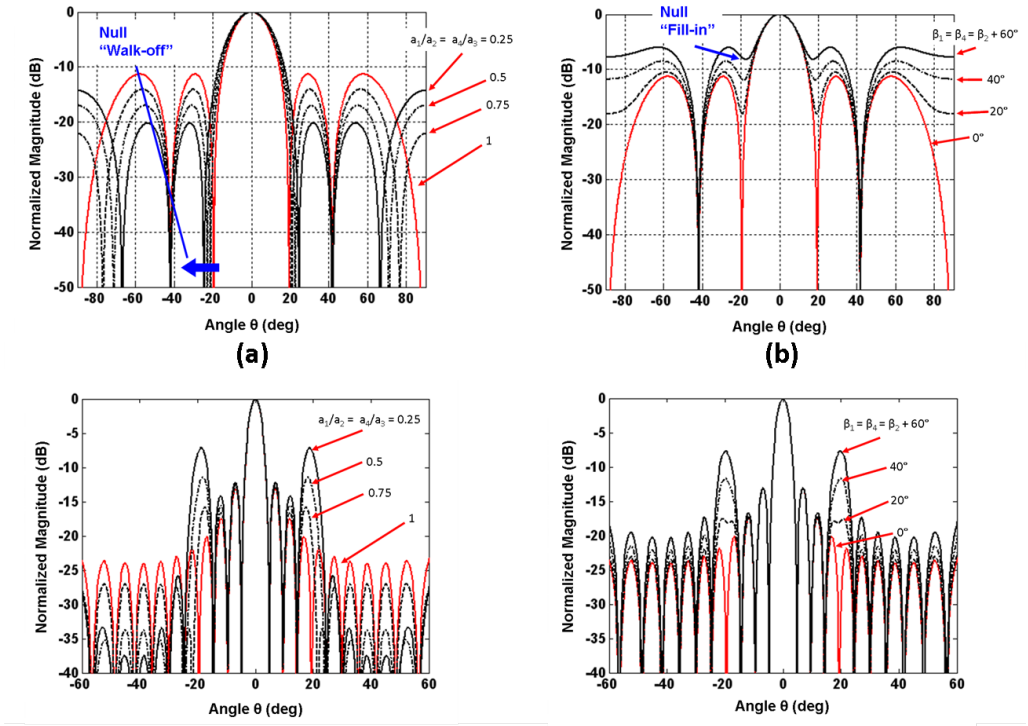

Figure 3.5: AF of a parallel fed 1x4 subarray and the multiplication of the subarray and full array AFs with different (a) amplitude tapers and (b) phase shifts between the inside and outside elements. Anomalous grating lobes become more severe as the amplitude and phase differences between the inside and outside elements becomes greater.

had filled-in.

3.1.2 Series Excitation

Fig. 3.6 shows an example of a 1x4 subarray that is excited in series. In a configuration like this, it can be deduced that the most likely errors to appear to be progressive amplitude and phase along the elements of the subarray.

A series excited subarray would have the following conditions:

Amplitude:

$$a_n = a_1 - (n-1)\delta a \tag{3.4}$$

Phase:

$$\beta_n = \beta_1 + (n-1)\delta\beta \tag{3.5}$$

where δa and $\delta\beta$ is the progressive amplitude difference and progressive phase shift between adjacent elements, respectively.

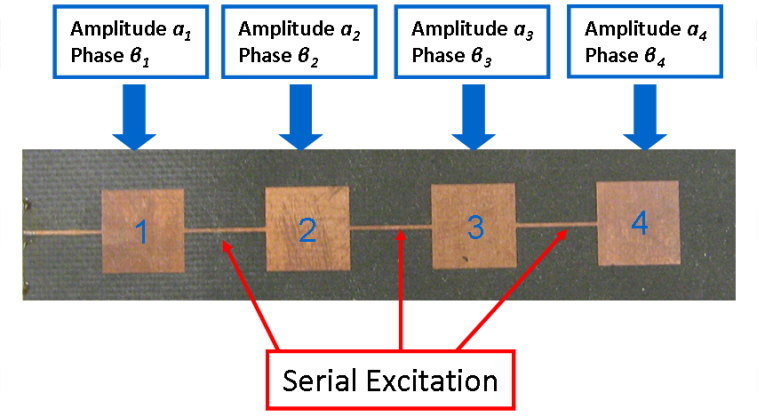

Figure 3.6: Example of a 1 x 4 subarray that is excited in series.

Fig. 3.7(a) illustrates the distortions of the AF of the subarray for progressive amplitude between adjacent elements. The AF pattern labeled '0' is the case of ideal uniform amplitude with the other patterns labels being the progressive drop in amplitude between each adjacent element. Here, one can see that the both nulls begin to fill in, very similar to the phase errors in the parallel case. The combination of the AFs of the subarray and full array levels are also presented in Fig. 3.7(a) showing the corresponding grating lobes.

Fig. 3.7(b) also displays the distortions of the AF of the subarray for progressive phase between adjacent elements. Each label corresponds to the phase shift between adjacent elements. Here the pattern begins to scan in the direction of the phase shift. Since the entire pattern shifts, the nulls that would cancel the corresponding grating lobes shift away as well and no longer cancel them. This is a similar example of null 'walk-off' as it was observed for the amplitude errors

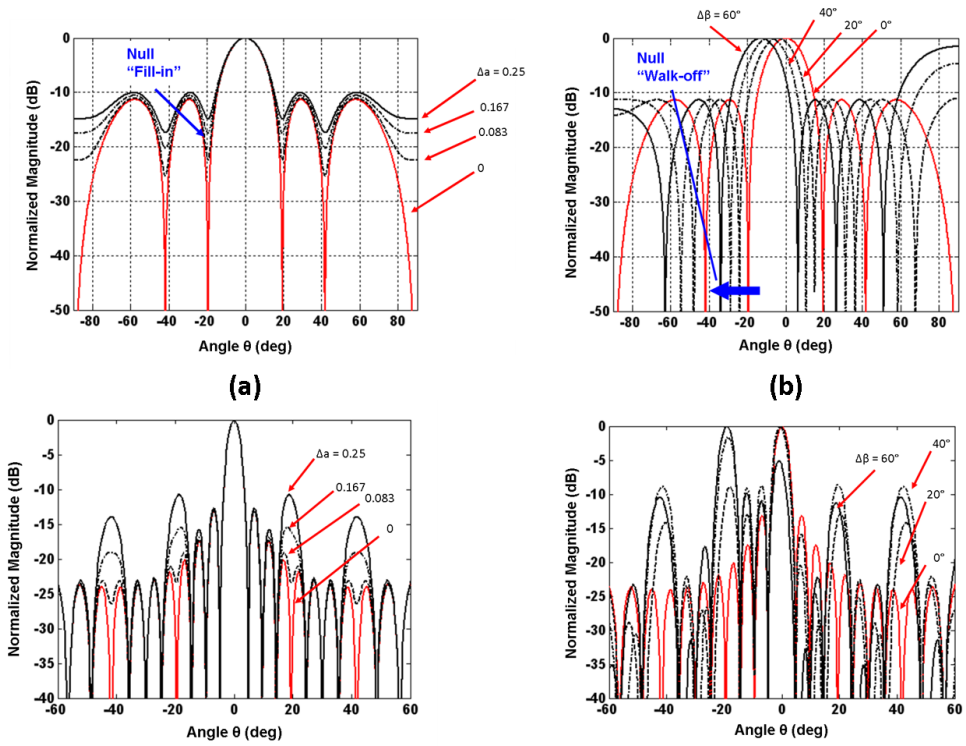

Figure 3.7: AF of a series excited 1x4 subarray and the multiplication of the subarray and full array AFs with different (a) amplitude tapers and (b) phase shifts between the adjacent elements. Anomalous grating lobes become more severe as the amplitude and phase differences becomes greater.

in the parallel excitation. Fig. 3.7(b) also illustrates the combination of the two AFs. Clearly, the grating lobes are not cancelled out and appear in the pattern.

It is interesting to note the opposite behavior of the pattern distortions between the parallel and series excitation cases. Errors due to amplitude exhibits null 'walk-off' in the parallel case, but exhibits null 'fill-in' in the series case. Phase errors exhibit null 'fill-in' for parallel feeds and null 'walk-off' for the series feed.

3.1.3 Other Excitation Schemes

The distortions categorized here represent only two possible excitation schemes that can be implemented. Further configurations, including irregular element spacing, not perfectly symmetrical or progressive errors, or combinations of amplitude and phase errors can be investigated and used for diagnostics by applying Eq. (1) and plotting the subarray AF. These plots can be used in the same manner as described in Section III to troubleshoot any potential issues in the subarray design.

3.2 Full-wave Analysis and Measurements of Subarray Design Diagnostics

All the evaluations in the previous section were calculated from the generalized AF. To verify the concept and incorporate any potential differences due to electromagnetic effects such as mutual coupling, a full-wave analysis on a microstrip patch antenna array was conducted. To facilitate the analysis, it was determined to design two antennas: First, an 'undistorted' uniformly excited 1x4 subarray with parallel excitation, and a second 'distorted' parallel excited 1x4 subarray design that was purposely distorted to have phase shifts between its inside and outside elements. Furthermore, an undistorted 1x16 and a distorted 1x16 array was designed using the corresponding 1x4 subarrays to demonstrate the grating lobe manifestations in a larger array.

Fig. 3.8 shows the two subarray designs. The undistorted design shown in 3.8(a) was designed to have close to uniform amplitude and phase for all the elements. The distorted design shown in 3.8(b) was designed to have a large phase shift that was accomplished by adding a bend in the line feeding the outside elements. The design operated at 13.4GHz.

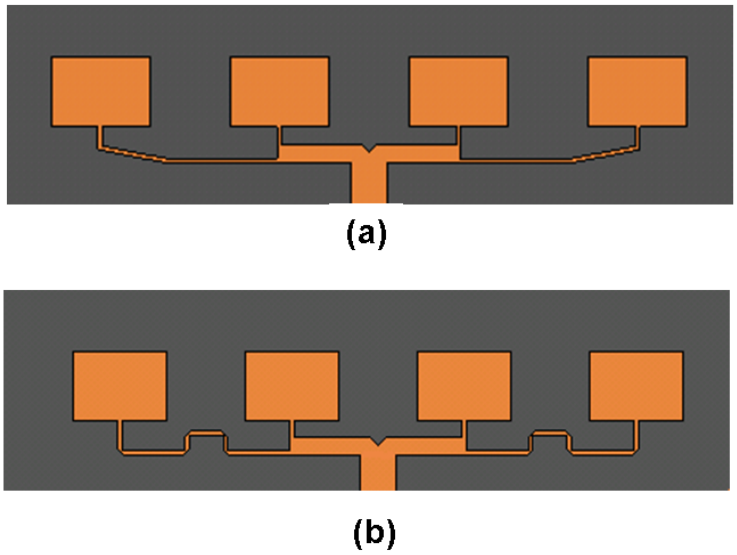

Figure 3.8: 1x4 subarray designs. (a) Undistorted design with no phase shift. (b) Distorted design with phase shift on the outside elements.

Each subarray design was analyzed in High Frequency Structure Simulation (HFSS) and their radiation patterns calculated. Fig. 3.9(a) and 3.9(b) shows the radiation patterns of the undistorted and distorted design, respectively. As predicted in the previous section, the null 'fill-in' effect for phase errors in a parallel excitation is clearly seen in the distorted subarray pattern, while the undistorted subarray has deeper first nulls. It would follow that this effect would manifest itself in the large array pattern as grating lobes.

These two subarray designs were then incorporated into separate 1x16 antenna arrays that were analyzed. Fig. 3.10 shows the 1x16 designs for the undistorted and distorted arrays. Care was taken in ensuring that uniform amplitude and phase was applied at the inputs of each individual subarray so to avoid any quantization error. The radiation patterns of each were then calculated. They will be shown in the following section where they will be compared with the measured results.

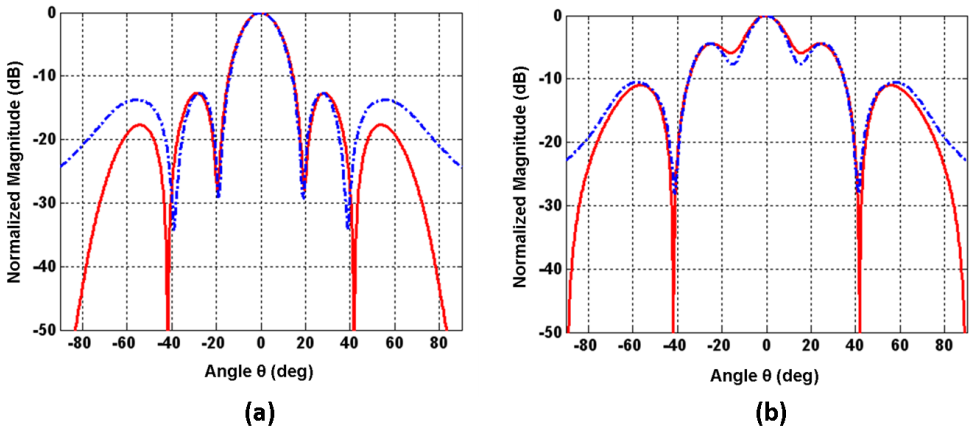

Figure 3.9: (a) 1x4 Undistorted Subarray design radiation pattern compared with corresponding analytical radiation pattern. The deeper 1st null is observed that will cancel out the corresponding grating lobe. (b) 1x4 Distorted Subarray design radiation pattern compared with corresponding analytical radiation pattern. The phase shift between the inside and outside elements of the subarray was 70°.

The two 1x16 designs simulated in the previous section were fabricated to verify the appearance (or the lack) of grating lobes. The fabricated arrays are shown in Fig. 3.11. They were etched on Rogers Duroid 5880 that was 0.7874mm thick. Both designs used a probe fed design that featured a SMA connector on the backside of the array. Both were measured in UCLA's Spherical near-field antenna range at the operating frequency of 13.4GHz.

Figs. 3.12(a) and 3.12(b) present the measured array pattern compared to the corresponding simulated array pattern. Fig. 3.12a is the comparison of the undistorted array measured and simulated pattern. In this case, we expect the pattern to show no grating lobes, as the subarray design was designed to exhibit uniform amplitude and phase as shown in Section IV. This is clear in the pattern that the grating lobes have been suppressed as expected in the array synthesis.

Fig. 3.12(b) presents the comparison of the distorted array measurement and simulation. Here we expect the appearance of grating lobes due to the null fill-in

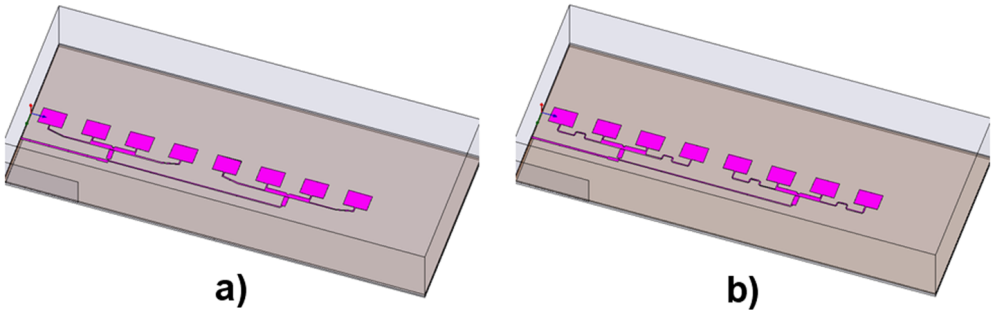

Figure 3.10: Simulated 1x16 arrays. Both are truncated at the center of the design and symmetry was enforced in the analysis. a) Undistorted design b)Distorted design.

effect. Indeed, the pattern features grating lobes at the predicted angles as the simulation, confirming the effect of the phase shift in the subarray design.

The appearance of undesirable grating lobes in antenna arrays that use subarrays is potentially caused directly by distortions in the subarray AF. These distortions arise due to excitation errors in the subarray design. Depending on the pattern of these errors, it is possible to diagnose and correct any distortions before the incorporation of the subarray in the array design. This chapter has categorized and demonstrated the distinct and systematic subarray AF distortions caused by the parallel and series excitation configurations and their particular manifestations in the final array pattern. These distortions were demonstrated with analytical AF calculations, full-wave electromagnetic analysis of both 1x4 subarray designs and 1x16 linear array designs, and finally representative measurements using a Ku-band 1x16 linear array. In general, the distortions consisted of two distinct occurrences, the first being 'null walk-off' where the nulls of the subarray AF changes its position in relation to the corresponding grating lobe, and the second, 'null fill-in', where the nulls of the subarray AF becomes non-zero, preventing complete cancellation of the corresponding grating lobes. Familiarity

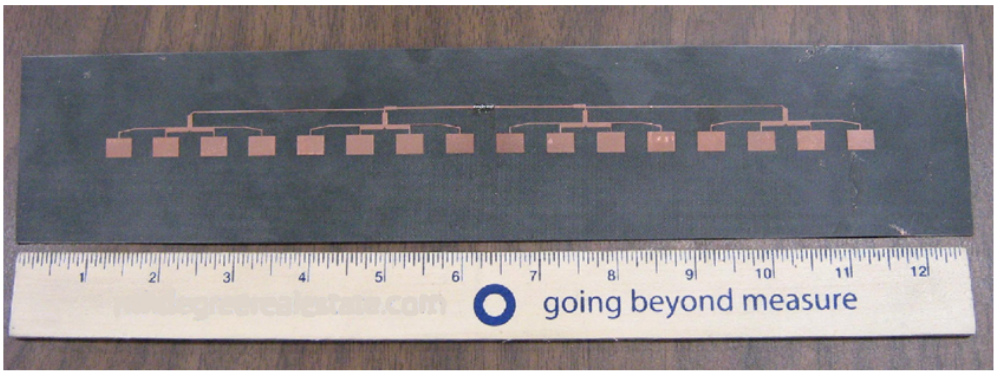

(a)

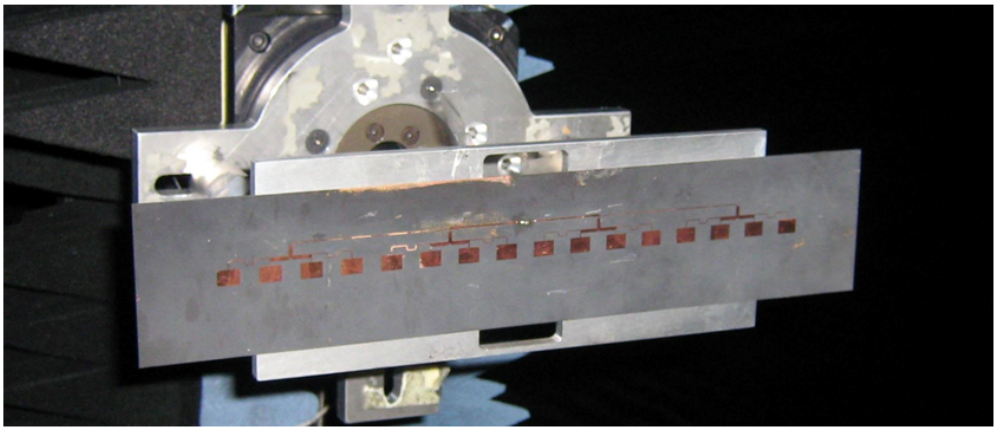

(b)

Figure 3.11: 1x16 Linear arrays fabricated for the representative measurements. (a) Undistorted array design. (b) Distorted array design.

with these distinct distortions allows for array designers to understand and prevent subarray design errors before they are used in larger arrays, saving valuable time and effort in the design cycle. In addition, current array designs that feature grating lobes can be efficiently diagnosed and corrected using this technique.

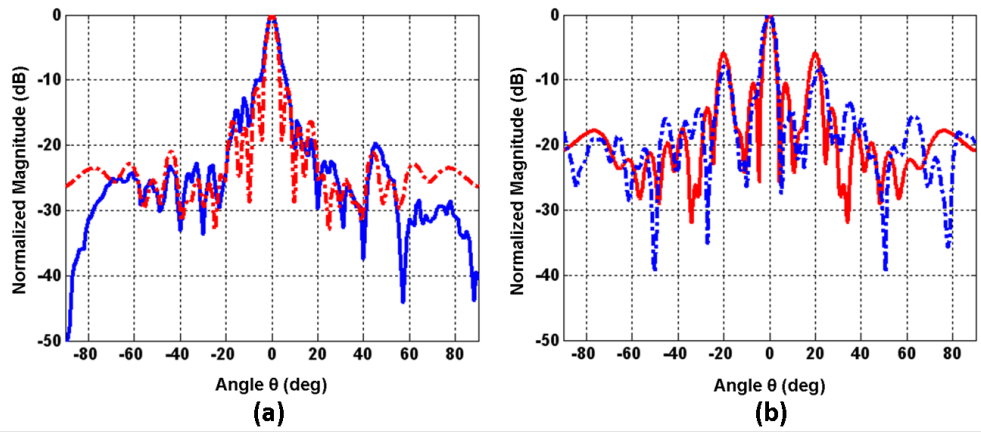

Figure 3.12: (a) Comparison of simulated (dashed line) and measured (solid line) patterns of the undistorted 1x16 linear microstrip array. (b) Comparison of simulated (solid line) and measured (dashed line) patterns of the distorted 1x16 linear microstrip array clearly showing the presence of grating lobes.

CHAPTER 4

2D Periodic Structures: Planar Microstrip Array Design using the Subarray Design Diagnostic Technique

The subarray design diagnostics described in the last chapter can be applied directly to 2D antenna array designs. In this chapter, a direct application of the subarray design diagnostic technique will be shown the design of an uniform illuminated Ka-band planar array that uses series excited 1x4 subarrays [25]. The design, simulations, and fabrication of this array will be addressed in this chapter. The measurement of this array will be addressed in the next chapter, as the measurement of this array and others like it lead to interesting research that is more specific to antenna measurement in general.

4.1 Planar Rectangular Microstrip Antenna Arrays using Subarrays

The subarray design diagnostic technique describe in the previous chapter was the result of analyzing a number of planar rectangular microstrip antenna arrays featured in [22], [23], and [26]. The Ka-band array in [26] was a design that used a parallel excited subarray that exhibited features of null fill-in. This observation was used in the formation of the diagnostic technique described in the previous chapter. Verification of the diagnostic technique was conducted using the 1x16

planar rectangular microstrip array in [12] that again used a parallel excited subarray. To verify the diagnostic technique for series fed subarrays, a new planar array design was devised that feature 1x4 series excited arrays. Fig. 4.1 shows the fabricated array that is featured in this chapter. This 8x8 rectangular microstrip array operates at Ka-band which features sixteen 1x4 series-excited subarrays. It was designed to be place on Rogers 5880 Duroid substrate that was 0.7874mm thick. To demonstrate the use of subarray design diagnostics the following steps were conducted: (1) Design of individual rectangular patch. (2) Design of series 1x4 subarray using subarray design diagnostics. (3) Design of overall 8x8 array. The second step is the most critical step in the design and exhibits a potential procedure to apply design diagnostics.

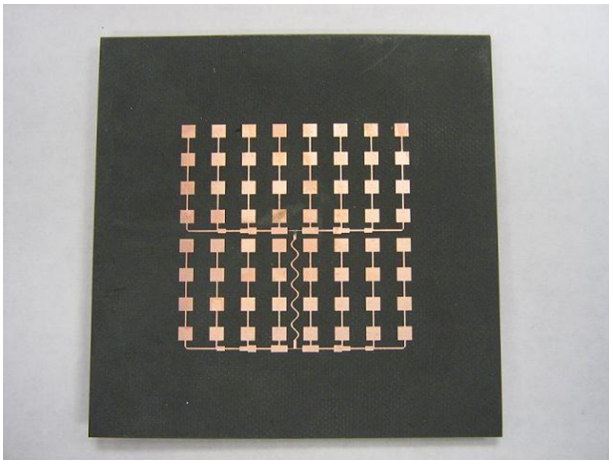

Figure 4.1: Fabricated 8x8 Ka-Band planar microstrip array featured in this chapter.

4.1.1 Design of Individual Ka-band Rectangular Patch

Fig. 4.2(a) shows the rectangular patch design used in the Ka-band array. Its dimensions where designed to be 3.25mm by 2.225mm and resonant at 36.1GHz. This patch was simulated in HFSS and its return loss plotted in Fig. 4.2(b). The edge impedance was 150Ω. Using this base design, the 1x4 subarray was designed.

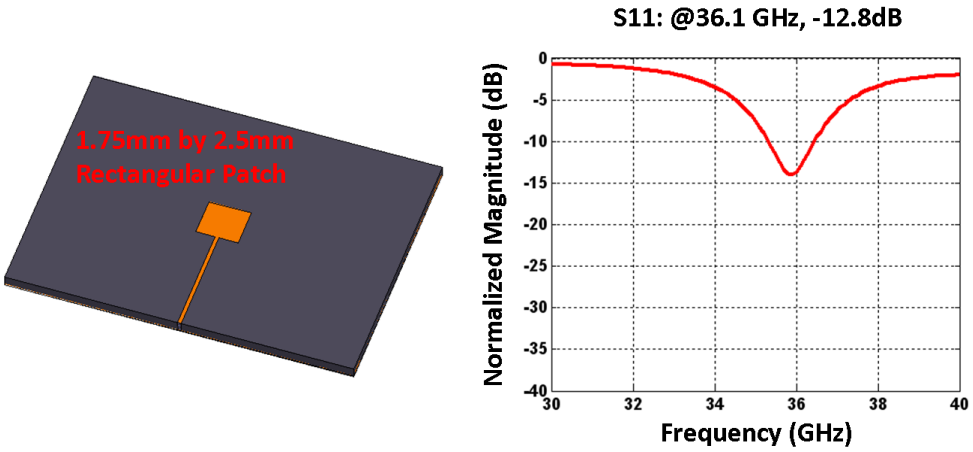

Figure 4.2: Single Ka-Band planar microstrip patch and its return loss.

4.1.2 Design of a 1x4 Series-excited Subarray using Design Diagnostics

To create a series excited subarray, a single feed line was placed in line with 4 rectangular patches that were separated by $0.5\lambda_0$ at 36.1GHz. The initial design with patch and line dimensions is shown in Fig. 4.3(a). It was then simulated in HFSS and its return loss and radiation pattern (principal cuts) plotted in Fig. 4.3(b) and 4.3(c), respectively. These results were not satisfactory for the design as the resonant frequency of the patches were shifted (likely due to the mutual coupling between the elements) and the radiation pattern exhibited a large beam tilt in the 0° cut. A redesign of the patch dimensions and array configuration was conducted to correct these issues.

4.1.2.1 Resonant Frequency Correction

The resonant frequency of the subarray was corrected by adjusting size of the rectangular patch. By fixing the feed line at a width with a characteristic impedance of 144Ω, the patch size was adjusted to resonant close to 36.1GHz. The size was found to be 2.65mm by 2.5mm. The new subarray with the resized patches are shown in Fig. 4.4 along with its return loss plot.

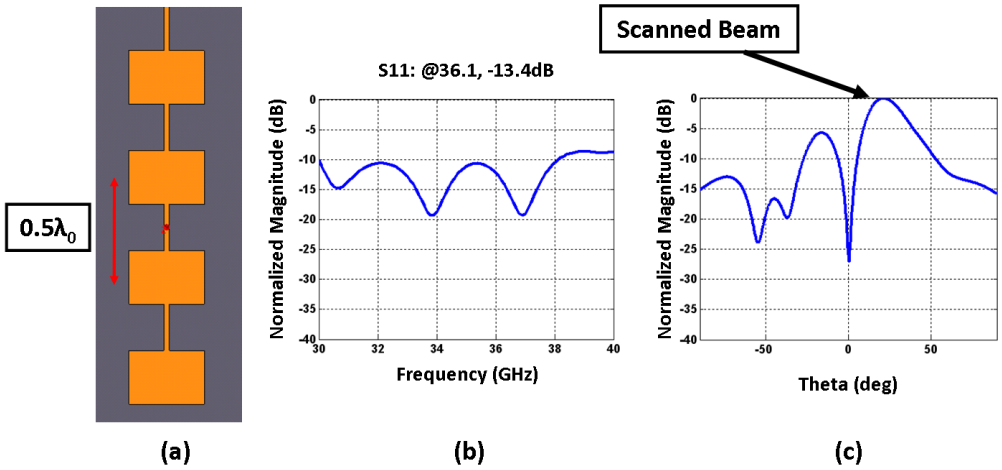

Figure 4.3: Initial design of the Ka-Band planar microstrip 1x4 subarray. Due to errors in the subarray design, the main beam of the radiation pattern is scanned severely in one direction.

4.1.2.2 Correction of Beam Tilt using Subarray Design Diagnostics

The major issue with the initial subarray design was that the radiation pattern exhibited a significant beam tilt. To correct this, the design diagnostics developed in the previous chapter were applied. For a series-excited subarray, a beam tilt in the subarray radiation pattern is caused by progressive phasing errors between adjacent elements. Thus, the phasing between the elements had to be adjusted so that each patch had equalized phase. There were many options that could have been employed to do this. One option would be to lengthen the feed lines between each patch by adding bends of some kind. Another option would be to add lumped inductors or capacitors along the feed line between the patches. A third option is to adjust the spacing between the elements so that the phase between them changes. This third option was ultimately chosen because it was the most practical option.

A parametric set of separation distances were simulated and the radiation patterns generated as shown in Fig. 4.5. As expected, as the phasing between

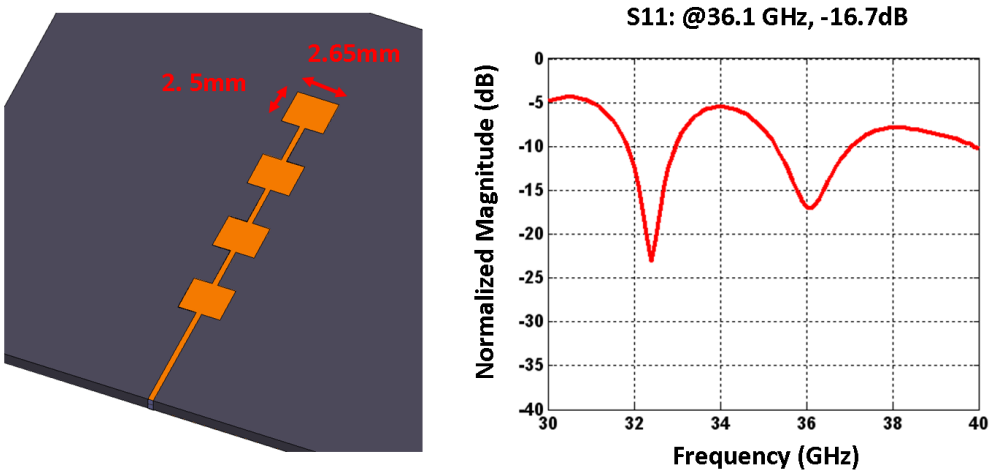

Figure 4.4: Redesigned Ka-Band planar microstrip 1x4 subarray and its simulated return loss. Patches were re-sized and re-spaced to correct for the errors found in the initial design.

the elements changed, the beam maximum scanned. At a separation distance of 0.625λ, the radiation pattern was maximum at broadside. In addition, the first and second nulls remained very deep, indicating that null fill-in was not occurring.

As was described in the previous chapter, recognition of the subarray pattern distortion led to an immediate redesign of the subarray so that to ensure a proper pattern before a full array was designed. A similar procedure can be conducted for any array design that uses subarrays; saving time and effort in the development of the array. With confidence that the subarray design is designed properly it was possible to design the complete 8x8 array.

4.1.3 Design of Overall 8x8 Rectangular Array

To create an 8x8 array, sixteen 1x4 subarrays were arranged in 2 rows as shown in Fig. 4.6. The feed origin of the array was at the center of the array and a feed network was designed to feed each subarray uniformly. The symmetry of the design allowed for identical (but mirrored) feed lines to be used on each quadrant

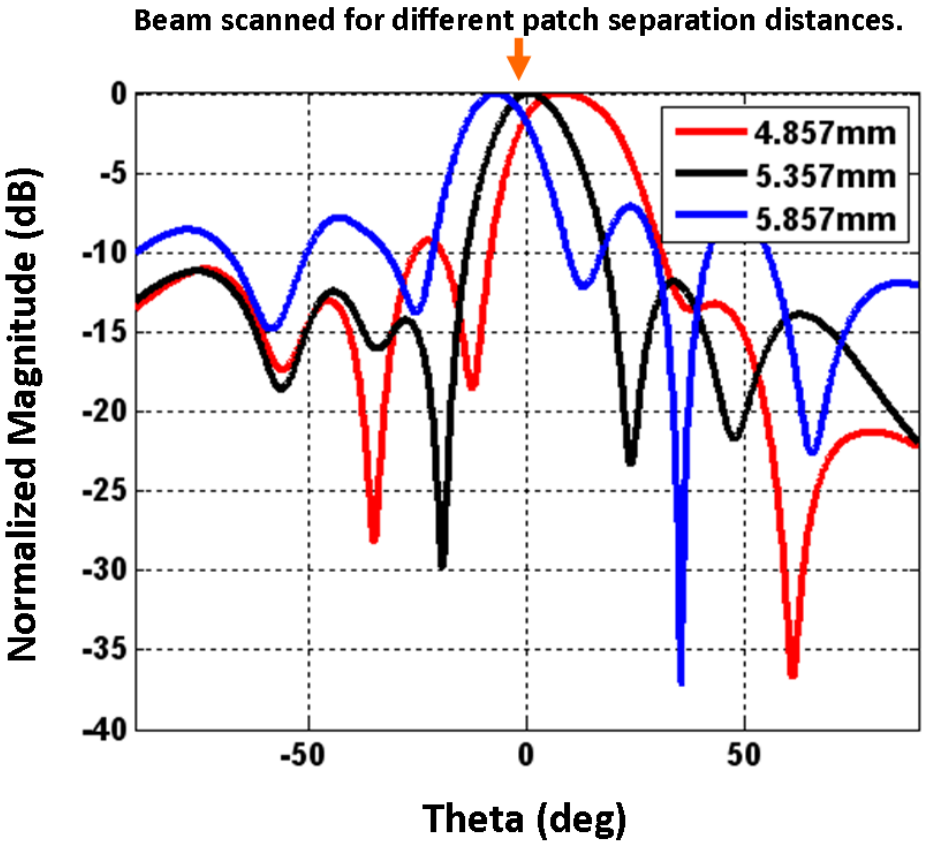

Figure 4.5: Radiation pattern of 1x4 subarray showing how different patch separation distances causes the main beam to scan. The correct spacing found to produce a proper subarray radiation pattern was 5.357mm.

of the array as shown in Fig. 4.7. With them in place, the only line to design was the line from the feed origin to the feedline label 'B' in Fig. 4.6. The design of this line was more difficult due to the fact that a straight line did not provide equal phasing between feedlines 'A' and 'B'. To equalize the phase, the line had to be meandered in a sinusoidal manner.

The complete design was then fabricated on the Rogers 5880 Duroid substrate using UCLA's fabrication facilities. To feed the array, a GPPO connector was used and fed through the back of the substrate. The next step was to verify its performance with a measurement using UCLA's Millimeter-wave Bipolar Planar

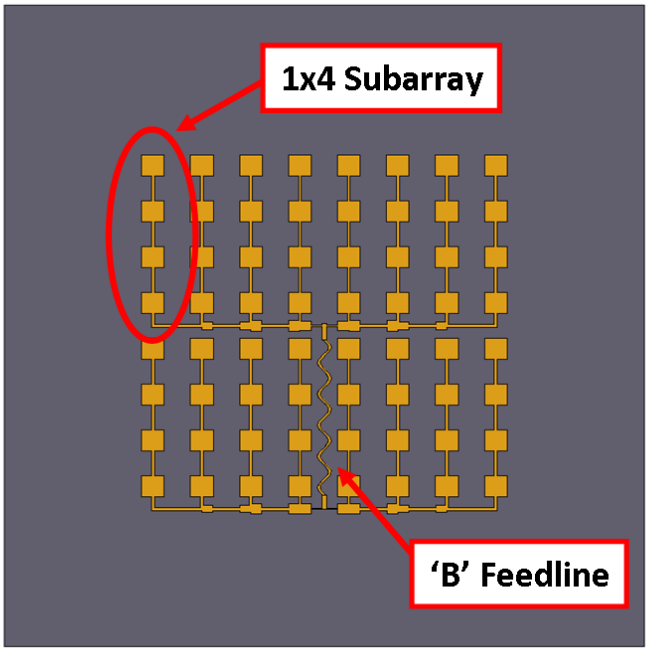

Figure 4.6: 8x8 antenna array design. Sixteen 1x4 subarrays were arranges in two rows of eight.

Near-field Measurements system. A near-field measurement was conducted and the far-field pattern generated. The primary cuts (H-plane and E-plane) are shown in Fig. 4.8. The directivity of antenna was 24.23dB. The beamwidth was 7.52° and 9.02° for the H-plane and E-plane, respectively.

The next chapter will again revisit this antenna array. Instead of focusing on the array design, the next chapter will discuss several near-field antenna measurement developments that was a natural extension of the array research. In particular, novel scanning techniques and developments in phaseless measurements.

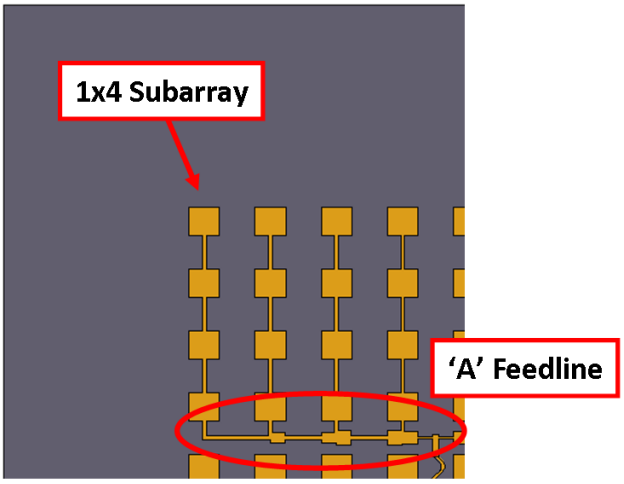

Figure 4.7: Main feed line for the antenna array. This is mirrored for each wing of the array.

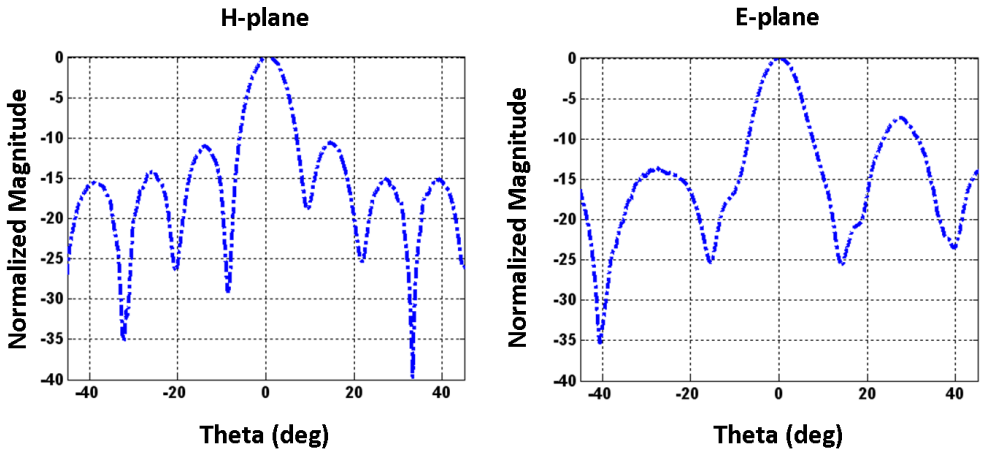

Figure 4.8: Measured H-plane and E-plane far-field cuts 8x8 antenna array design.

CHAPTER 5

Antenna Array Measurements: Planar Bipolar Measurements

The Millimeter-wave Bipolar Planar Near-field Antenna Measurement System, shown in Fig. 5.1, was designed as an antenna range that could measure physically small directive antennas that operated at millimeter-wave frequencies. This fact allowed the design to be relatively small and compact. Moreover, the bi-polar scanning technique, previously developed at UCLA, offers advantages in the same respect. In particular, bipolar scanning offers space-saving features that help reduce the footprint of the system and also eliminate linear motion, simplifying the mechanical complexity and design implementation [27]. These advantages made this technique preferable over other planar techniques such as plane-rectangular or plane-polar scanning.

With the unique compact design of the system, it became possible to place it on top of a standard optical table in the Center for High Frequency Electronics at UCLA. The optical table, with a grid of mounting screw holes, became an ideal place to mount (and conveniently dismount) the scanning apparatus of the measurement system. To reduce costs, the scanner itself was designed around standard, off-the-shelf positional equipment and the structural components were constructed in-house. The scanner structure was also designed to be modular, allowing for simple assembly and modification. The structure is hollow and allows the cabling to pass through and be hidden from the rest of the chamber. As constructed, it only has a footprint 22 inches by 6 inches and is only 20 inches

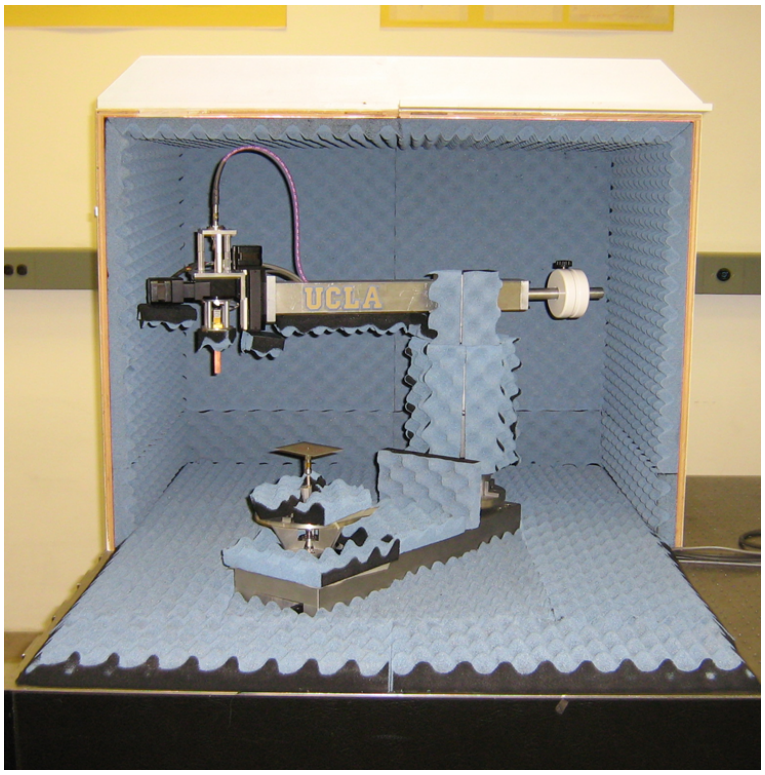

Figure 5.1: UCLA's Millimeter-wave Bipolar Planar Near-field Antenna Measurement System

tall. The two main axes of the arm and AUT sit 16 inches apart. It is surrounded by an enclosure that is also mounted on the optical table. The enclosure is lined inside with copper-shielding which is covered by 1.5 inch convoluted absorber designed for high frequencies. The absorber is also placed on the optical table, surrounding the scanner base and wedging against the edges of the enclosure. Absorber is also fitted on the scanner itself, isolating the scanner structure from the rest of the chamber. An image of the scanner inside the enclosure and many of the major dimensions of the system is shown in Fig. 5.2.

As built, the system offers a number of important specifications and features. First, the desired frequency range for the system is 26.5 GHz to 67 GHz, with options to expand to 110 GHz. The maximum antenna width that the system can accommodate is 24 inches. The maximum antenna height is 6 inches and

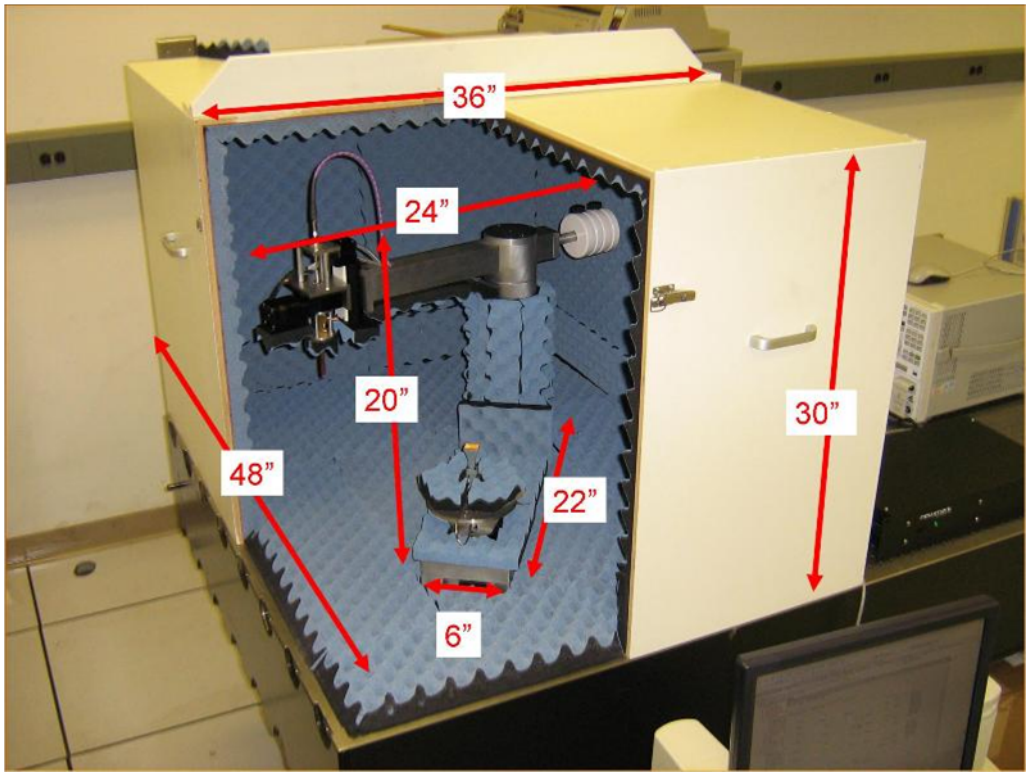

Figure 5.2: Major dimensions of the MMW Bipolar Scanner.

the maximum antenna weight is 75 lbs. The scanner can measure a scan plane of 60 inches in diameter and the probe can be translated vertically 1.5 inches. The system would be designed to be portable and compact and would include integrated custom software for measurement control, algorithms for near-field to far-field processing, and the option of phaseless measurements. The last feature was foremost of the options for this chamber because of its usefulness at millimeter-wave frequencies.

This system has been used to measure antennas at Ka-Band, V-band, and W-band with excellent results [27] and was a perfect fit to measure the Ka-band 8x8 antenna array that was designed in the previous chapter.

5.1 Conventional Measurement of Ka-Band Antenna Array

The Ka-band antenna array design was intended to serve a number of purposes related to antenna array design and measurement. The first purpose was to demonstrate the procedure of the subarray design diagnostic technique. The array also was design for the purpose of demonstrating new bipolar measurement techniques, the first being bipolar spiral scanning and the second was to was phaseless measurements at millimeter-wave frequencies.

To begin, a conventional measurement of the Ka-Band array was conducted to provide a baseline for the antenna pattern. The measurement was conducted at an operating frequency of 31.2GHz and scanned using the conventional stepped bipolar technique as described in [15]. The measurement took 7 hours to complete. The measured near-field amplitude and phase of both the Co-polarized and Cross-polarized fields are shown in Fig. 5.3. This data was then propagated to the far-field. The E-plane and H-plane cuts of the array are shown in Fig. 5.4. In addition, the data was then back-projected onto the aperture plane of the antenna array and it is shown in Fig. 5.5. It can be seen that the amplitude and phase distribution is close to uniform as was designed.

5.2 Spiral Scanning for the Bipolar Planar Measurements

Sampling requirements for antenna measurements at millimeter-wave frequencies often lead to long measurement times due to the large amount of data points required. In the case phaseless measurements, the doubling sampling requirement and four measurement near-field planes [19] of data that are required for the phase retrieval algorithm can quadruple the measurement time over that of a conventional measurement. For the Ka-Band array measured here, a phaseless

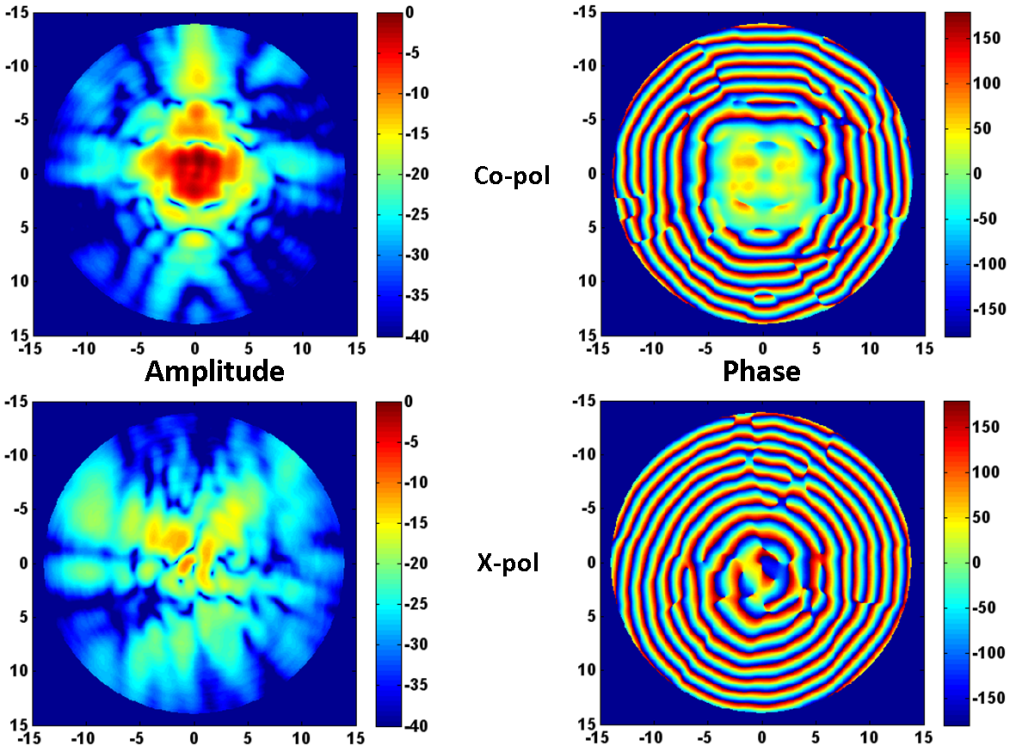

Figure 5.3: Copolarized and Cross-polarized near-field images of the 8x8 Ka-Band array.

measurement would take upwards of 28 hours to measure, potentially reducing the accuracy of the measurement due to drift or other errors. To help reduce the measurement time, new schemes in planar scanning had to be investigated, implemented, and demonstrated.

The most natural and rapid mode of scanning for the bipolar scanner involves simultaneous and continuous motion of both the arm and AUT rotational axes of the bipolar scanner show in Fig. 5.6. This motion results in a data grid with a spiral geometry. The first implementations of this spiral scanning have used a linear spiral geometry, where uniform spacing between subsequent radial rings is present on the same polar azimuthal angle as shown in Fig. 5.7(a) [28]. However, implementation of this geometry in a continuous mode is complicated for the bipolar scanner because it requires non-uniform velocity for both rotational axes

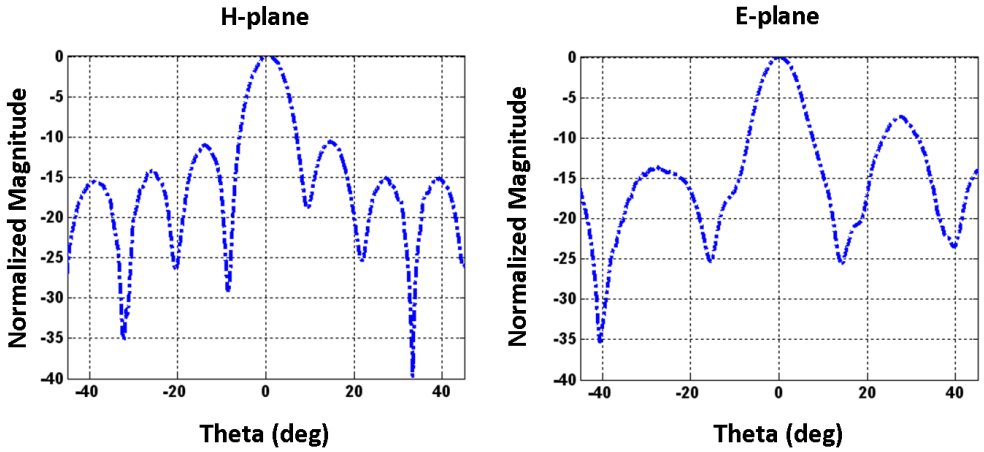

Figure 5.4: H-plane and E-plane far-field cuts of the 8x8 Ka-Band array.

during the measurement. In most cases, this complication would prevent any type of true continuous mode measurement from being implemented due to hardware limitations.

The second and recently developed implementation involves continuous and uniform motion of the two rotational axes. The resultant spiral data grid does not form a linear spiral, but instead forms what we call a 'bipolar' spiral. This bipolar spiral geometry differs from the linear spiral due to the fact that it exhibits uniform spacing between subsequent radial rings along the bipolar azimuthal angle shown in Fig. 5.7(b). This bipolar geometry with its simple implementation avoids the inherent issues with linear spiral geometry with the bipolar scanner and is the preferable mode for measurement for all possible scanning geometries using the bipolar scanning technique.

The following subsections will describe implementations of both continuous linear and bipolar spiral scanning for the Millimeter-wave Bipolar Planar Near-field Antenna Measurement system. Verification of the use of these techniques are also presented.

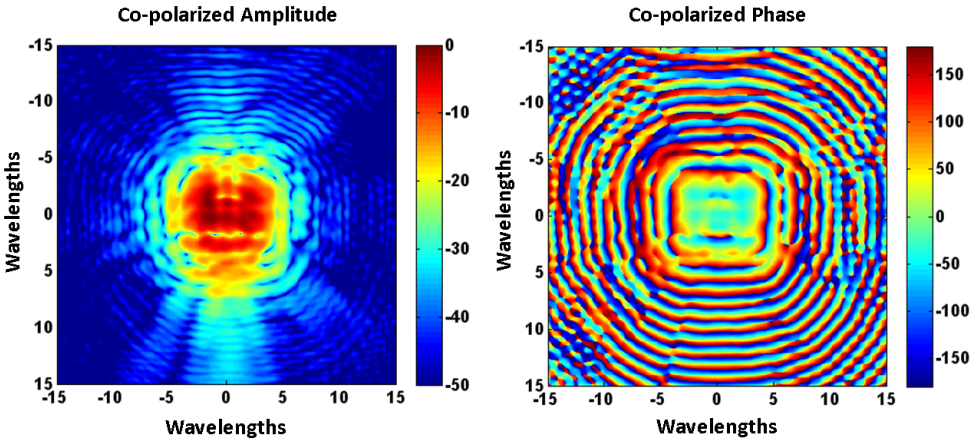

Figure 5.5: Back-projection holograms for the Co-polarized field at the aperture of the antenna array.

5.2.1 Continuous Linear Spiral Scanning

The linear spiral is geometrically achieved in the bipolar and plane-polar coordinate systems by linearly coupling the azimuth and radial axes. It is mathematically described in plane-polar coordinates by the following equations:

$$\rho_{nm} = \frac{\Delta\rho}{2\pi}(\phi_m + 2\pi n) \tag{5.1}$$

$$\phi_m = m\Delta\phi \tag{5.2}$$

where ρ and ϕ are standard polar coordinates. The integer constants n and m represent the number of spiral rings and the number of the points on each spiral ring, respectively. Similarly, the linear spiral for the bipolar coordinate system involves a coupling of the radial coordinate ρ and bipolar azimuth coordinate α, where α is defined by $\alpha = \phi - \frac{\beta}{2}$ where β is the arm angle of the bipolar scanner. The linear spiral equations in this case are almost identical to equations 1 and 2; the only difference being the parameter ϕ is replaced by α. The sampling space parameters $\Delta\phi$, $\Delta\alpha$, and $\Delta\rho$ are calculated by following requirements for the

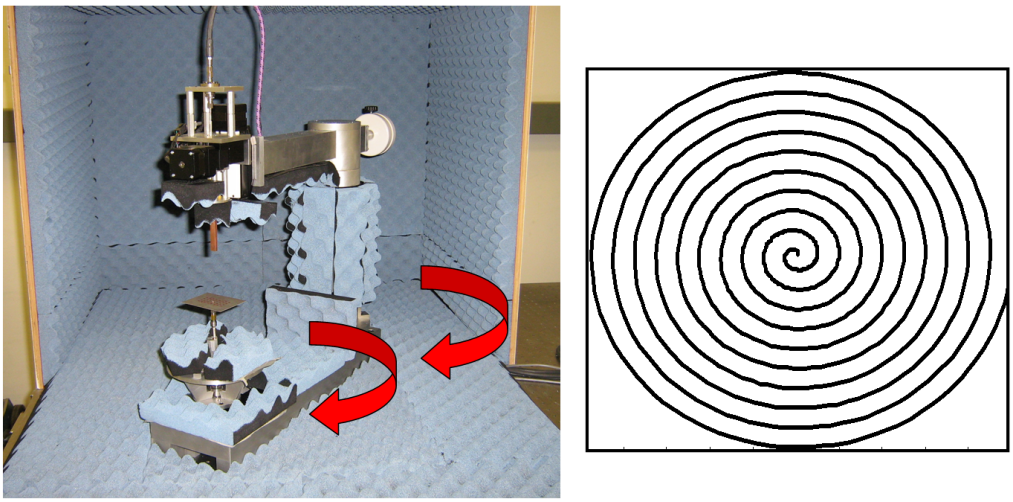

Figure 5.6: Spiral scanning for the bipolar scanner.

bipolar configuration outlined in [15]. Fig. 5.8 diagrams the linear spiral in both the plane-polar and bipolar coordinate system.

Discrete (stepped) implementation of this sampling geometry is straight-forward for both plane-polar and bipolar configurations. One simply has to indicate to the controller the position of the sampling point and measure after all axes arrive. There are no timing requirements beyond waiting for all axes to arrive before the measurement is taken. Continuous implementation, on the other hand, is straight-forward for the plane-polar configuration while complicated for the bipolar configuration. The plane-polar configuration only requires constant velocity for both the radial and azimuth axes to achieve the linear spiral geometry. When constant velocity is applied to the AUT and arm axes in the bipolar configuration, the geometric path does not follow a linear spiral, but rather a path we call a 'bipolar' spiral. Both spiral geometries begin at the same location, however, the subsequent path of the bipolar spiral begins to diverge from the path of the linear spiral. Fig. 5.9 shows the differences between the linear spiral patch with increment velocities (the velocity to traverse a distance $\Delta\rho$ or angle $\Delta\phi$ in a period of

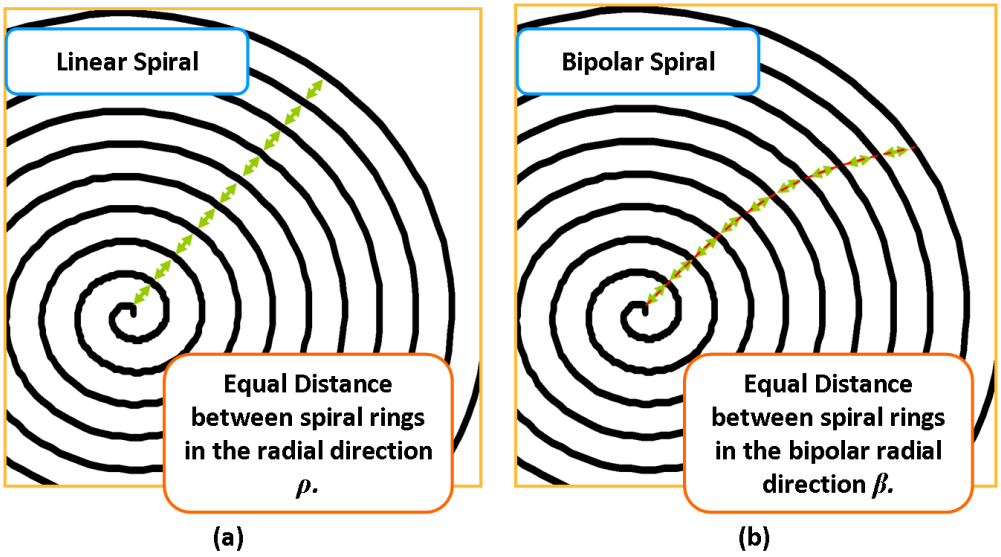

Figure 5.7: Spiral definitions: (a) Linear (b) Bipolar.

time) $\Delta\rho_v$ and $\Delta\phi_v$, and the bipolar spiral with incremental velocities $\Delta\alpha_v$ and $\Delta\beta_v$.

The difference between the two paths is due to the non-linear relationship between the distance coordinate ρ and the angular coordinate β and also the dependence of the angle ϕ on β. These relationships are defined as follows:

$$\beta = 2\sin^{-1}(\frac{\rho}{2L}) \tag{5.3}$$

$$\alpha = \phi - \frac{\beta}{2} \tag{5.4}$$

where L is the length of the bipolar arm. To match the spirals, one can use these relationships to parameterize the angles in time. In other words, using the constant incremental velocities $\Delta\rho_v$ and $\Delta\phi_v$ (that would create a linear spiral path in the plane-polar configuration) and analyzing one can determine the parameterized expressions for $\alpha(t)$ and $\beta(t)$.

These equations were found to be:

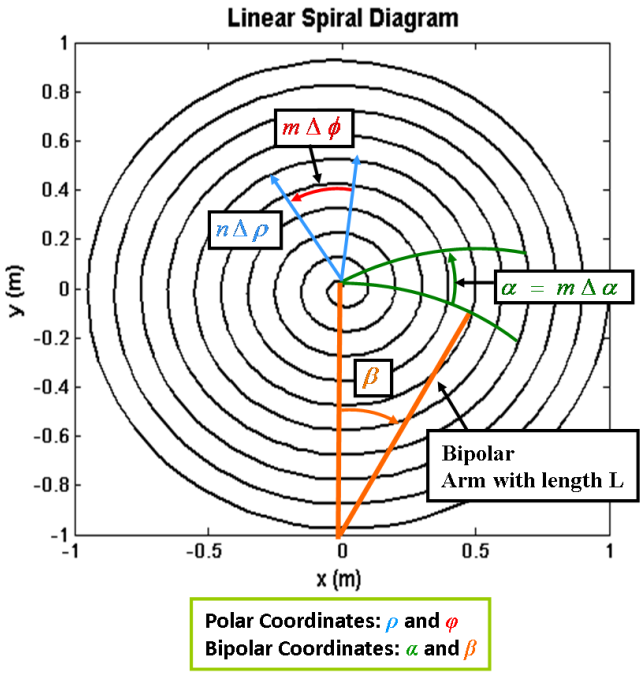

Figure 5.8: Linear Spiral diagram in plane-polar and bipolar coordinate systems.

$$\alpha(t) = t\Delta\phi_v + \sin^{-1}\left(\frac{(\Delta\rho_v/\tau)t}{2L}\right) \tag{5.5}$$

$$\beta(t) = 2\sin^{-1}\left(\frac{(\Delta\rho_v/\tau)t}{2L}\right) \tag{5.6}$$

where τ is the length of time to traverse one spiral ring azimuthally. These equations can then be directly used to govern the motion of the bipolar axes over the time of the measurement.

Implementation of a continuous linear spiral routine for the bipolar configuration requires non-uniform velocity and acceleration for either the arm, AUT axis, or both. In addition, if there is probe co-rotation (to preserve the antenna polarization during measurement), the velocity and acceleration of the probe axis must be considered. The probe axis, which is attached to the far-end of the arm over the AUT axis, has a position that is a combination of the angle α and β. Due to fact that we considered probe co-rotation and also to hardware restrictions, a simple

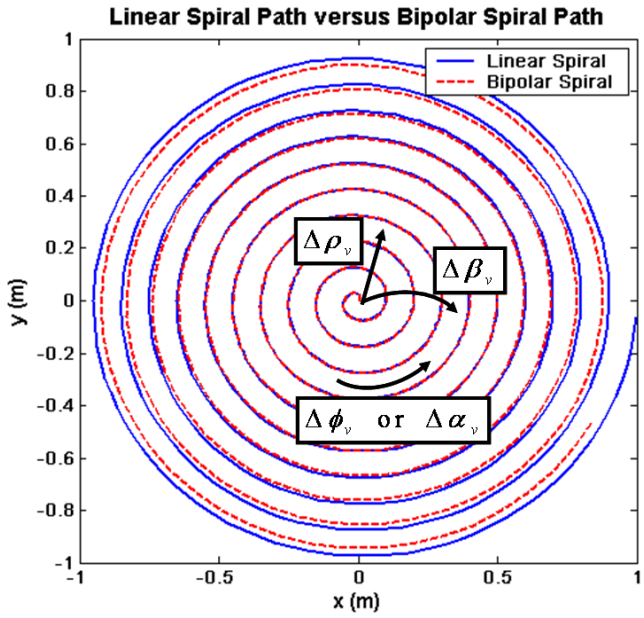

Figure 5.9: Diagram showing how the linear spiral and bipolar spiral diverges.

application of a non-uniform acceleration and velocity equations above could not be directly entered into the motion controller in our implementation. Instead, an approach had to be devised to allow continuous updates of the acceleration and velocity of each axis during the measurement to effectively match the linear spiral path.

This approach took advantage of the discrete nature of antenna measurement. During the measurement, the only times when all the axes (AUT, arm, and probe) must be in the correct position is at the pre-calculated measurement points governed by the linear spiral equations. In between these measurement points, the three axes can be in any position and rotate at any velocity or acceleration. Thus, after determining the constant period time between each adjacent point, the acceleration and velocity of each axes could be determined directly from the knowledge of the starting and ending points of each adjacent point pair. These calculations can be done either before the measurement starts or during the measurement, however, the correct values for the acceleration and velocity must be passed to

the controller during the measurement to allow correct motion. Either way, the measurement will measure the data points of a linear spiral path over the measurement plane in a continuous fashion as long as the controller data is fed to the controller without interruption.

Separately, the RF measurement apparatus (in our case an Agilent PNA), should measure power at the corresponding data points. The measurement can be triggered in one of two modes. The first can take measurements at the time-interval between points. As long as there are no errors in motion, the controller should position each axis to in the right configuration at the time these measurements are taken. The second mode can rely on the position reporting of the motion controller. During the measurement, the motion controller can be pinged for the position of each axis. With knowledge of the position of each axis for a particular data point, the trigger can be set so that a measurement is taken when the axes reach or nearly reach the correct position.

If one is taking averaged power measurements, either triggering mode can programmed to trigger before the actual time or position, respectively for mode 1 and 2, is completely reached since an average measurement cannot complete multiple measurements in one position without stopping. The amount of time or how far before each power measurement is at the discretion of the programmer.

A straight-forward flowchart is presented in Fig. 5.10 outlining the implementation of the linear spiral.

5.2.2 Continuous Bipolar Spiral Scanning

Bipolar spiral scanning involves uniform velocity for both the arm and AUT rotational axes. This bipolar spiral geometry differs from the linear spiral due to the fact that it exhibits uniform spacing between subsequent radial rings along the bipolar azimuthal angle as shown in Fig. 5.7(b). This bipolar geometry and its

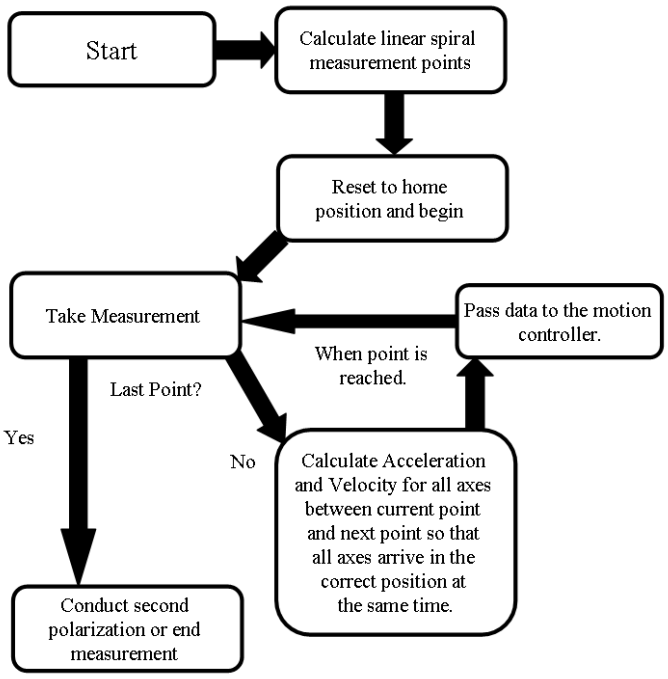

Figure 5.10: Flow-chart showing the continuous spiral algorithm for the bipolar scanner.

simple implementation avoids the inherent issues with linear spiral geometry with the bipolar scanner and is the preferable mode for measurement for all possible scanning geometries using the bipolar scanning technique.

The bipolar spiral is characterized by the following equations:

$$\beta_{nm} = \Delta\beta(n + \frac{m}{M}) \tag{5.7}$$

$$\alpha_m = m\Delta\alpha \tag{5.8}$$

where β and α are the bipolar coordinates defined by the bipolar configuration, the integer constants n and m represent the current particular spiral ring and the current particular point on each spiral ring, respectively. The parameter M is the number of total points per spiral ring. Both equations feature sampling spaces $\Delta\alpha$ and $\Delta\beta$ that are determined by sampling requirements outlined in [15].

Implementation of the bipolar spiral is simple. Uniform and continuous motion is required to create this geometry and is available for most motion controllers and drivers. The only requirement during the motion is that the velocity of the arm travels only an angle of $\Delta\beta$ in one revolution of the AUT axis.

5.2.3 Spiral Measurement Comparisons

To demonstrate and verify the spiral implementations described, a sequence of comparative measurements were conducted with a millimeter-wave antenna measurement system. Three measurements were conducted overall, each using a different measurement scheme: Stepped standard bipolar, linear spiral, and bipolar spiral. The standard bipolar measurement is the typical scheme used in bipolar measurement. Each measurement scheme was tested for measurement accuracy and total measurement time.

The antenna used in these measurements was a custom designed 4x8 Ka-band rectangular patch planar array [26] shown in Fig. 5.11. The antenna was operated at 31.2GHz.

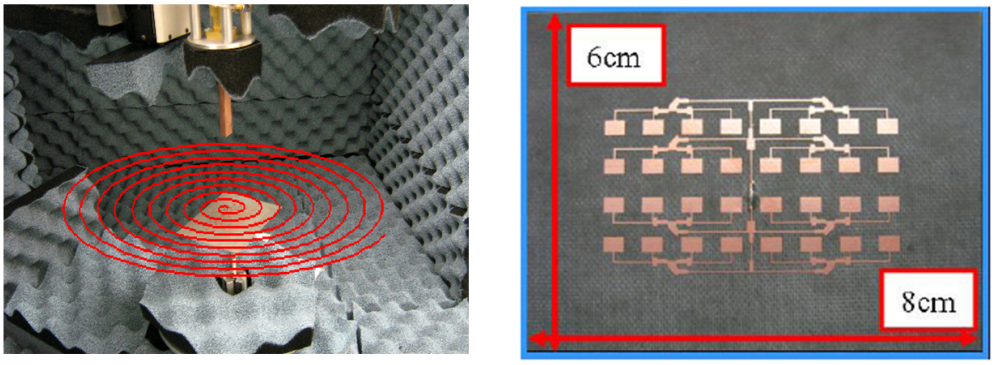

Figure 5.11: 4x8 Microstrip Antenna Array used in the spiral measurement comparisons.

The results of the measurements are shown in Fig. 5.12. Fig. 5.12(a), 5.12(b), and 5.12(c) show the measured co-polarized near-field images for the three scan-

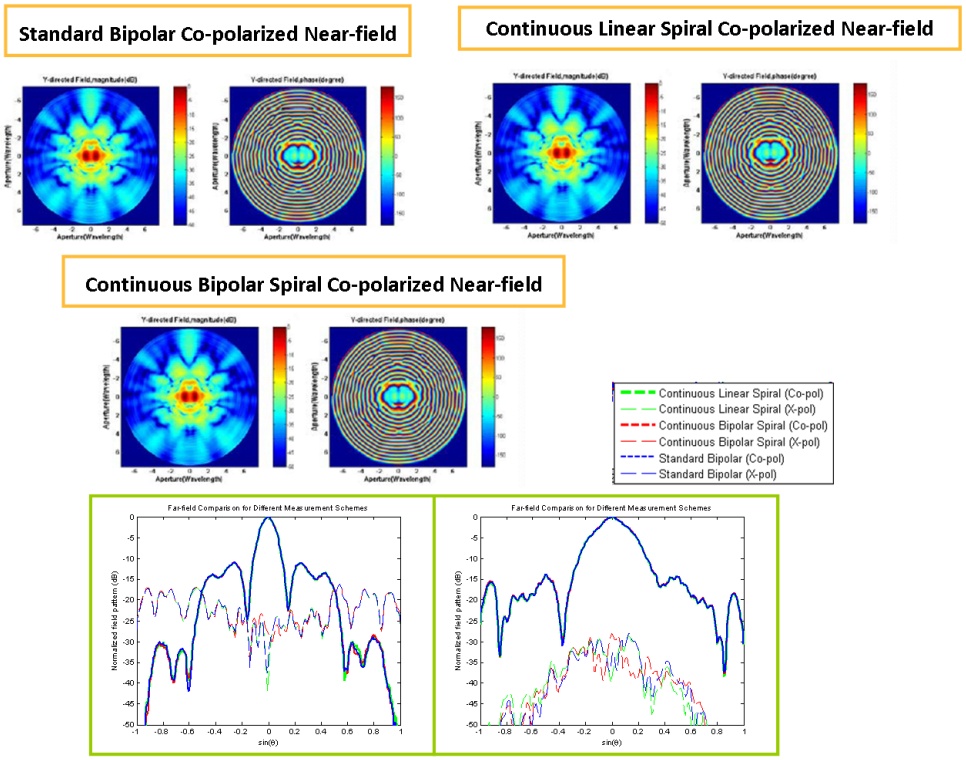

Figure 5.12: Near-field image and far-field pattern comparisons between the standard stepped bipolar, linear spiral, and bipolar spiral measurements. (a) Near-field of standard stepped bipolar measurement. (b) Near-field of linear spiral measurement. (c) Near-field of bipolar spiral measurement. (d) H-plane Co-polarized far-field comparison. (e) E-plane Co-polarized far-field comparison.

ning geometries. This data was then processed to the far-field for comparison. Figure 5.11(d) and 5.11(e) shows the co-polarized H and E planes of the array for each of the scanning geometries superimposed on one another. It is clear that the patterns are virtually identical, verifying the viability of all the scanning geometries.

The measurement times of the linear spiral and bipolar spiral measurements were very close to one another, however, showed a 2.5 times decrease in time in comparison to the stepped standard measurement. It should be mentioned that

the total measurement time is also depended on the programmed speed of the AUT axis.

5.3 Phaseless Measurements at Millimeter-wave Frequencies

One important goal of the bipolar measurement research was to implement and demonstrate phaseless measurements at millimeter-waves. The phaseless measurement, where only amplitude measurements are taken, was developed for the bi-polar scanner in [19]. It shows that with two planes of amplitude data above the antenna aperture if was possible to retrieve the unknown phase by an iterative Fourier algorithm starting from a standard initial guess. Furthermore, it is shown in [20], that the technique can be improved by using an evolutionary algorithm to determine a more appropriate initial guess.

Phaseless measurements have a number of important advantages that make it very useful for millimeter-wave antenna measurement. The first is the mitigation of positional errors. Small positional errors due to positioner over-shoot, rounding errors, etc., can effect the phase measurement significantly at millimeter-wave frequencies while the amplitude is not as sensitive [29]. With phaseless measurements, the phase errors are not incorporated in the data and can help avoid these types of measurement error. The second advantage is the elimination of vector RF test equipment. The vector network analyzer used for the full amplitude and phase measurements, which has the ability to measure amplitude and phase up to 67GHz, is the most expensive piece of the measurement system. In fact, it is about 5 times the total cost of the rest of the system. Such an expense is forbidden for most laboratories. Phaseless measurements, in contrast, only requires a signal and power (amplitude) measurements. A simple oscillator or frequency synthesizer and a power meter and sensor can be used, reducing the costs for

appropriate equipment considerably.

To demonstrate phaseless measurements, the Ka-band array was measured according to the requirements of the phase retrieval algorithm. Four sets (X- and Y- polarized near-fields at two different measurement planes) of doubly-sampled data was collected at measurement planes 5cm (6λ) and 7.3cm (8.8λ) above the antenna under test. Phase retrieval was used to then recover the phase and then propagate to the far-field.

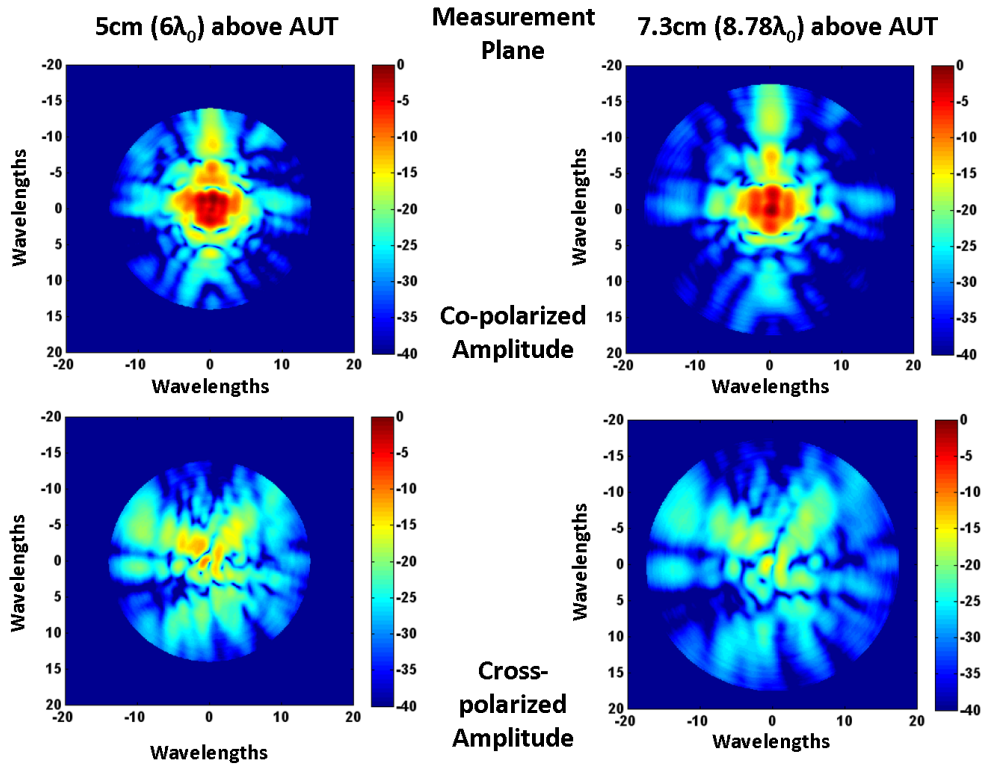

Figure 5.13: Doubly-sampled amplitude measured near-field for the two measurement planes (5cm and 7.3cm) of the phaseless measurement.

Fig. 5.13 shows the measured doubly-sampled amplitude at the two measurement planes. The recovered (after applying phase retrieval) amplitude and phase at the first measurement plane is shown in Fig. 5.14. Visually, the measured and recovered amplitude images look very similar. Fig. 5.15 compares three E-plane

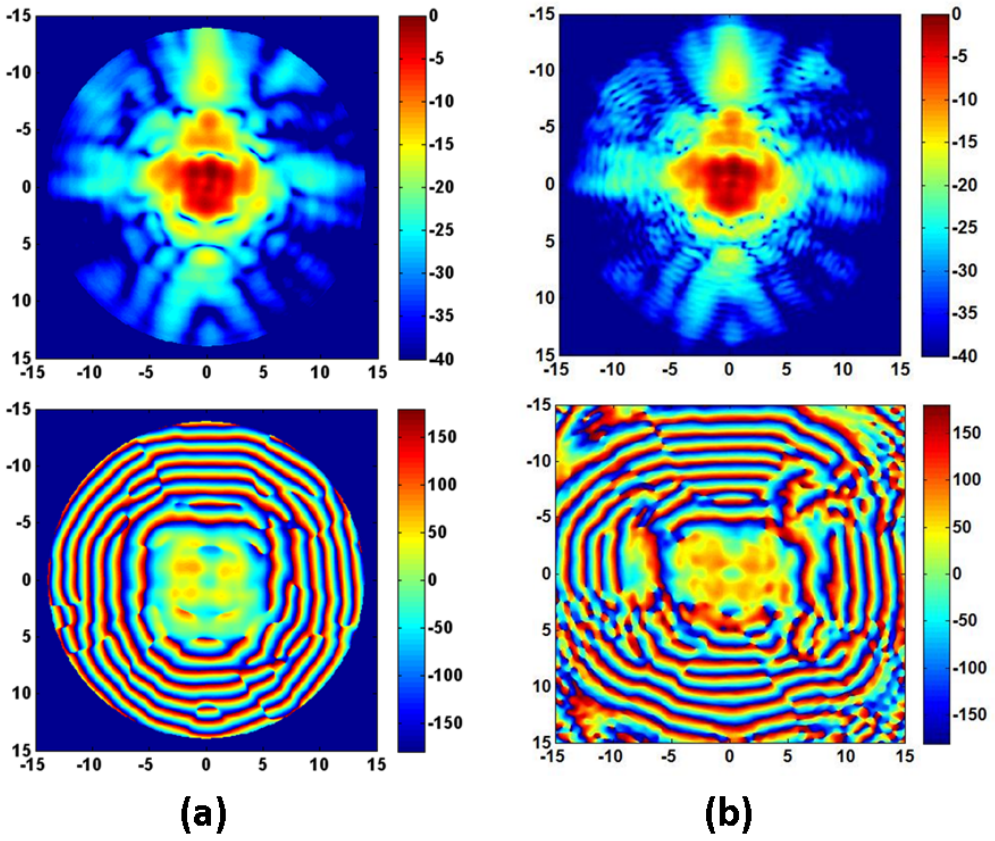

Figure 5.14: Comparison of the conventional and the recovered amplitude and phase co-polarized near-field.

and H-plane far-field patterns: The conventional measurement, a simulation of the array antenna (conducted in HFSS), and the phaseless measurement. The phaseless measurement far-field agrees somewhat with the conventional and simulation, however, there is enough difference to suggest that the phase retrieval algorithm is not converging to the most accurate result. It was determined that the difference was significant enough that a deeper investigation was required.

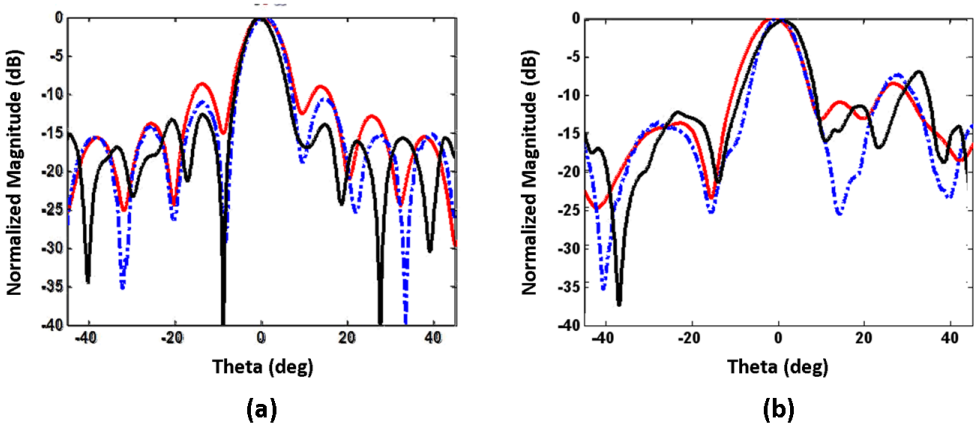

Figure 5.15: Comparison of the far-field primary cuts of the conventional measurement, simulated array, and phaseless measurement.

5.4 Antennas with an Internal Source: A Phaseless Measurement Technique

Modern wireless devices are increasingly becoming completely integrated, where all components from the source to the antenna are included in the overall design. From a design and manufacturing standpoint this is quite advantageous, however, from a testing and measurement standpoint, verifying performance can be complicated, especially when characterizing the antenna.

In most antenna measurements, a signal is directly fed to the antenna where its radiation is measured using a probe at a certain distance from the antenna. This signal is usually referenced using a network analyzer or similar receiver system. In far-field measurements, this referenced signal is used to determine gain and antenna efficiency; however, it is not required to measure the radiation pattern. In near-field measurements, this referenced signal is required because both amplitude and phase must be measured to calculate the far-field radiation pattern.

For wireless integrated devices, the antenna is fed by its own internal source. To measure the antenna using conventional methods, the input signal must have

some way to be referenced. Unless the device designer specifically adds a way to do so, this is usually not possible. For existing antenna measurement chambers and ranges, this may complicate the measurement configuration, especially for near-field ranges where chamber modification may not be possible. Thus, for measurements of an antenna with an internal source, one cannot use the existing vector network analyzer in the conventional way. Instead, the input signal, coming from port 1 of the network analyzer cannot be applied to the antenna and instead is terminated. This configuration, shown in Fig. 5.16, uses the vector network analyzer as a receiver, measuring both amplitude and phase of the antenna using the reference signal from port 1. In this configuration, the measured amplitude and phase value is the relative value in relation to the integrated devices source. In theory, this is still valid for near-field measurement because relative field values are required to calculate the far-field. In reality, however, the lack of synchronicity between the network analyzers source and the devices internal source causes stability issues (drift) with the measured phase. This renders the measured phase unusable for the near-field to far-field transformation. In contrast, the relative amplitude can be used as long as the internal source power is stable. This allows for the use of phaseless techniques (i.e. phase retrieval) to determine the near-field phase that is required for the near-field to far-field transformation.

To demonstrate the issue with the measured phase that is presented in Fig. 5.16, a representative measurement of the millimeter-wave 8x8 microstrip array shown in Fig. 4.1 was conducted. Two measurements were conducted: The first was a measurement using the conventional near-field measurement configuration. The second was a measurement using a configuration that mimicked that of Fig. 5.16. To do this, a separate frequency synthesizer was connected to the input of the antenna array. This configuration is shown in Fig. 5.17.

Near-field results from the two measurements are shown in Fig. 5.18. Clearly, the amplitude images between the two measurements are very similar. However,

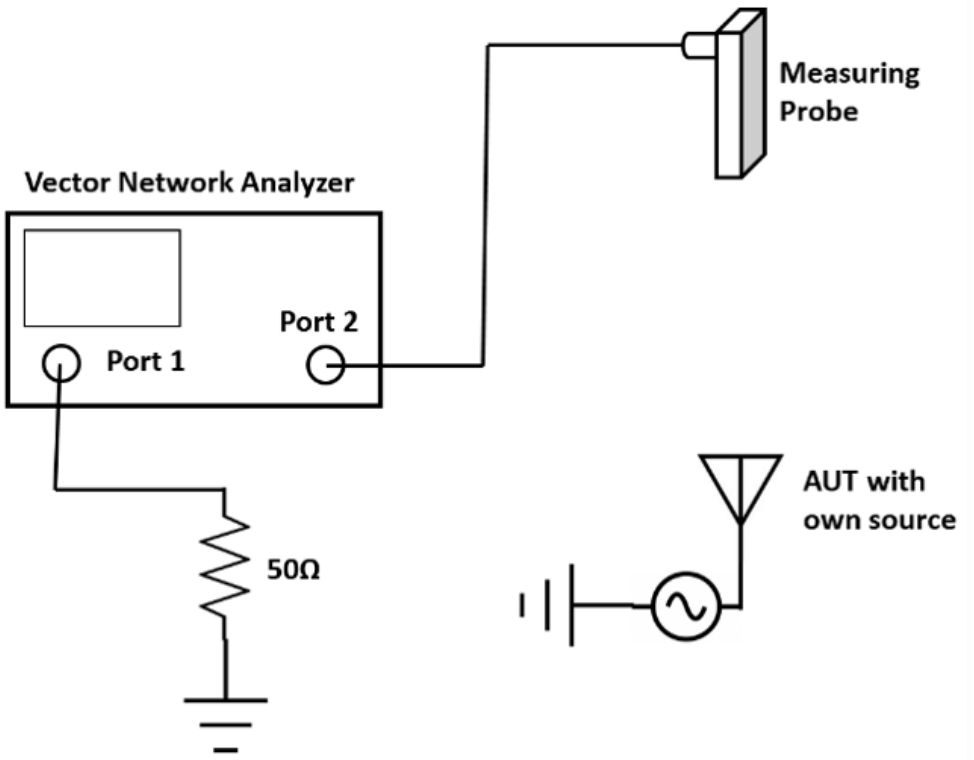

Figure 5.16: Near-field measurement configuration for antennas with an internal source.

the measured phase is completely different. Any attempt to conduct the near-field to far-field transformation would certainly result in different results. This is shown in Fig. 5.19 where the internal source measurement far-field pattern does not at all agree with the conventional measurement far-field (the accurate radiation pattern).

With only the amplitude information valid in an internal source measurement, one must rely on phase retrieval to accurately obtain the radiation pattern. To show this, two measurements of the 8x8 millimeter-wave microstrip array were conducted. The first measurement was a phaseless measurement using the conventional configuration. The second was a phaseless measurement using the internal source configuration. The near-field data collected was then used in the phase retrieval process to produce the far-field patterns. Measurements were conducted using UCLAs Millimeter-wave Bipolar Planar Near-field Antenna Measurement System. Fig. 5.20 shows the near-field images of the conventional configuration and internal source measurement after the phase retrieval algorithm was applied. Both show excellent agreement between one another. Fig. 5.21 shows the comparison between the far-field radiation patterns of the two measurements. Excellent agreement is seen between the two patterns. It also presents a table showing the excellent agreement of the directivity and beamwidth of the radiation pattern.

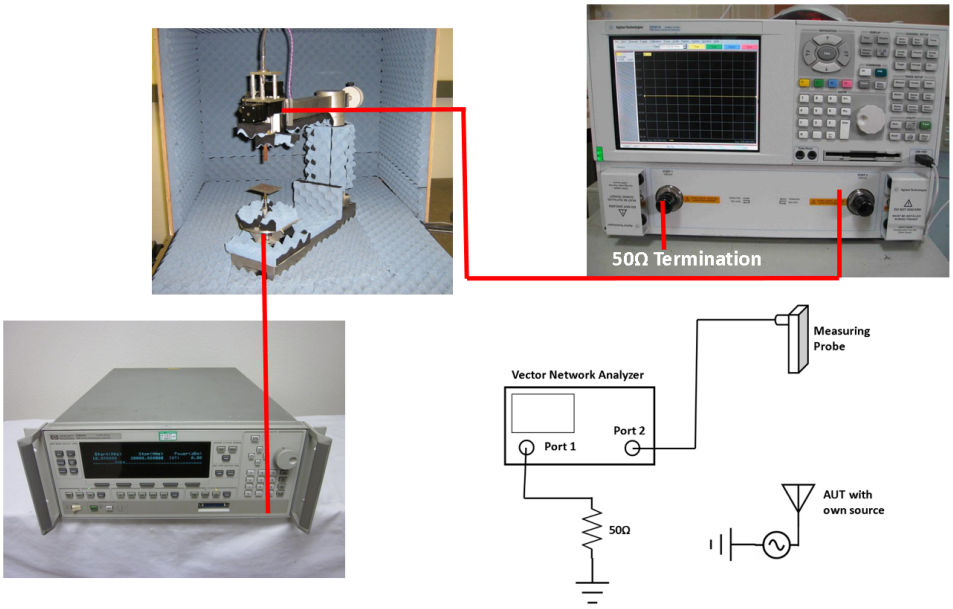

Figure 5.17: Near-field measurement configuration for internal source measurements for non-integrated antennas.

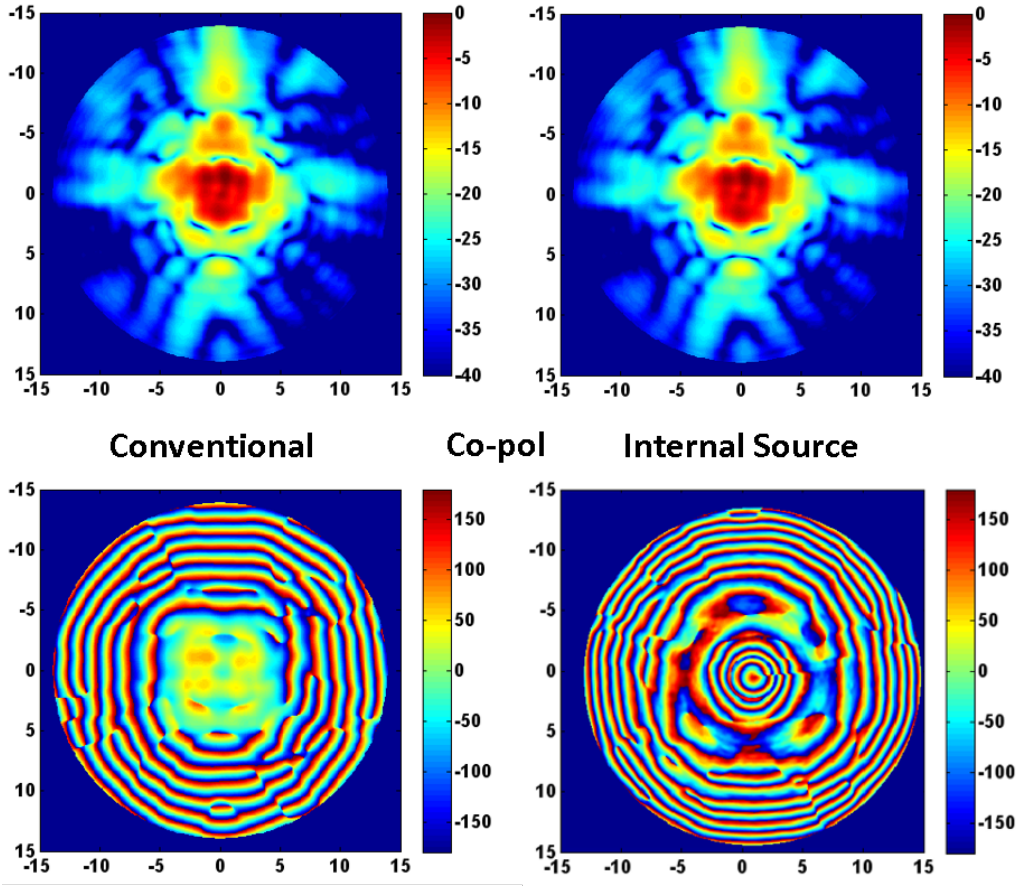

Figure 5.18: Comparison of the conventional and internal source measurements co-pol near-field images. These images demonstrate the phase problem when dealing with antennas with internal sources. On the other hand, the amplitude between the two measurement configurations are very similar and can be used to determine the radiation pattern.

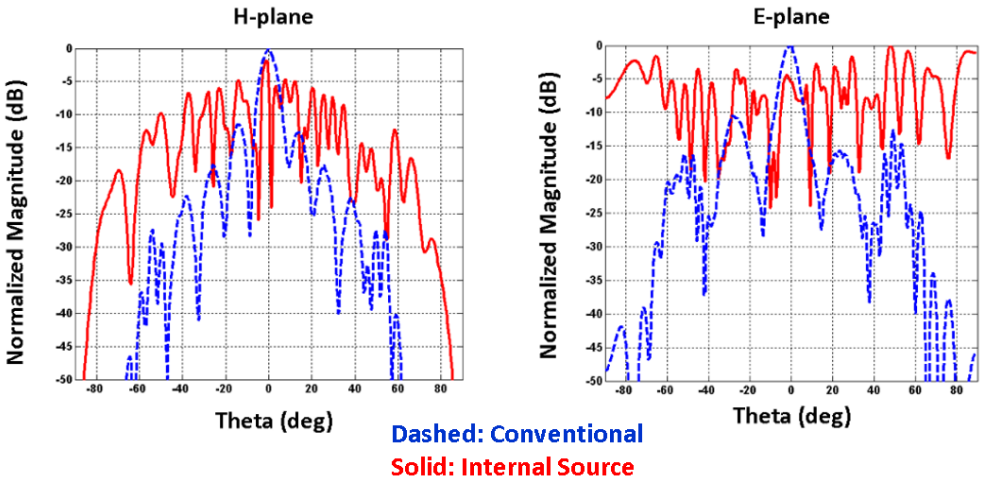

Figure 5.19: Comparison of the conventional and internal source measurements co-pol far-field radiation patterns. Due to the erroneous near-field phase, the internal source measurement cannot resolve an accurate far-field radiation pattern.

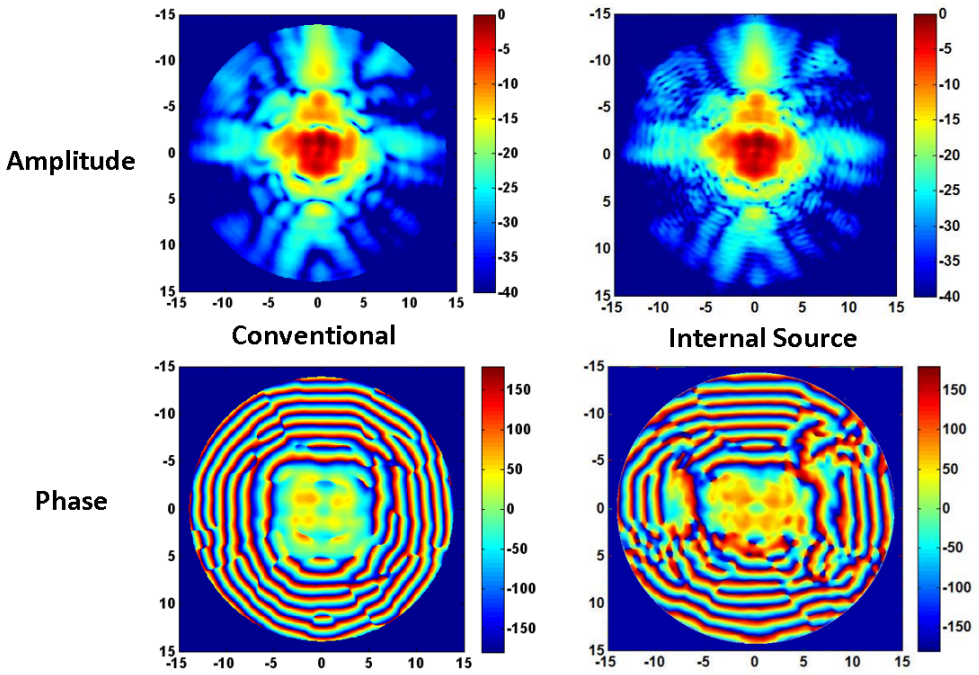

Figure 5.20: Comparison of the conventional and internal source phaseless measurements co-pol near-field images after applying the phase retrieval algorithm. These images show the excellent agreement between the near-field of the two configurations when considering amplitude-only data.

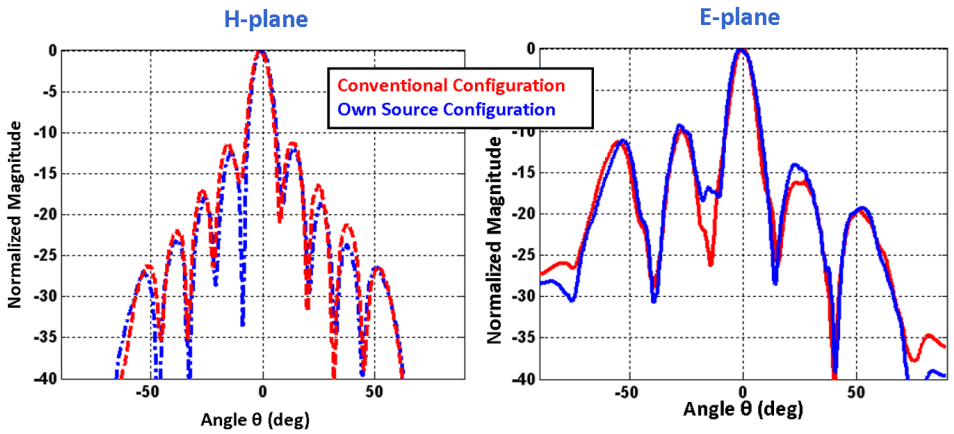

Antenna Parameters	Directivity	BeamwidthH-plane	Beamwidth E-plane
Conventional	25.53	6.87	7.07
Internal Source	25.32	6.85	7.17

Figure 5.21: Comparison of the conventional and internal source phaseless measurements co-pol near-field images after applying the phase retrieval algorithm. These images show the excellent agreement between the near-field of the two configurations when considering amplitude-only data.

CHAPTER 6

Three-dimensional Periodic Structures for Solar Harvesting and Electromagnetic Absorption Applications

Widespread adoption of solar energy has been limited due to practical issues such as low conversion efficiency and high cost. Although research has been conducted in addressing these issues [30,31], the technology has not progressed far enough to make solar energy a popular alternative for energy production. With solar energy being readily available and abundant, the ever-increasing demands for renewable energy have made new concepts in solar energy collection a paramount task for researchers.

6.1 Nanostructure Photovoltaic Arrays for Solar Energy Harvesting

Recently, nanostructured photovoltaic solar cells have been introduced as alternatives to conventional bulk photovoltaics because of their inherent advantages in optical absorption, conversion, and carrier extraction. It has been suggested that they possess the potential to exceed efficiencies of conventional (flat or thin-film) solar cells [30–35]. Investigations into nanostructures encompass many types of photovoltaics including hybrid cells [36], nanopillars [37], nanocones and nanoprisms arrays [38], multi-junctioned cells [39], and unpatterned nanostruc-

tured cells [40]. New lithographic-controlled fabrication techniques allow for patterned and periodic structures such as nanopillars to span the cell, making it possible to control the pillar dimensions and configuration for optimum design. These periodic nanopillars feature inherent properties that aid solar energy collection, such as: (i) Increased optical absorption properties that reduces inherent reflection from the solar cell. (ii) Increased surface area without an increase in the overall footprint of the solar cell. This allows for a larger area for carrier extraction to occur. (iii) Nanostructures allows for favorable optical thickness, improving carrier generation and minimizing diffusion lengths and carrier recombination. In addition, a preliminary investigation by the authors in a brief conference paper [37] has shown the potential for nanostructured solar cells to have favorable broadband and angle-independent performance that may eliminate the need for antireflection coatings and/or mechanical tracking used in many commercial solar cell installations.

This section will present a comprehensive investigation into the electromagnetic performance of these nanostructured solar cell arrays and their implications in the overall improvement of solar cell technology by primarily using full-wave analysis. It will focus on GaAs nanopillar arrays, which are patterned arrays of nano-sized columns made of doped GaAs material [36]. SEM images of these types of core-shell GaAs nanopillar arrays are shown in Fig. 6.1(a) [36]. The typical structure of a single core-shell nanopillar is shown in Fig. 6.1(b). It is comprised of two layers: The inside layer is -type GaAs material (doped with silicon), with the top layer being -type GaAs material (doped with zinc). The substrate is -type GaAs material and there is a dielectric oxide layer that spans the top of the substrate. The -type layer is designed with a nominal thickness to optimize carrier generation and minimize the distance a carrier must travel before extraction. In the following analyses, the typical nanopillar structure and dimensions are used; however, throughout the paper many parts of the structure

are modified from GaAs material to PEC material to better understand how the structure interacts with the incident optical field. These modifications will be discussed more in the Section V. GaAs has been chosen for these structures because of their advantage in optical performance over other semiconductors such as silicon. Firstly, the bandgap of GaAs is best suited to absorb the visible region of the solar spectrum, the most energetic region of the spectrum. Secondly, GaAs has a direct bandgap, reducing the total thickness required for effective absorption. In real solar cell devices, a layer of transparent conductor such as indium-tin oxide (ITO) is placed over the nanopillar array to act as an electrode, but is not considered in the analysis here since this paper is more focused on understanding the fundamental operation of nanopillar arrays and not the performance of a single design.

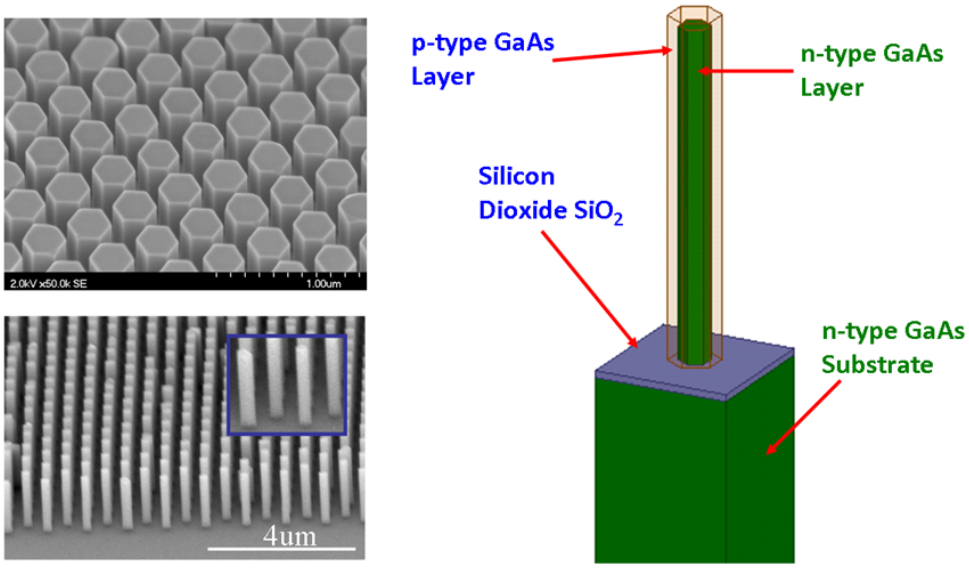

Figure 6.1: (a) Scanning electron microscope images of GaAs nanopillar arrays (courtesy of UCLA Integrated Materials Lab). (b) Basic configuration of an individual nanopillar.

The section will investigate the following: (a) Incorporation and verification of material optical properties, (b) Nanopillar array optical absorption versus con-

ventional solar cell optical absorption, (c) Parametric investigations of nanopillar dimensions and configuration for optical absorption properties, (d) The application of electromagnetic theory and concepts for improving nanopillar arrays, and (e) Understanding of the role of the structure and materials of the nanopillar arrays through graphical visualization of the electric fields.

6.1.1 Analyzing Optical Absorption

In general, the overall power conversion efficiency of a solar cell, denoted by η_{Overall}, can be separated into three major efficiency components as shown below:

$$\eta_{\text{overall}} = \eta_{\alpha}\eta_{\text{g}}\eta_{\text{ex}} \tag{6.1}$$

where η_{α} is the fraction of power absorbed by the cell (absorption efficiency), η_{g} is the efficiency of carrier generation, and η_{ex} is the efficiency of carrier extraction from the cell device into the cell electrodes over the entire solar spectrum. Fig. 6.2 illustrates each of these efficiency components in a nanostructure photovoltaic array that consists of either nanopillars, nanocones, or nanoprisms. The absorption efficiency is defined as follows:

$$\eta_{\alpha} = 1 - |\Gamma(\omega)| - |\tau(\omega)| \tag{6.2}$$

where $|\Gamma(\omega)|$ is the frequency, incident angle, and polarization dependent reflection coefficient and $|\tau(\omega)|$ is the frequency, angle, and polarization dependent transmission. The carrier generation efficiency, η_{g}, is defined as the ratio of the number of electron-hole pairs generated over the number of above-bandgap incident photons, and the carrier extraction efficiency, η_{ex}, is defined by the ratio of the number of electrons extracted by the cell's electrodes over the number of electron-hole pairs generated. Clearly, maximizing the overall solar cell efficiency is a multidisciplinary effort involving material science, semiconductor physics, and

electromagnetic analysis.

The broad range of research and resources that is required to come to an optimal overall nanostructure array design is certainly daunting. In-depth understanding of each process and how they interact (and perhaps conflict) with each other is essential but elusive without expertise in the appropriate disciplines. An approach to simplify the task, or at least to provide a launching point, could be to separate the processes into independent components. Each component would be evaluated and optimized independently without restriction (due to consideration of the other components) where, later on, the optimal component designs would be merged into an overall optimized design. With this approach in mind, the authors hope to contribute only to the first efficiency component: Optical absorption (absorption efficiency). Working under the assumption that maximizing optical absorption will lead to better overall efficiency (by providing more photons to create electron-hole pairs); the authors will seek to analyze and understand how the structure and configuration of the nanopillar array affect and improve optical absorption. Eventually, it is hoped that this analysis can potentially be a valuable basis for further optimization of these devices

Current investigations into optical absorption of nanostructures are often secondary goals in nanopillar array research where the primary goal is to understand fabrication processes and conditions [34], [36]. These investigations often use cumbersome trial-and-error approaches that require expensive and time-consuming fabrication and measurement iterations. For more cost-effective progress in both characterizing and maximizing optical absorption in nanostructures, it was necessary to verify an accurate simulation platform for characterization that can eliminate these costly iterations. Furthermore, a simulation platform can reveal the fundamental operation of these nanostructures, leading to an enhanced physical understanding of the processes that drive optical absorption in nanostructures.

Full-wave simulation has been an essential tool in characterizing and opti-

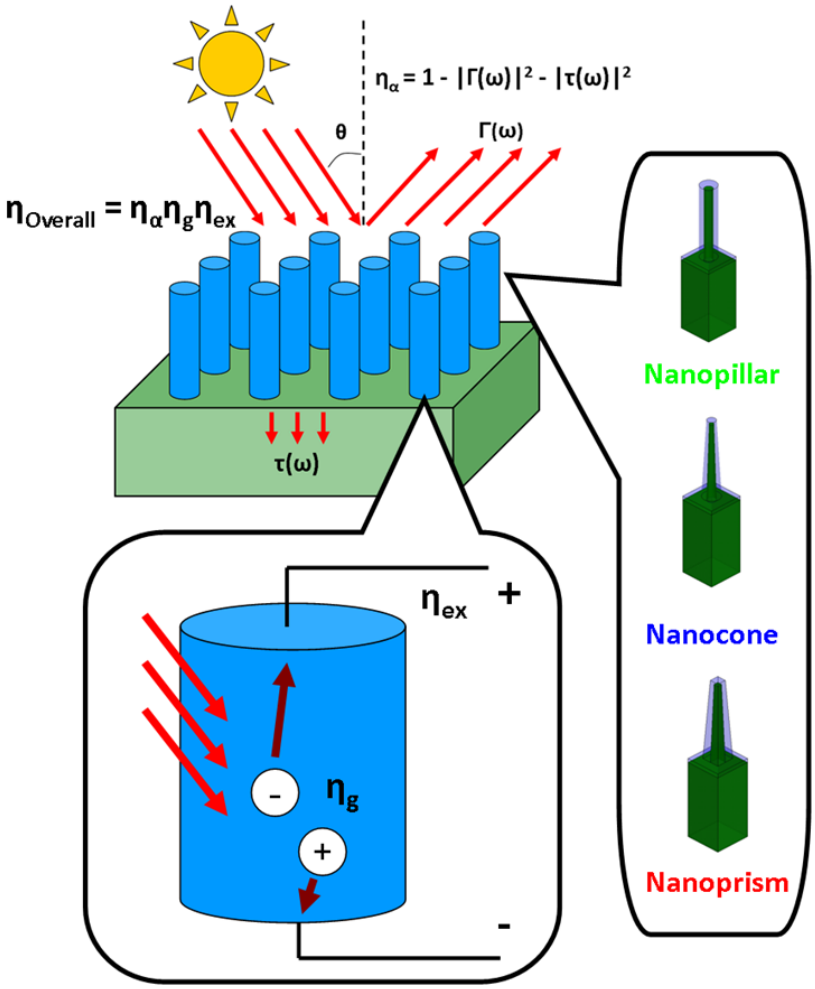

Figure 6.2: Illustration of the major processes of a nanostructure solar cell and some examples of nanostructures. Each process can be represented by an efficiency term that contributes to the overall solar cell efficiency.

mizing periodic electromagnetic structures at RF and microwave frequencies. At optical frequencies, some research using full-wave simulations has been done on optical metamaterials and split-ring resonators [41], [42] and other types of optical structures and devices [43], however, such tools have not been as common because of the usually large problem size of most optical structures. With the advent of sub-wavelength nanostructures, however, the problem size is small enough to make computation in the optical regime possible, making it the most accurate

tool to characterize and optimize nanostructured solar cells for maximum optical absorption.

6.1.2 Material Considerations

Semiconductor material is subject to frequency dependent material properties over the solar spectrum. Since the size of a typical nanopillar (¿50nm in thickness, width, and height), quantum effects such as confinement or plasmonic properties are avoided [4, 44]. Instead, widely available bulk material properties can be used in the analysis of the nanopillar arrays. For the nanopillars used in this study, n-type Si-doped GaAs, p-type Zinc-doped GaAs, and SiO2 material properties over the visible region were found in [45–47]. The parameters required for electromagnetic analysis include the index of refraction, n, and the extinction coefficient, k. From these parameters the frequency dependent relative dielectric constant and loss tangent can be obtained and incorporated into the full-wave analysis. These are plotted in Fig. 6.3 showing the dielectric properties for both n-type and p-type GaAs.

Verification of the constitutive parameters used in the analysis was achieved by comparing the reflection magnitude of a bulk GaAs substrate calculated in a full-wave simulator and a representative measurement of a real bulk GaAs substrate. The reflection magnitude was used instead of absorptance because the reflection magnitude can be measured directly. An equivalent simulation was conducted in the full-wave simulator, in this case High Frequency Structure Simulator (HFSS), using imported material properties where the sample was illuminated with near normal incidence. The measurement was taken with a UV/Visible spectrophotometer and was measured over the visible spectrum of 450 THz to 750 THz. Fig. 6.4 shows the comparison of the sample's measurement and simulation. Excellent agreement is seen between the measured and simulated reflection magnitude, validating the use of the material properties in the simulation model.

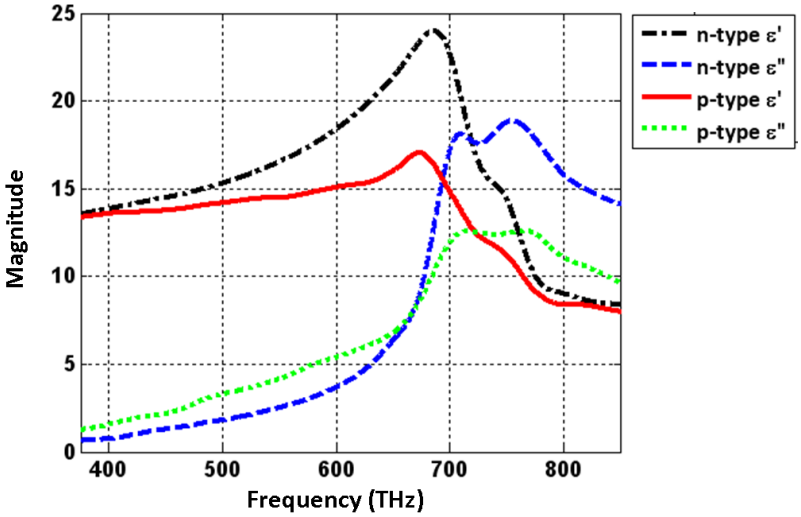

Figure 6.3: The real and imaginary part of the dielectric constant for N-type and P-type GaAs used in the electromagnetic analysis. These values were calculated from the index of refraction and extinction coefficient from [13][15]: $\epsilon^{'} = n^2 + k^2$, $\epsilon^{"} = 2nk$.

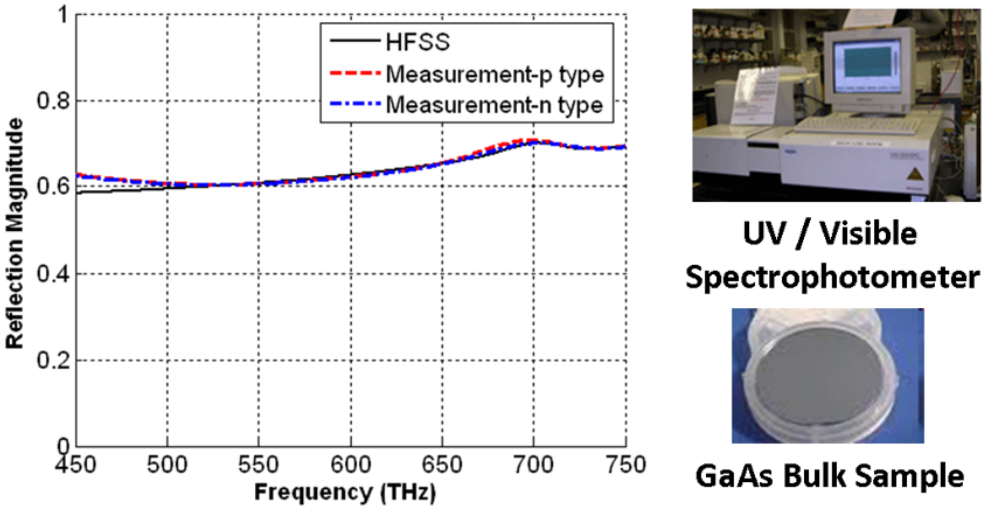

Figure 6.4: Comparison between bulk GaAs measurement and the equivalent simulation in HFSS. Images of the spectrophotometer and an example of the GaAs bulk sample that was measured.

Optical properties can be found for many different types of bulk semiconductor, metals, and dielectric materials where they can be collected and imported into the simulator. If samples are available, they can also be verified in the UV/Visible spectrophotometer as well. For newer materials, spectrophotometer measurements can be used to extract optical properties for use in the simulator. These material properties can be used when investigating new nanostructures or array configurations.

It was also desired to measure the reflection coefficient of a sample nanopillar array over the visible range. Unfortunately, current fabrication techniques available to the authors do not allow for samples large enough to be measured accurately using UV/Visible spectrophotometer. However, since this paper is focused more on the implications of nanopillar structure and configuration, absolute values of optical absorption were not required to understand relative differences in absorption properties between different designs. As more fabrication capabilities become available to the authors, comparisons between real samples and simulated results will be a priority and work is underway in that direction.

6.1.3 Conventional Versus Nanostructure Solar Cells

Any solar cell (flat or nanostructure) requires that maximum optical absorption occur in the active region. Electromagnetic phenomenon, in consequence, plays a large role in designing an efficient nanostructure solar cell. Conventional bulk photovoltaic solar cells are usually pn-junctions comprised of semiconductor material usually configured in thin, flat samples. This configuration exhibits certain disadvantages that limit its optical absorption efficiency. For gallium arsenide (GaAs), a flat cell with no anti-reflection coating that is illuminated with unpolarized sunlight has an absorptance of less than 65%. The absorptance of unpolarized light is defined by:

$$|\Gamma_{\text{Unpolarized}}| = \frac{1}{2}(|\Gamma_{\text{TE}}|^2 + |\Gamma_{\text{TM}}\ |^2) \tag{6.3}$$

where Γ_{TE} and Γ_{TM} are the reflection coefficient of the TE and TM polarized incident waves. In the analysis of the flat cell, transmission is not considered because the substrate is sufficiently thick enough to allow complete absorption (it is several hundred skin depths deep).

Nanostructure arrays specifically have an advantage over conventional flat cells due to the fact that reflection can be reduced inherently for a wide angle of incidence without the need for lossy anti-reflection coatings or cumbersome mechanical tracking solutions. Fig. 6.5 shows a comparison between the absorptance of a conventional GaAs bulk solar cell and a representative nanopillar array for unpolarized light over the visible spectrum. The dimensions of each individual nanopillar of the array are included in the figure. It shows, even without any optimization, the inherent absorption of the nanopillar array is over 1.5 times that of the conventional flat cell. These advantageous properties make nanostructures an interesting device for further development and have the potential of improving overall solar cell efficiency over conventional bulk cells in the near future.

The full-wave analyses conducted here were done in the High Frequency Structure Simulator (HFSS). The nanopillar array was represented using a unit cell (shown in Fig. 6.1(b)) of a single nanopillar with periodic boundary conditions. The periodic boundary conditions enforces the electric and magnetic fields to be continuous (with a phase shift) on each side of the unit cell, essentially representing the structure as an infinite array of identical nanopillars. To represent the array as an infinite structure is valid in this case because of the large amount of pillars in a single sample (more than 250,000 pillars per 0.5mm by 0.5mm sample).

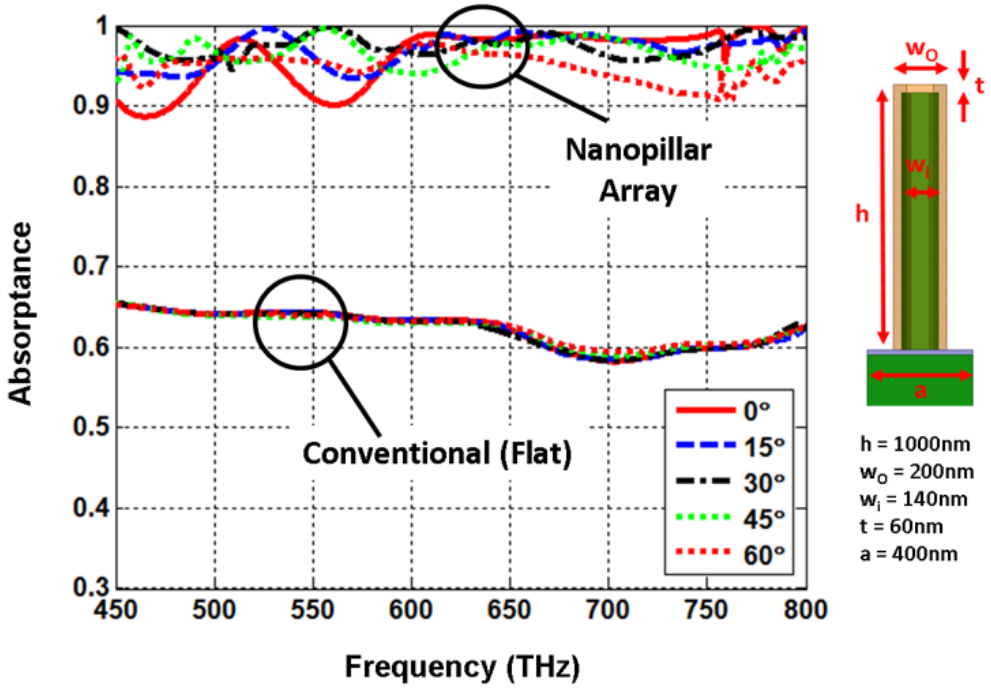

Figure 6.5: Comparison of absorptance of unpolarized light over the visible spectrum between a bulk (flat) GaAs sample with a representative nanopillar for angles of incidence up to 60°. Only a maximum of absorptance of $< 65\%$ is possible with a flat GaAs sample whereas the nanopillar array features $> 90\%$ absorption.

6.1.4 Nanopillar Array Electromagnetic Analysis

6.1.4.1 Parametric Analysis

To understand the optical absorption behavior of nanopillar arrays to different pillar dimensions, array configurations, and the incident angle of light, a number of parametric studies were conducted. In (2), optical absorption is calculated by subtracting both the squared magnitude of the reflection and transmission coefficient from unity. In representative designs of nanopillar arrays, there is a substrate that provides the base for the nanopillars as shown in Fig. 6.1. This substrate is made of semiconductor or dielectric material where light is absorbed or transmitted through. This absorbed energy is considered as loss because the

primary active region (where electrons are extracted) of the solar cell is solely the nanopillar. To account for this lost energy is possible; however, to simplify the analysis, two configurations were used to eliminate the need to calculate the substrate absorption. First was to eliminate the substrate completely and have a nanopillar-only array. The second was to replace the semiconductor/dielectric substrate with a substrate made completely of perfect electric conductor (PEC). In both cases, the nanopillars are made of GaAs material. By examining these two configurations, it is also possible to understand the role the substrate can play in the optical absorption of the arrays. A third configuration is introduced in a later section, where the entire nanopillar and substrate is comprised of PEC material. A diagram of each unit cell of the three configurations is shown in Fig. 6.6.

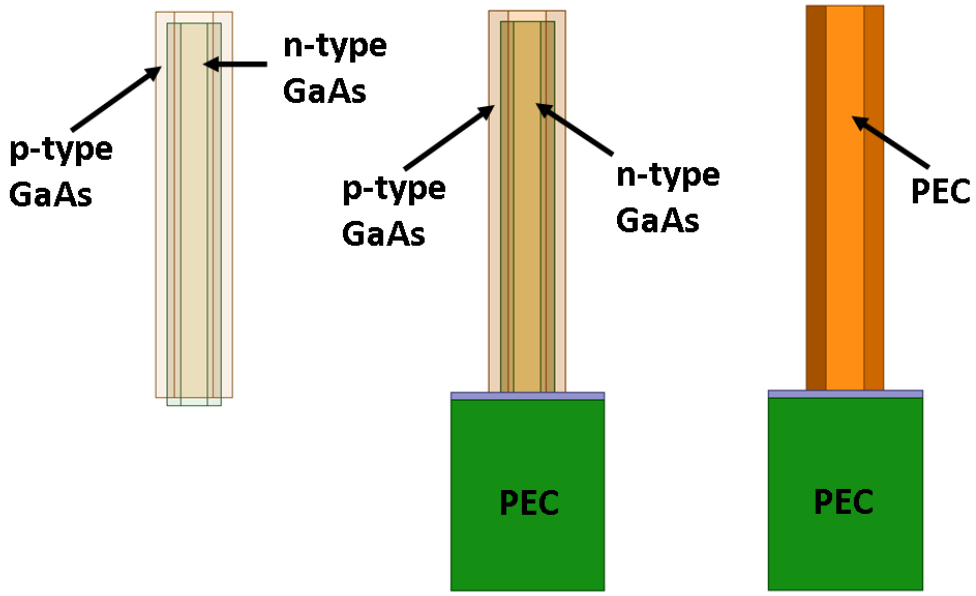

Figure 6.6: Nanopillar array unit cell of the three configurations considered in Section V. (a) Nanopillar-only. (b) Nanopillar-array with PEC substrate. (c) All-PEC nanopillar array.

The following parametric studies were conducted: Nanopillar separation, nanopil-

lar height and diameter, and angle of incidence. In the nanopillar-only configuration, the optical absorption is calculated using (2). For the nanopillar array with PEC substrate, transmission is zero and the absorption is calculated by subtracting the square of the reflection coefficient magnitude from unity. Dimensions and the configuration of each parametric study are labeled in the corresponding figures. The structures were simulated over the frequency range of 450 THz to 800 THz (375 nm667 nm (visible spectrum)).

Nanopillar Separation Parametric Investigation The nanopillar array with PEC substrate and square periodicity was simulated at normal incidence with three different nanopillar center-to-center separation distances (pitch), 400 nm, 500 nm, and 600 nm with nanopillar diameter of 200 nm and height 250 nm. The absorptance of the three separation distances is shown in Fig. 6.7. Clearly, differences appear between the three distances. In particular, a region of highly oscillatory levels of absorptance can be seen. Interestingly, this region of oscillatory reflection magnitude begins exactly at the frequency where the nanopillars are exactly one free-space wavelength. From electromagnetic theory, when elements of a periodic array are at least one wavelength apart, grating lobe phenomena begins to appear and will affect the electromagnetic performance of the array. These grating lobes, defined by undesirable peaks and nulls in the electromagnetic field, can cause oscillatory behavior and higher average reflection over the spectrum. Angle of incidence also affects the formation of this phenomenon: As the angle of incidence increases, the separation distance must decrease to avoid such effects. A similar trend was seen in the nanopillar-only array simulation.id such effects.

An effective way to prevent these grating lobe phenomena is to keep the separation distance less than one wavelength. For normal incidence, a 400nm pitch resulted in stable and lower average reflection over the visible spectrum. This separation was maintained for the rest of the parametric investigations due to

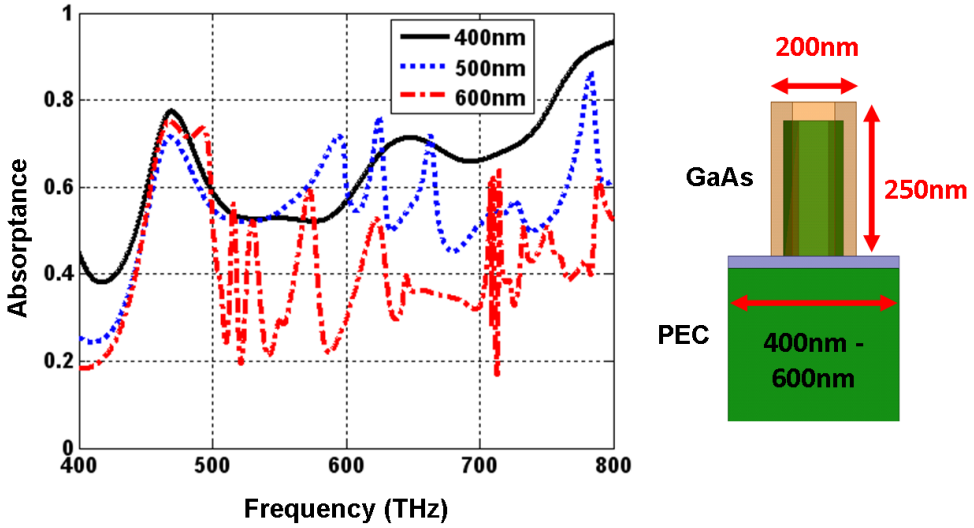

Figure 6.7: Reflection magnitude of varying separation distances. The separation distance has a profound effect on where grating lobe behavior begins.

physical constraints: The nanopillars must maintain a minimum diameter to ensure efficient carrier generation and extraction [34]. At steeper angles of incidence the grating phenomenon will appear at this pitch, however, other techniques such as configuring the array with triangular periodicity rather than square periodicity, may help reduce these effects [6].

Height and Diameter Parametric Investigation Both the nanopillar-only array and the nanopillar array with PEC substrate configurations were simulated with nanopillars of different heights (250 nm2000 nm) and diameters (150 nm350 nm) at frequencies of 400 THz, 600 THz, and 800 THz and with a fixed separation distance of 400 nm. Figs. 6.8 and 6.9 shows the absorptance of the nanopillar diameter versus height at each of the three frequencies.

Plotted in this manner, the absorption behavior is illustrated over the entire parametric space. In general, absorption is larger for longer pillars, whereas the

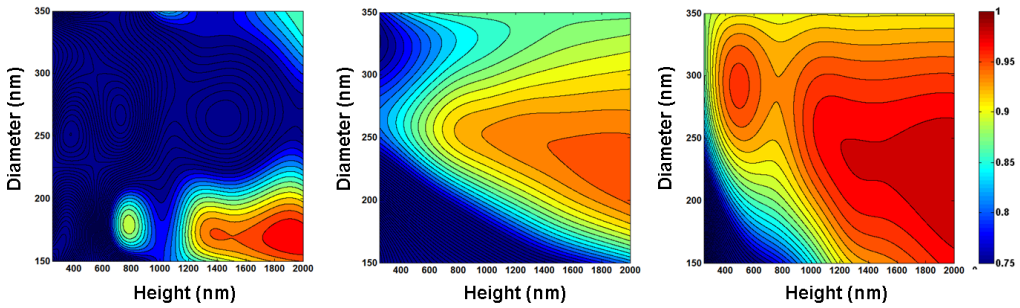

Figure 6.8: Absorptance of a nanopillar-only array with nanopillars of diameters of 150 nm to 350 nm and heights of 250 nm to 2000 nm with a fixed separation distance of 400 nm for normal incidence. Frequency: (a) 400 THz, (b) 600 THz, (c) 800 THz. In general, the optical absorption increases as the pillar gets longer in relation to the incident wave wavelength. The behavior due to the nanopillar diameter is more irregular and suggests a modal response to the incident wave.

diameter of the pillar has irregular behavior suggesting a modal response in absorption coupling of the nanopillar. This is seen in Fig. 6.8, where there is a clear improvement in absorption up to Formula for diameters of 250 nm, and Fig. 6.9 where there is an improvement at 200 nm and 300 nm diameters. The absorption increases essentially monotonically with the length of the nanopillar, with the highest absorption found when the nanopillar is longer. The total length of the pillar is usually limited to about $5\mu m$ long. Beyond this length, the pillars have a tendency to bend and deform to the point of touching adjacent pillars. As the frequency of operation increases, even shorter pillars have increased absorption (600 nm pillar height at 800 THz).

It can be speculated that the behavior of the absorption for pillars of different dimensions is a function of how well incident energy is coupled into the array. The frequency of incident light, the diameter and height of the nanopillar, and the separation distance seem to be all the parameters that can change amount of energy coupled from the air into the nanopillar array. It implies that the

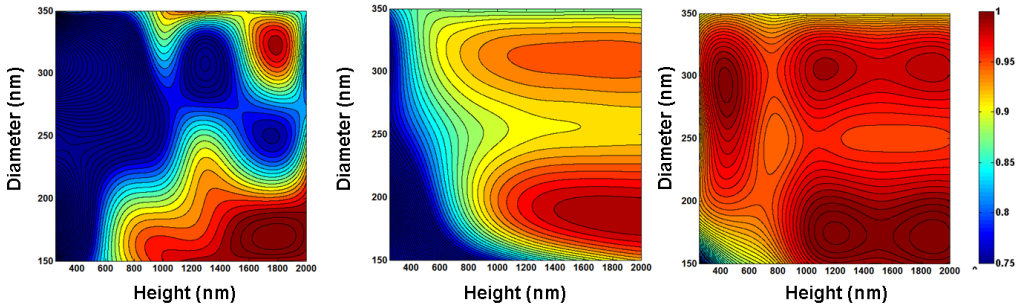

Figure 6.9: Absorptance of a nanopillar array with a PEC substrate with nanopillar diameters of 150 nm to 350 nm and heights of 250 nm to 2000 nm with a fixed separation distance of 400 nm for normal incidence. Frequency: (a) 400 THz, (b) 600 THz, (c) 800 THz. In general, the optical absorption increases as the pillar gets longer. The behavior due to the nanopillar diameter is more irregular and suggests a modal response to the incident wave. The PEC substrate has an advantageous effect on absorption due to the energy being reflected back along the pillar where increased absorption occurs.

nanopillar array acts an electromagnetic interface: Its dimensions determining how well the incident energy is coupled into the array. In addition, the diameter of the nanopillar, with its irregular behavior over different values and its apparent frequency dependence could imply that resonance effects are present.

Another interesting observation that can be made in Fig. 6.9 is that optical absorption is increased for the array that includes the PEC substrate. Not surprisingly, any incident energy not absorbed on the first pass is reflected and can be reabsorbed on the second pass past the nanopillars, effectively doubling the length of the nanopillar. In fact, the reflected energy interferes with the incident field and creates intense pockets of energy in between the pillars (provided the pillars are long enough) where significant absorption occurs. This absorption phenomenon is visualized in Section V-B. A comparison between the optical absorption for the nanopillar array with PEC substrate and the representative nanopillar array in

Fig. 6.5 shows that the absorption into the substrate is only a small fraction of the overall absorption. This supports the supposition that a nanopillar array that features a semiconductor substrate behaves similarly to a nanopillar array with a PEC substrate.

Angle of Incidence Investigation The nanopillar array with the PEC substrate was used to investigate the pillar's dependence on the angle of incidence of the incoming optical field. For improved performance, it is advantageous to have similar performance for all angles of incidence. This would allow the elimination of mechanical tracking that many commercial solar applications require. Fig. 6.10 shows the unpolarized optical absorptance for angles of incidence varying from 15° to 75°, respectively. The dimension of the pillars can be seen in the figure. In both cases, the differences between each angle of incidence were small up to 60°, indicating consistent enhanced optical absorption of Formula over large angles of incidence.

6.1.4.2 Nanopillar Array Fields

The concept of light-trapping has been described as the primary reason for the improved optical absorption for nanopillar structures. Some have described this effect in the ray optics sense, describing the trapping as oblique incident waves reflecting inwards towards the substrate [21]. This description, however, is less accurate for sub-wavelength structures (including nanopillars) and cannot explain the improved optical absorption at normal incidence. Furthermore, the improved performance over conventional cells at large angles of incidence implies that particular mechanisms allow for efficient absorption to occur. To understand these mechanisms, it was determined that an analysis of the field interaction with the nanopillar array could help reveal the electromagnetic operation that drives optical absorption. The full-wave solver has the ability to generate the total electric

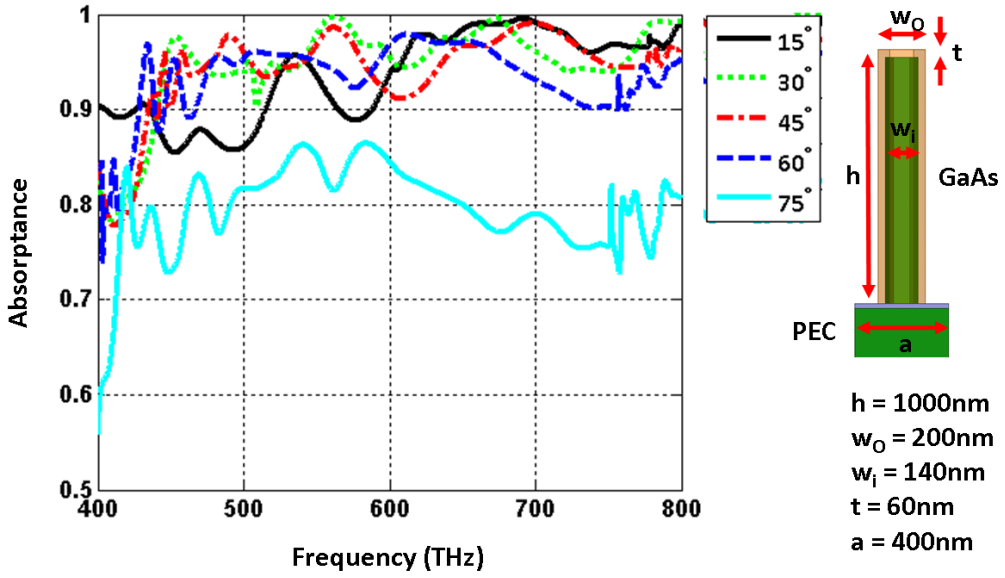

Figure 6.10: Absorptance of a nanopillar array with PEC substrate for unpolarized lights at angles of incidence of 15° to 75°. The absorptance remains > 90% for angles up to 60°.

fields at various incident phases and angles allowing for an animation of the field distribution in the vicinity of the nanopillars. Such visualizations can illustrate the absorption process of the nanostructure PV arrays and potentially reveal the underlying physics behind its inherent improvement of absorption over conventional photovoltaics.

It can be hypothesized that the absorption mechanism of these devices is a function of both the structure (i.e., dimensions) and the complex material properties of the semiconductor. To decouple and understand the role of these two aspects of the nanopillars, simulations of a nanopillar array using completely perfect electric conducting material was included in the analysis along with aforementioned nanopillar-only and nanopillar array with PEC substrate configurations. An analysis of the field distribution allowed for some insight into the electromagnetic operation of these structures.

Fig. 6.11 shows the total electric field magnitude $|E|$ in the vicinity of the nanopillars for the all-PEC, nanopillar array with PEC substrate, and nanopillar-only array for a normal incident plane wave at 600 THz ($\lambda_0 = 500nm$). Five images are shown for each array configuration, each representing a phase step from 0° to 150°. The nanopillar dimensions for all the configurations were: Height 1000 nm, diameter 200 nm, and separation distance of 400 nm.

Over the phase progression, a particular periodic electric field distribution is created in between the nanopillars in the array. For the PEC nanopillar in Fig. 6.11(a), no energy is absorbed and resulting combination of the incident and scattered electric fields creates a stationary standing-wave field distribution that fits two cycles along the length of the nanopillar, corresponding to approximately two full free-space wavelengths at 600 THz. Throughout the phase progression, it is seen that these fields cycle between maximum and minimum levels but do not deviate along the vertical length of the pillar.

Similarly, a periodic field distribution is created in-between the nanopillars for the semiconductor nanopillars with and without the substrate. This distribution, in contrast, is not stationary throughout the progression of the phase as it is with the PEC nanopillars. In fact, the fields move downward from the top of the pillar down along the length of the pillars as the phase progresses. This behavior is expected in the nanopillar-only case, since there is no substrate to reflect energy back, however, in the nanopillar array with PEC substrate case, the fields still move slightly downward, indicating that the reflected field is too weak to create the standing-wave distribution that appears with the all-PEC nanopillar array. This difference can be attributed to the optical absorption of the nanopillar itself: As the incident wave travels downward the fields penetrate the skin of the nanopillar where it is absorbed. The amount of absorption is subject to the material properties and geometric dimensions as seen in the parametric studies. In the two cases, it is clear that fields are primarily coupled in between the nanopillars

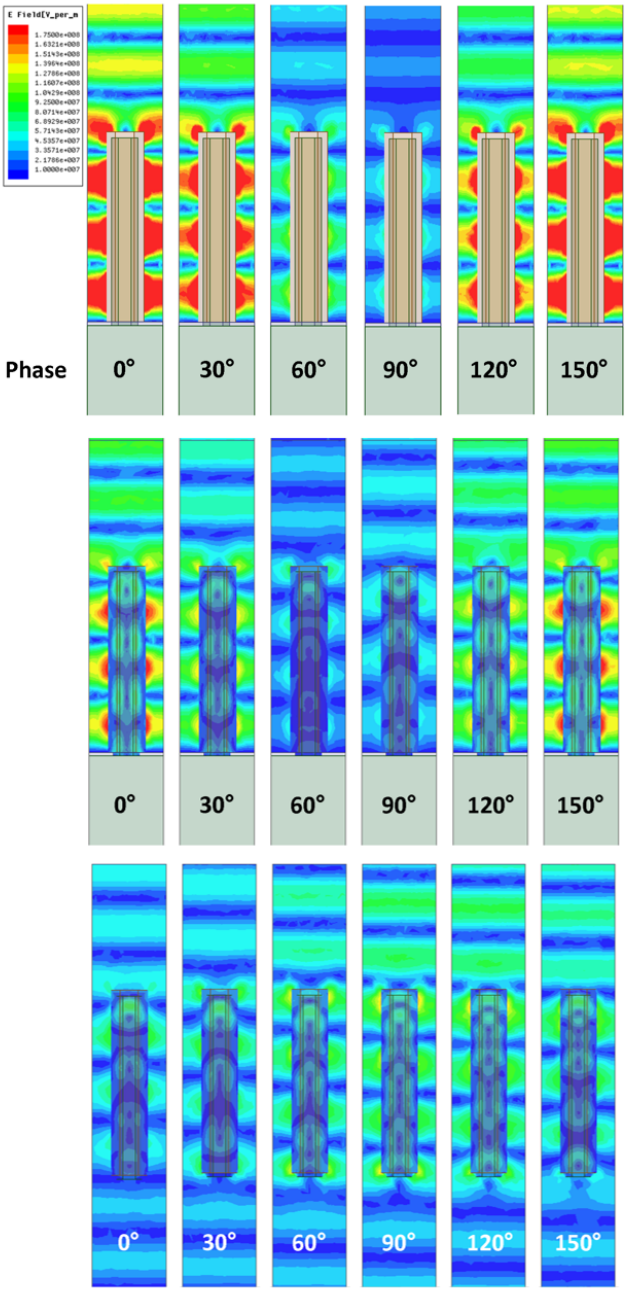

Figure 6.11: Total electric field magnitude Formula for normal incidence in the vicinity of the nanopillar unit cell. (a) All-PEC nanopillar array, (b) Nanopillar array with PEC substrate, and (c) Nanopillar-only array. Each adjacent image shows the phase angle for the incident electric field. Nanopillar dimensions are shown in Fig. 6.10.

and energy is absorbed due to the lossy nature of the semiconductor material when in the vicinity of the fields.

The presence of a reflecting substrate provides an important secondary advantage for improved absorption. The reflective nature of the substrate provides a scattered field that interacts constructively with the incident field that increases the magnitude of the electric fields next to the nanopillar and increases the overall amount of energy absorbed. This is supported by the parametric studies in Figs. 6.8 and 6.9, where higher overall absorption is observed for the PEC-substrate nanopillar array.

A similar absorption mechanism is observed at oblique incidences of light. Fig. 6.12 shows the TE-polarized electric fields for an all-PEC nanopillar array for an incident wave at an oblique angle of 45°. In a similar fashion to the normal incidence case, a standing-wave pattern is created: In this case, only one wavelength cycle is present along the vertical length of the nanopillar. As with the normal incident case, the standing wave is stationary as it was for normal incidence. Likewise for the semiconductor nanopillar array, the standing wave distribution travels downward into the substrate indicating a similar absorption mechanism as for normal incidence (not shown in the figure).

In summary, the nanopillar array structure acts like an electromagnetic absorbing (attenuating) interface subject to classical sub-wavelength electromagnetic properties that traditional ray-optics cannot predict. The array dimensions and configuration is responsible for coupling the energy from the air into the array, and the materials used responsible for the total amount of energy absorbed. Thus, the initial interface between the air and nanopillar array is an important aspect of the nanopillar design and must be optimized. Different shaped nanopillars such as conic, pyramidal, etc. could be possibilities to explore for absorption characteristics (Section VI). It is also plausible that a certain dimensions of nanopillar may be found that will optimize the absorption of optical field inside the nanopillar

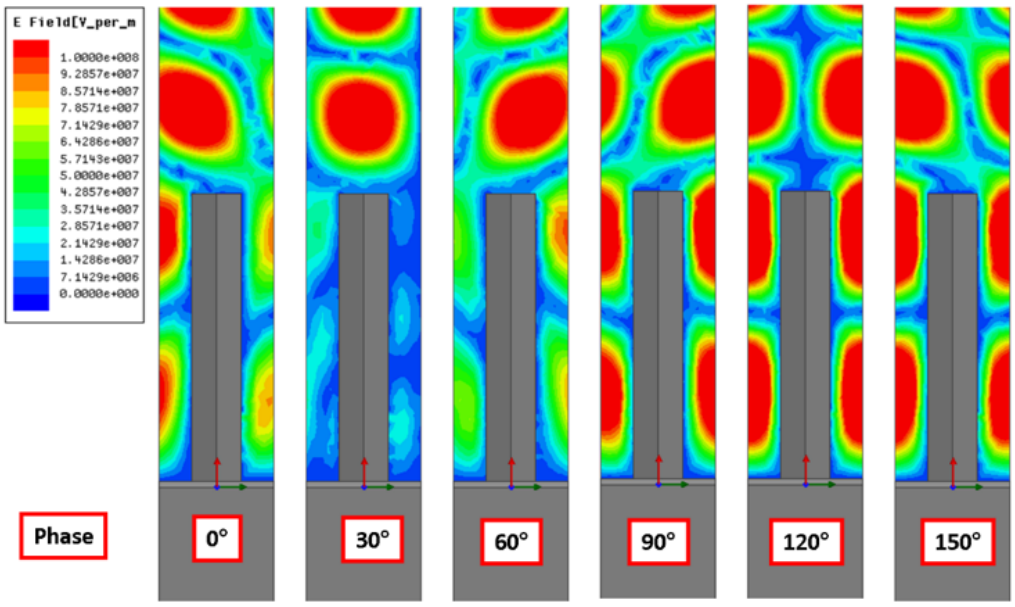

Figure 6.12: PEC nanopillar TE electric field magnitude $|E|$ in the vicinity of the nanopillars for phases 0° to 150° for an oblique incidence of 45°. Incident field frequency 600THz (500 nm).

structure.

6.1.5 Concepts for Next Generation Nanostructure Solar Cells

New concepts for nanostructures are actively being pursued to maximize optical absorption in nanostructure photovoltaics. One initial study involved analyzing the absorption of canonical nanostructure shapes such as a nanocone and nanopyramids [38, 48]. Fig. 6.13 shows a comparison of absorptance for these three nanostructure shapes for a constant separation distance and structure height. This improvement suggests that cones and pyramids provide a better match to the free-space impedance, allowing for better coupling into the region between nanopillars. Intermediate shapes that are in between a conic shape and pillar shape, such as superquadric nanostructures [49], will be considered in the next section.

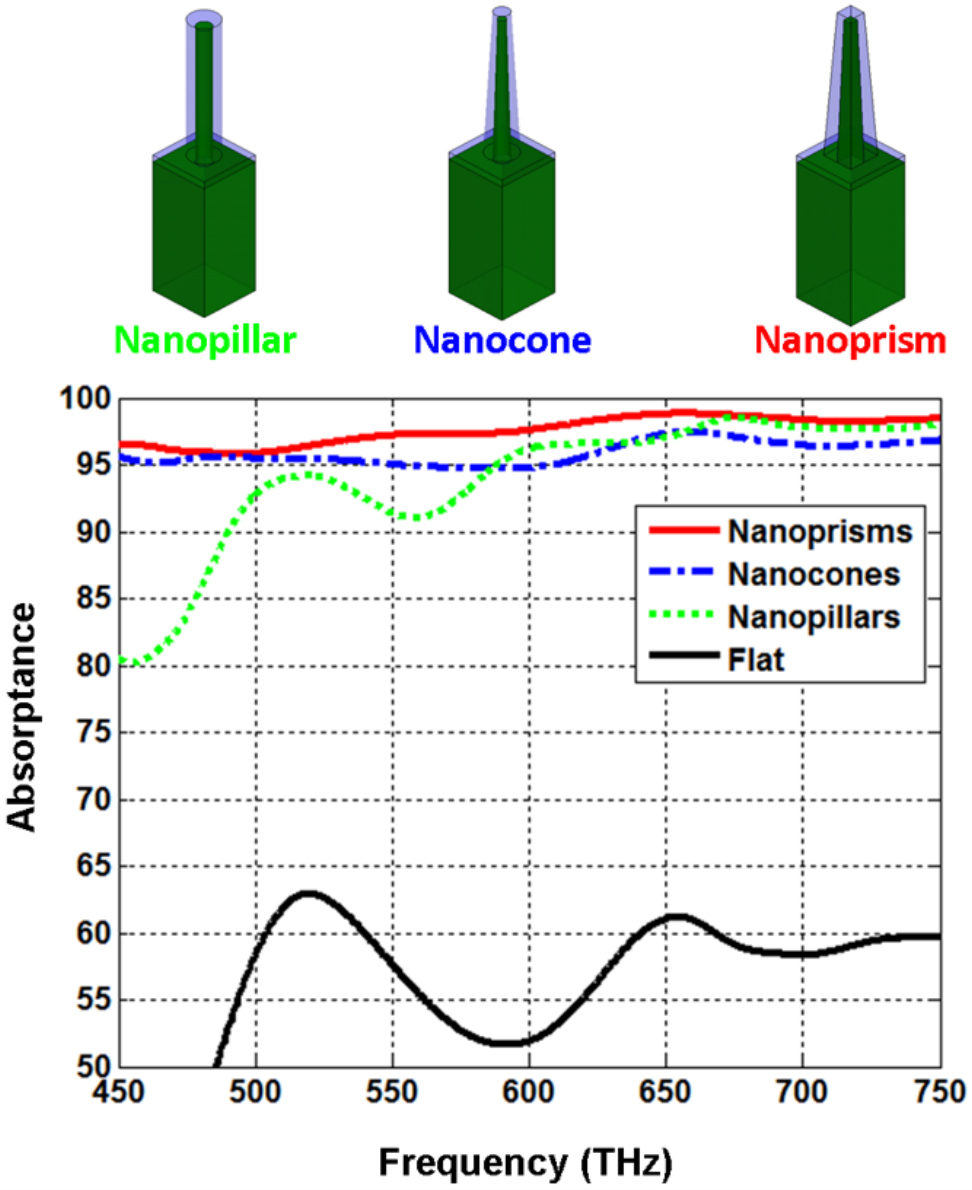

Figure 6.13: Comparison of absorptance between nanocones, nanopillars, nanoprisms arrays, and a flat cell. Improvement in overall reflection is seen for nanocone and nanoprism structures.

6.1.6 Superquadric Nanostructure Solar Cells

Increasing the absorption efficiency is one of the key tasks towards maximizing the overall solar cell efficiency which is a product of absorption efficiency, carrier

generation efficiency, and carrier extraction efficiency. It was shown in [2] that nanoconic and nanopyramid photovoltaic arrays have better broadband properties than nanopillar arrays. This can be potentially attributed to better matching between free-space and the nanostructured arrays. However, due to current fabrication limitations, these canonical structures may not be feasible in their true form. For example, fabrication techniques had to be devised that allowed the use of nanopillars as starting structures with modifications done afterwards to resemble conic or pyramidal shapes [3]. Although these structures are close in form, they are not exactly similar. Most likely, structures fabricated using such techniques will have a shape somewhere between a complete nanopillar and a nanopyramid. To understand the electromagnetic performance for these intermediate structures, it was necessary to identify a series of shapes that could closely represent them utilizing an appropriate function.

It was determined that a superquadric function could serve this purpose. This paper will investigate different superquadric nanostructured PV arrays for their reflection and absorption properties. Different shapes generated using the superquadric function will be evaluated for their optical properties ranging from hexagonal nanopillar to hexagonal nanopyramid. The elliptical superquadric nanostructures will be used for different parametric studies including height variation.

The definition of a superquadric boundary is given by

$$[(\frac{x}{a})^2]^n + [(\frac{y}{b})^2]^n = 1 \tag{6.4}$$

where a and b are the radii along the x and y-axes and n controls the shape of the superquadric curve. The parameterization of the superquadric curve is given by [5]

$$x(t,\Psi) = at\cos(\Psi)\frac{1}{[(\cos(\Psi)^2)^n + (\sin(\Psi)^2)^n]^{\frac{1}{2n}}} \tag{6.5}$$

$$y(t,\Psi) = bt\sin(\Psi)\frac{1}{[(\cos(\Psi)^2)^n + (\sin(\Psi)^2)^n]^{\frac{1}{2n}}} \tag{6.6}$$

Examples of parametric superquadric shapes are plotted for different n in Fig. 1 where t = 1, $\Psi = 0 : , a = 2000nm$, $b = 170nm$. Only half of the major axis is plotted. It can be seen that the curve is triangular for $n = 0.5$, ellipse when $n = 1$ and becomes rectangular as n increases ($n = 100$). We form a 3-D nanostructure surface using this curve, where the 3-D structure has 6 faces.

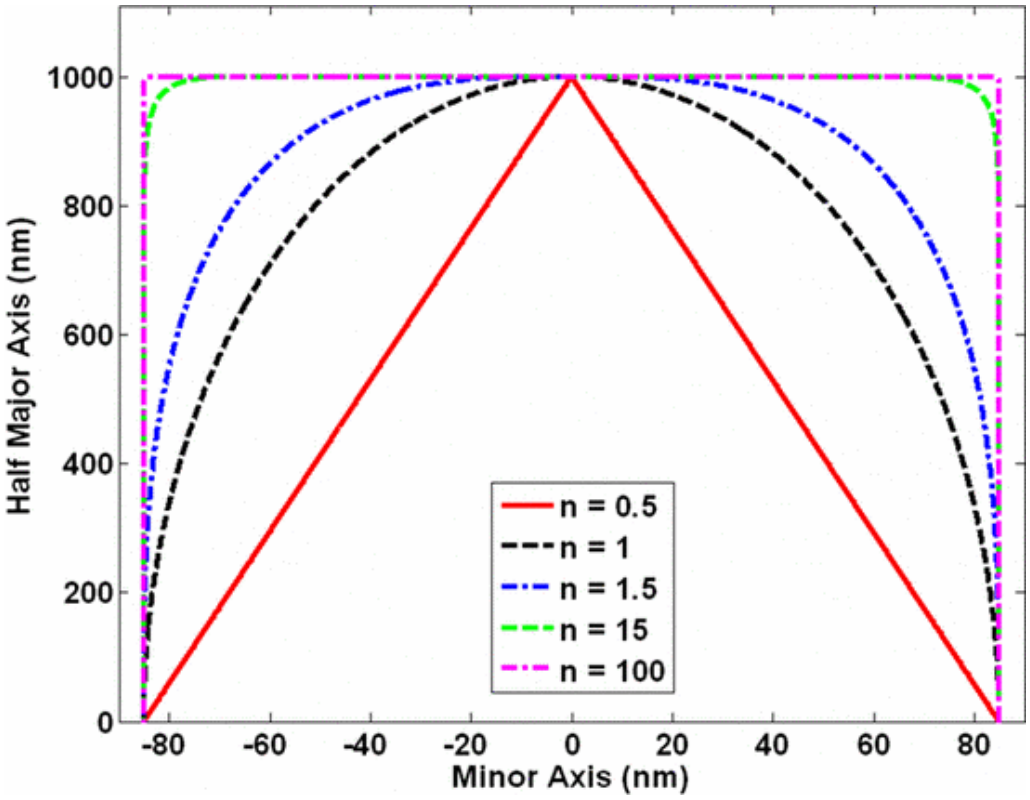

Figure 6.14: 2-D superquadric shapes for different values of n.

6.1.6.1 Superquadric Nanopillar Design and Analysis

To apply the superquadric function to the overall design of the nanopillar required a fourth parameter, ζ, which was used to describe the fraction of the nanopillar's total height that was in the shape of a superquadric function versus a straight nanopillar. Fig. 6.15 shows three nanopillar designs with $\zeta = 0.1$, $\zeta = 0.5$, and $\zeta = 0.95$. Coupled with the parameter n, the overall performance of the nanopillar can be evaluated using the same techniques as the straight pillars. In these investigations, we use a PEC substrate to eliminate the need to evaluate the transmission. Absorptance in the following figures is define as: $Absorptance = 1 - |\Gamma|^2$.

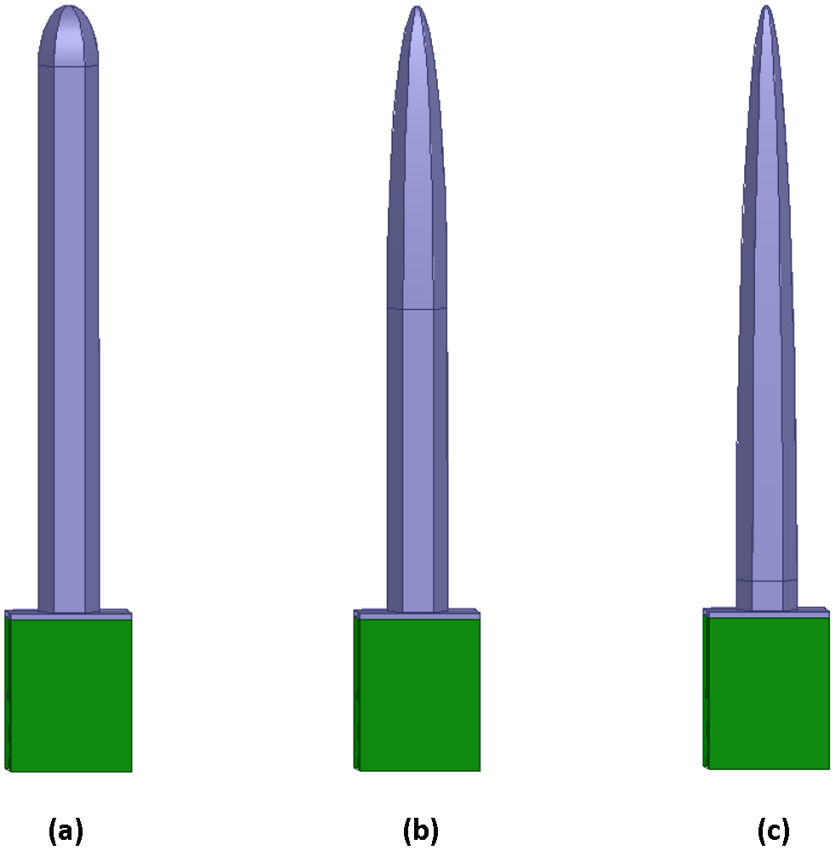

Figure 6.15: Representation of the nanopillar for different values of ζ.

The first evaluation that was conduced was to vary ζ and n and understand their effect on absorptance. In HFSS, three values $\zeta = 0.1, 0.5, 0.95$ were evaluated for $n = 0.5$ (conic), $n = 1, 4, 7, 10$. The pillar height and diameter was fixed at 2000nm and 200nm, respectively. The separation between adjacent nanopillars was 400nm. The nanopillar array was simulated over the frequency band of 400THz - 800THz at normal incidence. The resultant absorptance is shown in Fig. 6.16. From the results, it can be concluded that the shape of the nanopillar is more favorable for absorption if the superquadric shape is used over the majority of the nanopillar ($\zeta = 1$). In addition, the value of n shows that a conic shape ($n = 0.5$) is not necessarily the best. In fact, an n of about 1 seems to provide the best absorption over the visible band, avoiding the large oscillations in reflection magnitude seen with higher values of n.

The optimum value of n was clearly close to 1, however, to verify this a parametric investigation of n was conducted for a nanopillar with dimensions: Height = 2000nm, Diameter = 200nm, Pillar Separation = 400nm, $\zeta = 0.95$. The nanopillar was simulated over the visible band of 400THz - 800THz at normal incidence. The results are shown in Fig. 6.17(a). For this class of structure, $n = 1$ seemed to provide the best performance over the visible band. Furthermore, the performance of the structure over different angles of incidence was investigated and its results shown in Fig. 6.17(b). With this structure, it is possible for absorption rates of $> 97\%$ up to incident angles up to 60° and $> 90\%$ up to incident angles up to 75°.

In the preceding investigations, the diameter and height of the nanopillar was fixed to 200nm and 2000nm, respectively. To understand the effect of the diameter and height of the pillars, two parametric investigations were conducted using the best performing parameters of ζ and n. The first investigation was on different diameters of the nanopillar. The results are shown in Fig. 6.18(a). It clearly shows that a larger diameter is favorable. Using the largest diameter, 350nm, the height

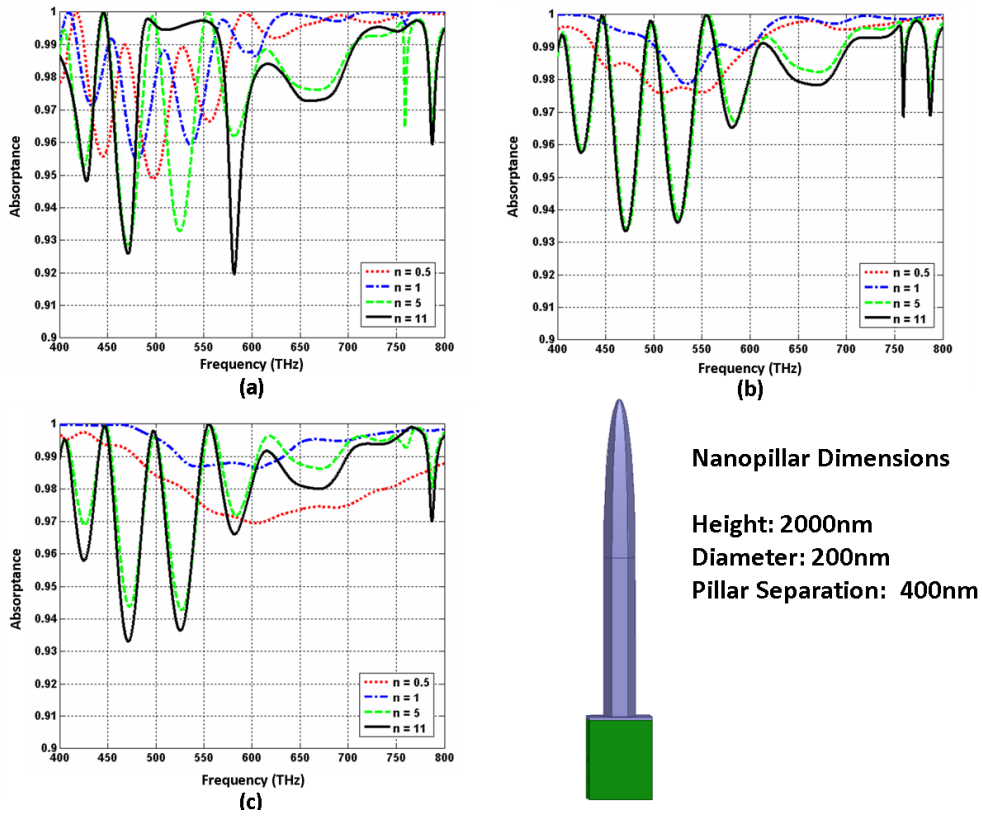

Figure 6.16: Absorptance of various superquadric nanopillars for different values of n. (a) $\zeta = 0.1$ (b) $\zeta = 0.5$ (c) $\zeta = 0.95$

was varied from 500nm to 3000nm. These results are shown in Fig. 6.18(b). As we saw with the straight pillars, the longer the pillar, the better the absorptance. In fact, once the pillar is longer than 2000nm, the overall absorptance reaches 100%!

In conclusion, the superquadric shape is theoretically a very favorable shape for improving the overall absorptance of the nanopillar array. Although such shapes may be very difficult to fabricate, the analysis show here shows that the elliptical curve provides an excellent interface for incoming electromagnetic waves. With proper dimensions, almost all the incident energy can be absorbed potentially improving solar energy harvesting efficiency. Future research can be conducted to

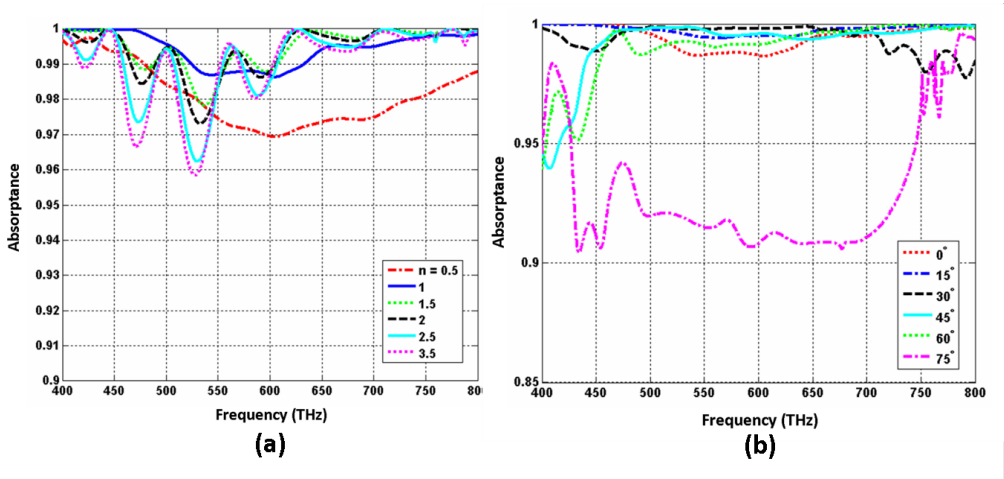

Figure 6.17: (a) Absorptance of a superquadric nanopillar with $\zeta = 0.95$ and values of n close to 1. For this class of nanopillar, $n = 1$ shows the best performance over the visible band. (b) Absorptance of a superquadric nanopillar with $\zeta = 0.95$ and $n = 1$ for different angles of incidence. Excellent absorptance is seen for angles up to 75°.

determine if such superquadric shapes will be possible to fabricate.

6.1.7 Superquadric Shapes for Absorbing Interfaces

The analysis of the superquadric nanopillar array was conducted using well-established numerical techniques that were developed in the microwave regime. A close corollary that acts very similar to solar cell arrays is microwave absorber used in anechoic chambers. These structures are also periodic structures primarily used for absorption and can be modeled similarly to nanopillar arrays.

The most common microwave absorber structure is pyramidial shaped cones. They come in all heights and widths, however, the majority use similar carbon-loaded polyethylene material. To model the absorber in the analysis here, we chose to use the dimensions of the absorber used in UCLA's spherical near-field chamber. A photograph of the absorber and its dimensions are shown in Fig.

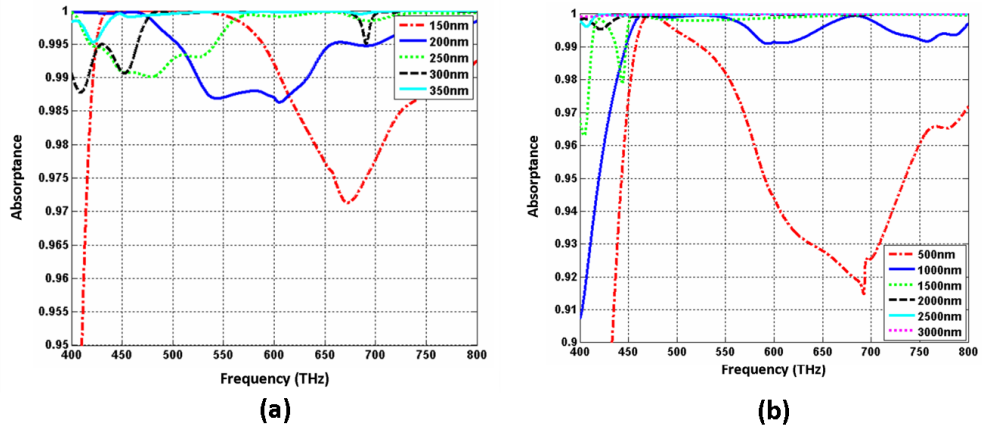

Figure 6.18: (a) Absorptance of a superquadric nanopillar with $\zeta = 0.95$, $n = 1$, height = 2000nm, pillar separation = 400nm for different nanopillar diameters. Larger diameters show better overall absorptance. (b) Absorptance of a superquadric nanopillar with $\zeta = 0.95$, $n = 1$, diameter = 350nm, pillar separation = 400nm, for different nanopillar heights.

6.19. As with the nanopillar arrays, the analysis will involve using a single unit cell with periodic boundaries.

To compare the performance between the conic and superquadric shape it was important to keep the height and width of the absorber constant. As shown in the previous section, the longer the pillar, the more absorption occurs. However, for microwave absorber, it is preferred to have the absorber as short as possible, so that it takes up less space and is less expensive to produce and purchase. With that in mind, we compared a conic pyramidal shape to a number of superquadric designs with different n's. In this case, we set $\zeta = 1$, since it was shown that applying the superquadric shape over the entire length of the pillar was more favorable for absorption. The comparison was conducted over the band of 1GHz to 10GHz at normal incidence. In addition, we compared the reflection magnitude instead of absorptance as it is the convention for microwave absorber.

Fig. 6.20 shows the comparison of the reflection magnitude of the microwave

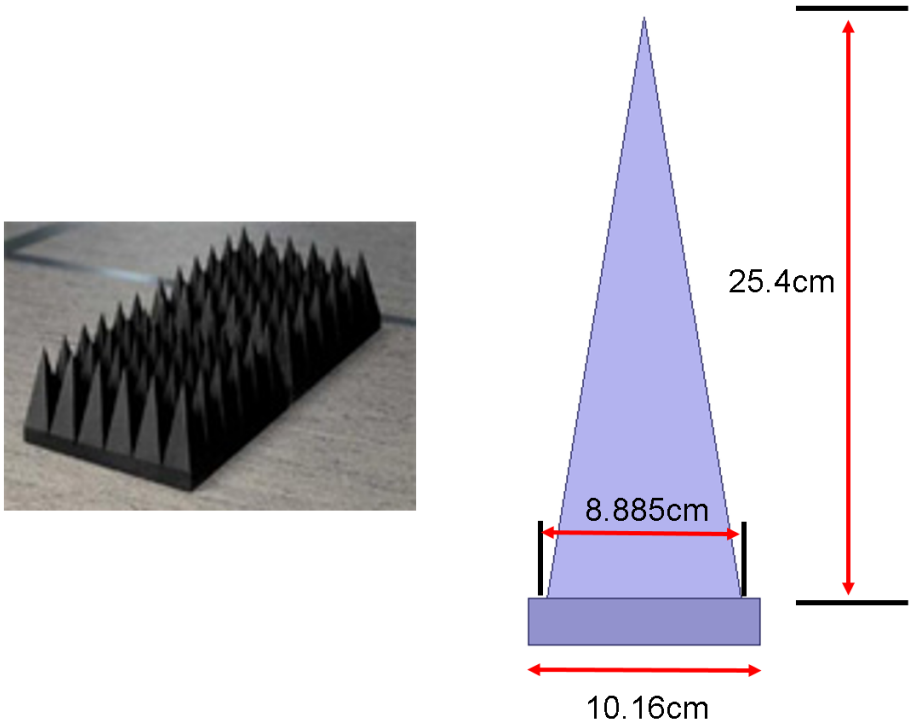

Figure 6.19: Photograph of the TDK microwave absorber that was modeled for the analysis. The dimensions of the single pillar is shown as well.

absorber analysis. It shows that the superquadric shape does indeed improve the reflection magnitude over the conic shape, especially at lower frequencies. Again, this is due to the improved interface at the tip of the pillar. In addition, the extra lossy material that is present with the superquadric shape than with the conic shape allows for increased overall field absorption. These results give credence to the concept of applying these shapes for many applications require excellent electromagnetic absorption. Future research can be done to fabricate, measure, and verify the improved absorption performance of these superquadric microwave absorber.

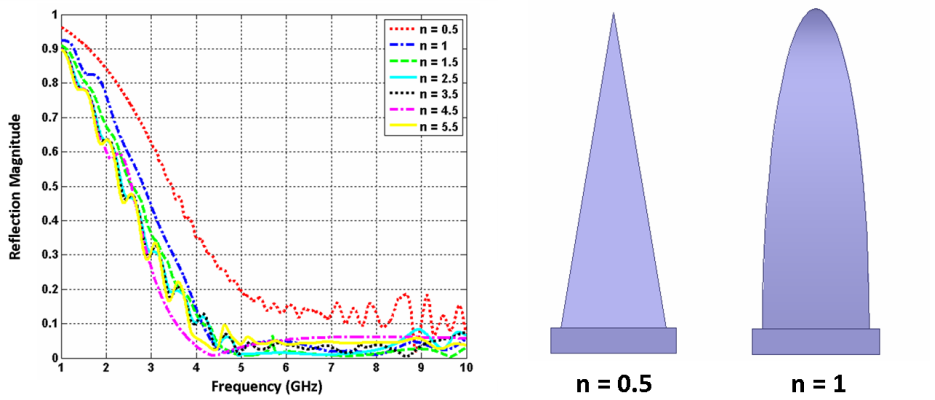

Figure 6.20: Reflection magnitude of the microwave absorber for fixed height of 25.4cm, width of 8.885cm, and cell size of 10.16cm for various values of n. As with the semiconductor nanopillars, improved absorption is seen with the superquadric shape.

6.1.8 Nanostructure Optimization: Analytical Models

Full-wave analysis is the most accurate technique to characterize the electromagnetic operation of the nanostructure arrays. Each simulation run, however, can take a few hours to complete. For optimization techniques that require hundreds of iterations to converge to a solution, such long simulation times make optimization undesirable. Analytical models, based on electromagnetic theory can be developed, to accelerate design and optimization.

6.1.8.1 Effective Dielectric Model

Fig. 6.21 shows a diagram of an effective dielectric model that could be used to calculate absorption of the nanostructure PV arrays as a first order investigation. The model will consist of two layers. The bottom layer will be the bulk substrate subject to the material properties as described in section C.1c. The top layer will represent the nanostructure PV array thorough an effective dielectric

medium. The nanostructure material properties, dimensions, and array configurations will weigh heavily in the calculation of this effective dielectric medium. If a proper dielectric model can be found, then a simple calculation of using basic electrodynamics can be used to compute the levels of optical absorption.

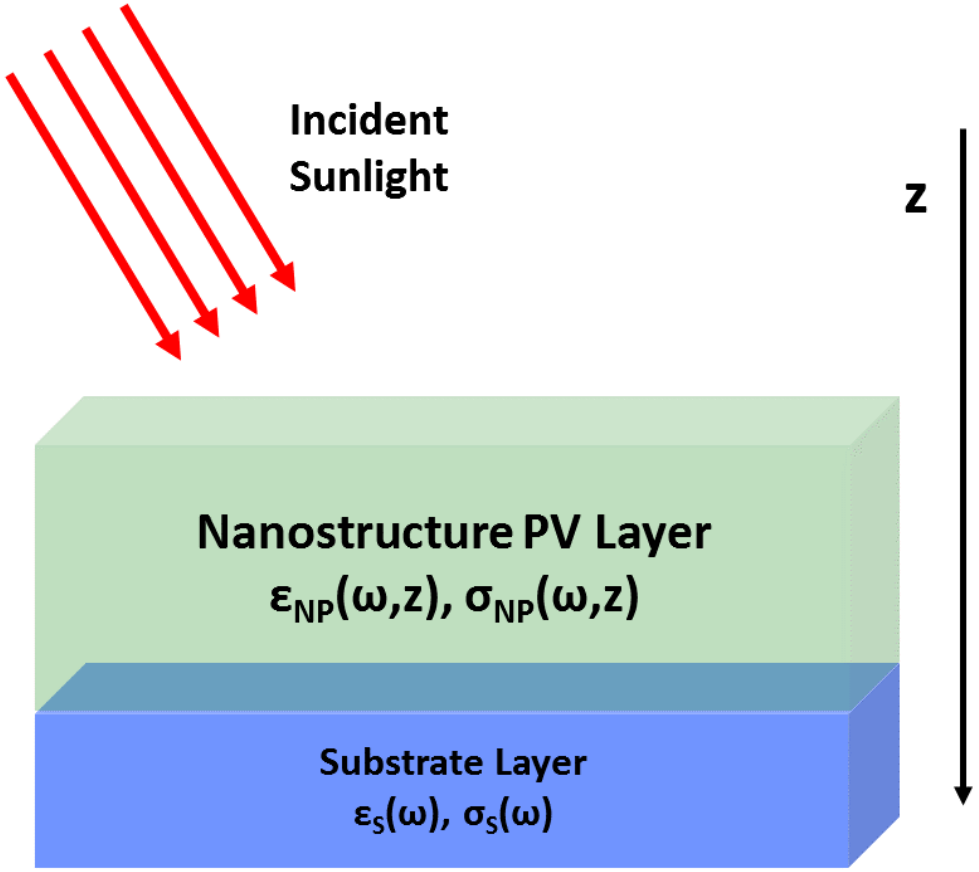

Figure 6.21: Development of an effective dielectric model for the nanostructure arrays. Using this model it may be able to reduce the computation requirements for calculating absorption characteristics.

To obtain a proper model, dielectric homogenization was explored. In [50], it is seen that a periodic array can use homogenization to obtain an effective dielectric within 5%. In particular, the use of the Hashin-Shtrikman formulas provide an reasonably accurate value for the dielectric constant:

$$\epsilon_{eff} = \epsilon_0[1 + g\frac{2(\epsilon_{mat} - \epsilon_0}{(1+g)\epsilon_0 + (1-g)epsilon_{mat}}] \tag{6.7}$$

where g represents the volume fraction of space occupied by the pillar in the unit cell.

6.1.8.2 Shaped Nanopillar Effective Dielectric Model

The two layer model is valid for pillars that do not vary along its length. For shaped nanopillars that do vary along its length, it is possible to break up the pillar into equal thickness slabs, each with its own effective dielectric. Using basic electrodynamics, it is then possible to determine the overall reflection coefficient. This concept is illustrated in Fig. 6.22.

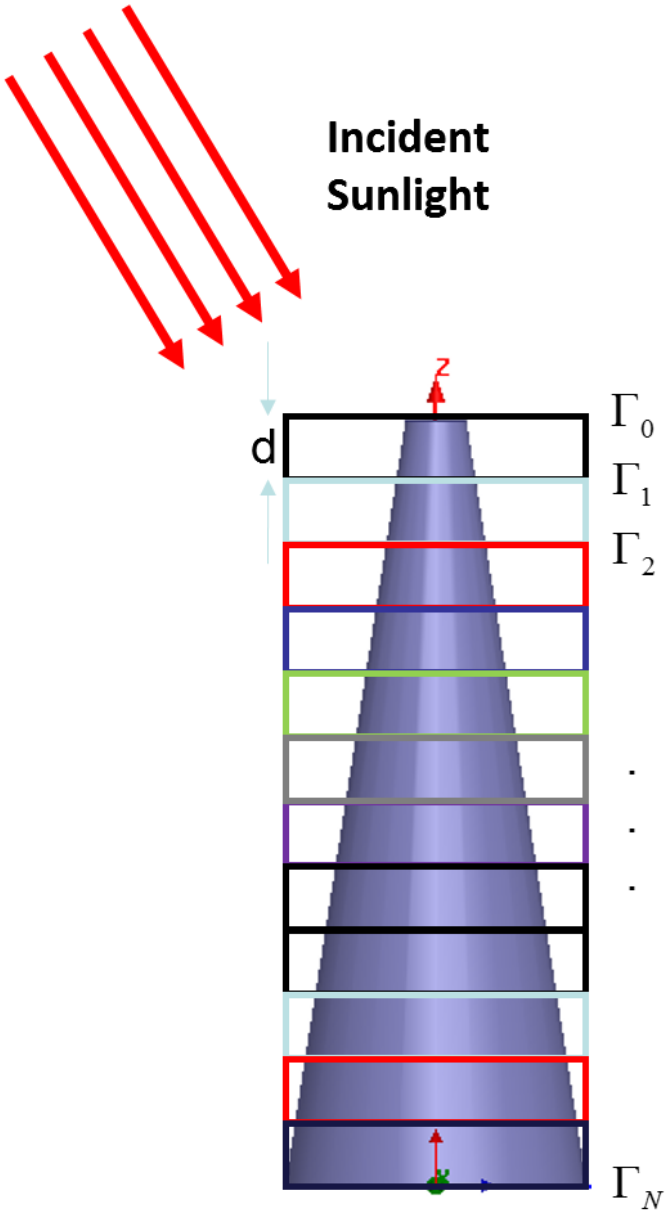

Figure 6.22: Multi-slab model for pillars that vary along its length. Each slab will have its own effective dielectric and basic electrodynamics can calculate the overall reflection coefficient.

CHAPTER 7

Conclusion

Periodic structures for electromagnetic applications have many avenues of research and development. This dissertation introduced novel approaches to antenna array diagnostics, bipolar planar antenna measurement, and solar harvesting technology. In antenna arrays, the subarray design diagnostic technique was introduced as a way to design large antenna arrays using subarrays. Understanding the possible distortions in the subarray radiation pattern is essential in ensuring a proper design. Here these distortions were categorized by the type of excitation configuration and component (amplitude or phase). The concepts of 'null walk-off' and 'null fill-in' were introduced as the two dominant distortions that could cause degradation in the final array radiation pattern. An example of design diagnostics was presented through the design and measurement an 8x8 microstrip patch array that used sixteen 1x4 series excited subarrays.

During the process of measuring the 8x8 array, it was necessary to develop new scanning techniques for the bipolar planer near-field measurement system. New scanning modes, in particular continuous linear and bipolar spiral measurements, were essential to improving measurement times and simplify measurement implementation. Phaseless measurements were attempted with this array, however, the results were not completely satisfactory and future work will aim to improve the overall performance of the phase retrieval algorithm at millimeter-wave frequencies.

Finally, periodic structure electromagnetic analysis was conducted on recently

developed nanostructure arrays. Parametric studies, electric field analysis, and investigation into nanostructure shapes have shown significant inherent improvement of solar energy absorption in nanostructure arrays over conventional flat solar cells. Further investigations into nanostructures can and will be conducted for improvements in solar energy absorption, concentration, and ultimately electricity extraction.

References

[1] R. Haupt, *Antenna Arrays: A Computational Approach*. Englewood Cliffs, New Jersey: Wiley, 2010.

[2] F. Yang and Y. Rahmat-Samii, *Electromagnetic Band Gap Structures in Antenna Engineering*. Cambridge, UK: Cambridge University Press, 2008.

[3] H. Rajagopalan, Y. Rahmat-Samii, and W. A. Imbriale, "Rf mems actuated reconfigurable reflectarray patch-slot element," *IEEE Transactions on Antennas and Propagation*, vol. 56, pp. 3689–3699, December 2008.

[4] L. Hu and G. Chen, "Analysis of optical absorption in silicon nanowire arrays for photovoltaic applications," *Nano Letters*, vol. 7, p. 3249, 2007.

[5] C. Balanis, *Antenna Theory: Analysis and Design*. New York, New York: Wiley-Interscience, 3rd ed., 2008.

[6] R. Mailloux, *Electronically Scanned Arrays*. Amherst, MA: Morgan & Claypool, 2007.

[7] R. Haupt, "Reducing grating lobes due to subarray amplitude tapering," *IEEE Transactions on Antennas and Propagation*, vol. 33, August 1985.

[8] R. Haupt, "Optimization of subarray amplitude tapers," *Proc. Antennas and Propagation Society Int. Symp. Digest*, vol. 4, pp. 1830–1833, June 1995.

[9] R. Mailloux, "Array grating lobes due to periodic phase, amplitude, and time delay quantization," *IEEE Transactions on Antennas and Propagation*, vol. 32, pp. 1364–1368, December 1984.

[10] R. Mailloux, "Grating lobe characteristics of arrays with uniformly illuminated contiguous subarrays," *Proc. IEEE Antennas and Propagation Society Int. Symp.*, pp. 511–514, 1984.

[11] R. Mailloux, L. Zahn, A. M. III, and G. Forbes, "Gating lobe control in limited scan arrays," *IEEE Transactions on Antennas and Propagation*, vol. 27, pp. 79–84, January 1979.

[12] T. Brockett and Y. Rahmat-Samii, "Subarray design diagnostics for the suppression of undesirable grating lobes," *IEEE Transactions on Antennas and Propagation*, vol. 60, pp. 1373–1380, March 2012.

[13] Y. Rahmat-Samii, V. Galinda-Israel, and R. Mittra, "A plane-polar approach for far-field construction from near-field measurement," *IEEE Transactions on Antennas and Propagation*, vol. 28, pp. 216–230, March 1980.

[14] L. Williams, Y. Rahmat-Samii, and R. Yaccarino, "The bi-polar planar near-field measurement technique, Part I: Implementation and measurement comparisons," *IEEE Trans. on Antennas and Propagation*, vol. 42, pp. 184–195, February 1994.

[15] Y. Rahmat-Samii, L. Williams, and R. Yaccarino, "The UCLA bi-polar planar-near-field antenna-measurement and diagnostics range," *IEEE Antennas and Propagation Magazine*, vol. 37, pp. 16–35, December 1995.

[16] O. Bucci, C. Gennarelli, and C. Savarese, "Fast and accurate near-field-far-field transformation by sampling interpolation of plane-polar measurements," *IEEE Trans. on Antennas and Propagation*, vol. 39, pp. 48–55, January 1991.

[17] H. Booker and P. Clemmow, "The concept of an angular spectrum of plane waves, and its relations to thata of polar diagram and aperture distribution," *Proc. Inst. Elec. Eng.*, vol. 97, pp. 11–17, January 1950.

[18] A. Yaghjian, "Approximate formulas for the far field and gain of open-ended rectangular waveguide," *IEEE Trans. on Antennas and Propagation*, vol. 32, pp. 378–384, April 1984.

[19] R. Yaccarino and Y. Rahmat-Samii, "Phaseless bi-polar planar near-field measurements and diagnostics of array antennas," *IEEE Trans. on Antennas and Propagation*, vol. 47, pp. 574–583, March 1999.

[20] S. Razavi and Y. Rahmat-Samii, "A new look at phaseless planar near-field measurements: Limitations, simulations, measurements, and a hybrid solution," *IEEE Antennas and Propagation Magazine*, vol. 49, pp. 574–583, April 2007.

[21] S. Gedney, "Periodic structures and Floquet's theorem." Online Class Notes EE625: http://www.engr.uky.edu/ gedney/courses/ee625/Notes/PeriodicStructures.pdf, 2012. University of Kentucky, Lexington, KY.

[22] Y. Rahmat-Samii, J. Huang, B. Lopez, M. Lou, E. Im, S. L. Durden, and K. Bahadori, "Advanced precipitation radar antenna: Array-fed offset membrane cylindrical reflector antenna," *IEEE Trans. on Antennas and Propagation*, vol. 53, pp. 2503–2515, August 2005.

[23] N. Jin and Y. Rahmat-Samii, "A dual-polarized ku-band microstrip antenna array: A compact feeding network and a refinement strategy using microwave holographic imaging," in *Proc. IEEE Antennas and Propagation Society Int. Symp.*, pp. 2120–2123, June 2007.

[24] R. C. Hansen and G. Charlton, "Subarray quantization lobe decollimation," *IEEE Trans. on Antennas and Propagation*, vol. 47, pp. 1237–1239, August 1999.

[25] T. Brockett and Y. Rahmat-Samii, "Sub-array design diagnostics for the development of large uniform arrays," in *2011 IEEE International Symposium on Antennas and Propagation (APSURSI)*, pp. 938–941, July 2011.

[26] T. Brockett and Y. Rahmat-Samii, "Millimeter-wave bi-polar planar phaseless measurements and diagnostics: Characterization of a ka-band patch array," in *2009 IEEE International Symposium on Antennas and Propagation (APSURSI)*, pp. 1–4, June 2009.

[27] T. Brockett and Y. Rahmat-Samii, "A novel portable bipolar near-field measurement system for millimeter-wave antennas: construction, development, and verification," *IEEE Antennas and Propagation Magazine*, vol. 50, pp. 121–130, October 2008.

[28] T. Brockett and Y. Rahmat-Samii, "Rapid continuous linear spiral measurements for millimeter-waves," in *Antenna Measurements & Techniques Association Conference*, October 2009.

[29] S. F. Razavi and Y. Rahmat-Samii, "Resilience to probe-positioning errors in planar phaseless near-field measurements," *IEEE Trans. on Antennas and Propagation*, vol. 58, pp. 2632–2640, August 2010.

[30] Z. Fan and et. al., "Three-dimensional nanopillar-array photovoltaics on low-cost and flexible substrates," *Nature Materials*, vol. 8, pp. 648–653, 2009.

[31] Z. Chen and et. al., "Aligned amorphous and microcrystalline Si nanorods by glancing angle deposition at low temperature," *Nanotechnology*, vol. 20, 2009.

[32] Z. Chen and et. al., "Optical and electrical properties of single catalyst-free GaAs nanowires," in *UCLA Annual Research Review*, April 2009.

[33] Y. Lu and A. Lal, "High-efficiency ordered silicon nano-conical-frustum array solar cells by self-powered parallel electron lithography," *Nano Letters*, vol. 10, no. 11, pp. 4651–4656, 2010.

[34] G. Mariani, P. Wong, A. Katzenmeyer, F. Lonard, J. Shapir, and D. Huffaker, "Patterned radial GaAs nanopillar solar cells," *Nano Letters*, vol. 11, no. 6, pp. 2490–2494, 2011.

[35] C. H. Peters, A. R. Guichard, A. C. Hryciw, M. L. Brongersma, and M. D. McGehee, "Energy transfer in nanowire solar cells with photonharvesting shells," *J. Appl. Phys.*, vol. 105, p. 124509124509, 2009.

[36] G. Mariani and et. al., "Hybrid conjugated polymer solar cells using patterned GaAs nanopillars," *Appl. Phys. Lett.*, vol. 97, no. 013107, 2010.

[37] T. Brockett, H. Rajagopalan, and Y. Rahmat-Samii, "Gaas nanopillars for solar power absorption: Electromagnetic characterization," in *Antennas and Propagation Society International Symposium (APSURSI)*, July 2010.

[38] H. Rajagopalan, T. Brockett, and Y. Rahmat-Samii, "Investigation of semiconductor nanostructures photovoltaic for next generation solar cells," in *2011 IEEE International Symposium on Antennas and Propagation (APSURSI)*, pp. 1089–1091, July 2011.

[39] G. Conibeer, "Third-generation photovoltaics," *Materials Today*, vol. 10, pp. 42–50, November 2007.

[40] C. Lin and M. Povinelli, "Optimal design of aperiodic, vertical silicon nanowire structures for photovoltaics," *Opt. Express*, vol. 19, pp. A1148–A1154, 2011.

[41] I. M. Pryce, K. Aydin, Y. A. Kelaita, R. M. Briggs, and H. A. Atwater, "Highly strained compliant optical metamaterials with large frequency tenability," *Nano Lett.*, vol. 10, p. 42224222, 2010.

[42] K. Aydin, A. O. Cakmak, L. Sahin, Z. Li, F. Bilotti, L. Vegni, and E. Ozbay, "Split-ring-resonator-coupled enhanced transmission through a subwavelength aperture," *Phys. Rev. Lett.*, vol. 102, p. 1833018330, 2009.

[43] Z. Sheng, D. Da, and S. He, "Comparative study of losses in ultrasharp silicon-on-insulator nanowire bends," *IEEE J. Sel. Topics Quant. Elect.*, vol. 15, p. 14061412, October 2009.

[44] V. Kilmov and M. Dekker, *Semiconductor and metal nanocrystals: Synthesis and electronic and optical properties*. Florida: CRC press, 2003.

[45] D. Aspnes and A. Studna, "Dielectric functions and optical parameters of Si, Ge, GaP, GaAs, GaSb, InP, and InSb from 1.5 to 6.0eV," *Physical Review B*, vol. 27, pp. 985–1009, February 1983.

[46] E. Virgil and J. Rodriguez, "Optical constants of n- and p-type GaAs between 2.5 and 3.5 ev," *Phys. Stat. Sol.*, vol. 90, pp. 409–414, 1979.

[47] E. Palik, *Handbook of optical constants of solids*, vol. I. New York, New York: Elsevier Books, 1st ed.

[48] J. Zhu and et. al., "Optical absorption enhancement in amorphous silicon nanowire and nanocone arrays," *Nanoletters*, vol. 9, pp. 279–282, January 2009.

[49] H. Rajagopalan, T. Brockett, and Y. Rahmat-Samii, "Superquadric nanostructures for enhanced absorption in solar cells," in *2012 IEEE International Symposium on Antennas and Propagation (APSURSI)*, July 2012.

[50] E. Kuester and C. Holloway, "A low-frequency model for wedge or pyramid absorber arrays - i: Theory," *IEEE Trans. on Electromagnetic Comp.*, vol. 36, pp. 300–306, November 1994.